

Kinematic Inversion of Large Relative Motion Datasets Derived from Combined Geodetic Velocity Fields: an Application to the Mediterranean Region

MSc Thesis

Boris Gesbert

January 20, 2022

Abstract

Previous applications of the Spakman-Nyst method to inverse problems of slow regional crustal deformation have been technically restricted to tens or hundreds of geodetic velocities within a single observation network. Here, we test the relative motion inversion technique on thousands of GPS observations compiled from tens of different studies. Our case study is the Alpine-Mediterranean plate boundary zone, for which 8969 station vectors from 45 papers are merged into one lateral velocity field. To avoid pairing all GPS data through ~ 40 million integration paths, we utilize a new dartboard site connection algorithm that allows for decreasing the number of relative motion observations to a few million without impairing model quality. The model parametrization coupling the corresponding integral equations comprises a possible maximum of 4×691 and 2×98 unknown velocity gradient tensor and surface fault slip components, respectively, at 584 model nodes spanning 1111 spherical triangles. Large triangles characterize data-deficient areas where we constrain the inverse problem with synthetic data and strain rate damping. Subsequently, 43 GPS datasets are corrected for network Euler rotations (i.e. 3×43 unknowns) relative to a chosen reference network. This enables us to average co-located observations into single vectors, which reduces the computation time of the forward problem, and to estimate rigid Euler velocities from four datasets enclosed by plate boundary faults that outline the Adriatic, Aegean, Anatolian, and Calabrian sub-regions in the model. Finally, we present a new approach to investigating intraplate deformation by comparing inversion of the geodetic observations with inverting the Euler motions at all data sites from the four sub-regions and major African, Arabian, and Eurasian plates. We find that inversion for the velocity gradient field and inactive or active fault creep results in the largest kinematic differences between the GPS and Euler motion inversions, reflecting internal deformation. The two inversion types show a significant fault-local data misfit especially in the Eastern Mediterranean Sea, being related to trade-offs between almost perfectly resolved velocity gradient and fault slip parameters where observations near faults are lacking. Our main conclusion is that the Spakman-Nyst method and its implementation can be efficiently applied to thousands of geodetic data points. We suggest to explore the trade-off complication before making further model interpretations.



Utrecht University

Table of Contents

1	Introduction	3
2	GPS Data Compilation	5
3	Methods	7
3.1	The Spakman-Nyst Method	7
3.1.1	The Observation Equation	7
3.1.2	The Forward and Inverse Problem	8
3.2	Data Connection Strategy	10
3.3	Post-processing Tools	12
4	Experiments	13
4.1	Model Parametrization	13
4.2	Synthetic Data Constraints and Strain Rate Damping	14
4.3	Network Euler Rotations	19
4.3.1	Correction for Relative Network Rotations and Site Multiples	19
4.3.2	Microplate Euler Poles	22
4.4	GPS and Euler Motion Inversions	22
4.4.1	Experiment Set-up	24
4.4.2	Inversion Results	24
4.4.2.1	Model Quality Estimators	27
4.4.2.2	Fault Slip, Rotation, and Strain Rate Solutions	27
5	Discussion	34
5.1	Mixed Parameter Inversions	34
5.2	Software Complications	35
5.3	Geodynamic Interpretation	35
6	Conclusions	36
	Acknowledgements	37
	Data and Software Availability	37
	References	37
	Appendix	41

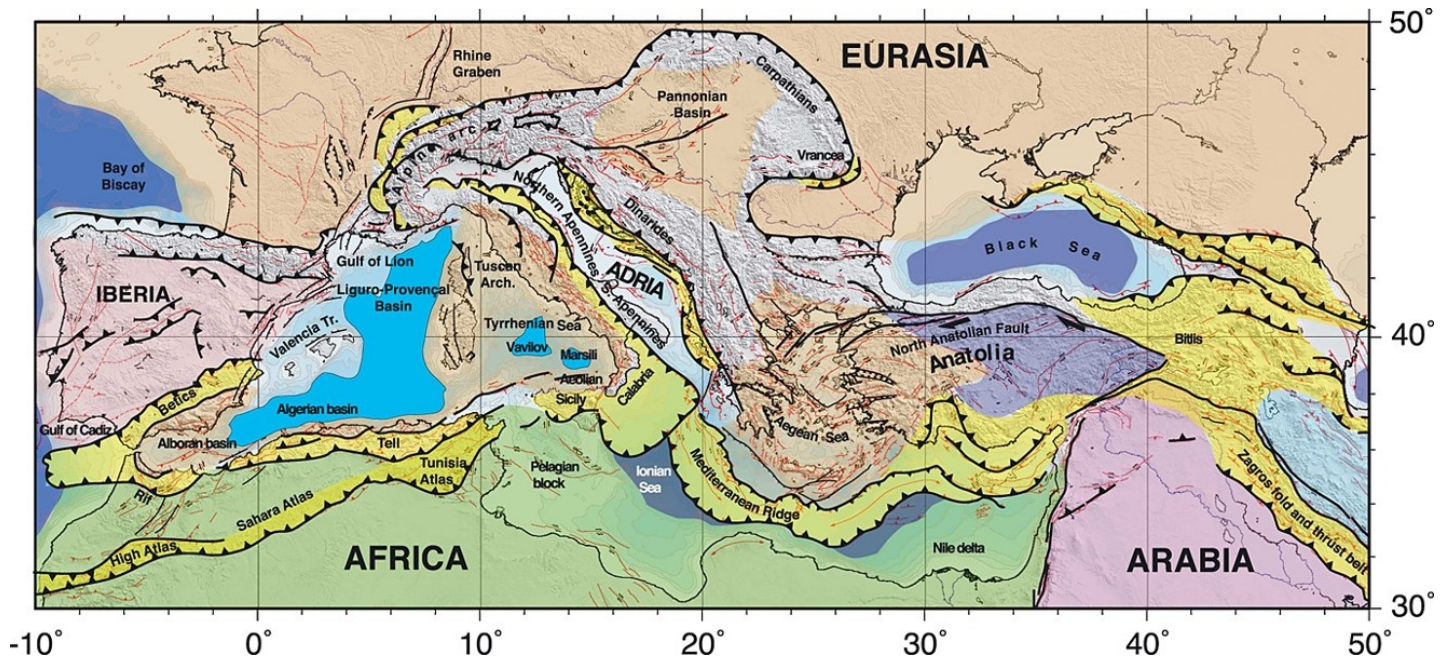


Figure 1: Plate tectonic setting and major geological attributes of the Mediterranean, taken from [Faccenna et al. \[2014\]](#), see Section 4.1 and Figure A.1 for the ways in which we adapted our model parametrization to this geological setting and other ones.

1 Introduction

Geodetic surface observations demonstrate that Earth’s tectonic plates deform internally, building upon the traditional plate tectonic view of crustal deformation being localized at the boundaries of rigidly rotating blocks. Furthermore, there is accumulating evidence that aseismic surface creep is active on faults besides co-seismic slip. During the last three decades, various kinematic techniques have been developed for relating observed surface velocities to intraplate strain, local rigid rotations, and/or fault creep [e.g. [Haines and Holt, 1993](#); [Lamb, 1994](#); [Shen et al., 1996](#); [Davies et al., 1997](#); [Bourne et al., 1998](#); [Ward, 1998](#); [Kahle et al., 2000](#); [Beavan and Haines, 2001](#); [Spakman and Nyst, 2002](#); [Cardozo and Allmendinger, 2009](#); [Hackl et al., 2009](#); [Tape et al., 2009](#); [Howe and Bird, 2010](#); [Kreemer et al., 2014](#); [Masson et al., 2014](#)]. However, while it is well-established by these studies that the kinematics of slow crustal deformation can be described by the underlying displacement or velocity gradient tensor field, i.e. strain and rotation rate fields, only a few studies incorporate fault motion into a kinematic theory [[Lamb, 1994](#); [Spakman and Nyst, 2002](#); [Howe and Bird, 2010](#)].

Notably, the paper by [Spakman and Nyst \[2002\]](#) presents a geophysical inversion method, hereafter called the Spakman-Nyst method, linking the relative velocity between any two surface observation points by line integration to the velocity gradient and fault creep parameters based on principles derived from seismic delay time tomography [e.g. [Bijwaard et al., 1998](#)]. A third unknown in the resulting integral equation concerns the Euler rotation between different geodetic networks, which is the same technical term as in other kinematic approaches [[Beavan and Haines, 2001](#); [Kreemer et al., 2014](#)]. The model parametrization, which allows for coupling many integral equations, is done by linear interpolation functions defined on triangular domains in the model space, leading to pure linear kinematic inversion of relative motion data without requiring any knowledge on crustal dynamics and rheology [[Spakman and Nyst, 2002](#)]. Next, the estimated kinematics can be compared to independent geological and seismological observations [[Bos et al., 2003](#); [Bos and Spakman, 2005](#)], and be interpreted in terms of geodynamic drivers [[Bos et al., 2003](#); [Spakman and Hall, 2010](#); [Spakman et al., 2018](#)].

We regard previous applications of the Spakman-Nyst method as being quite limited in two technical

aspects. First, to connect tens [Spakman and Hall, 2010] to hundreds [Bos et al., 2003; Bos and Spakman, 2005; Spakman et al., 2018] of satellite Global Positioning System (GPS) observations in problems of regional deformation, the basic practice has been to simply include all possible data combinations. Whereas this approach may be appropriate for such dataset sizes, a more advanced site connection procedure would be needed in case thousands of published GPS observations covering a large region like the Mediterranean are involved, since an inversion combining all of these data can be computationally expensive, and because relative motion connections between widely spaced stations may not be that helpful for inversion. So far, an actual strategy has not been proposed. Second, the possibility of inverting for geodetic network rotations has been largely overlooked. The inversion type has been tested once [Spakman and Hall, 2010], but solely on three combined datasets and is discussed only very briefly. Its potential for tens of merged GPS velocity fields remains unknown.

The goal of our research is to technically improve on above studies by finding ways to apply the Spakman-Nyst method to thousands of GPS observations acquired from tens of different studies performed in a wide complex plate boundary zone like the Alpine-Mediterranean arc. To first-order, this region has been shaped by a long geological history of interplay between the converging African, Arabian, and Eurasian plates, Calabrian, Gibraltarian, and Hellenic subduction systems, and internally deforming Adriatic, Aegean, and Anatolian crustal blocks [e.g. Wortel and Spakman, 2000; Reilinger et al., 2006; Serpelloni et al., 2007; D’Agostino et al., 2008; Faccenna et al., 2014; Van Hinsbergen et al., 2020] (Figure 1).

We use the pre-2014 available continuous GPS data as provided by Kreemer et al. [2014], and compile 44 more recent datasets [e.g. Metois et al., 2015; Palano et al., 2015; Bougrine et al., 2019; D’Agostino et al., 2020; Gomez et al., 2020] to estimate the kinematics of present-day surface deformation in the Mediterranean Region. In a unique series of experiments, we invert thousands of GPS observations for different kinematic parametrizations with a newly devised site connection algorithm, and correct for uniform rotational differences between the 45 combined GPS motion datasets. Particularly, we kinematically assess homogeneous plate rotation in key parts of the Mediterranean and the intraplate deformation component of the geodetic data, constituting preliminary work to future research that focuses on geodynamical interpretation and on modelling deformation in the Central and Eastern Mediterranean in more detail.

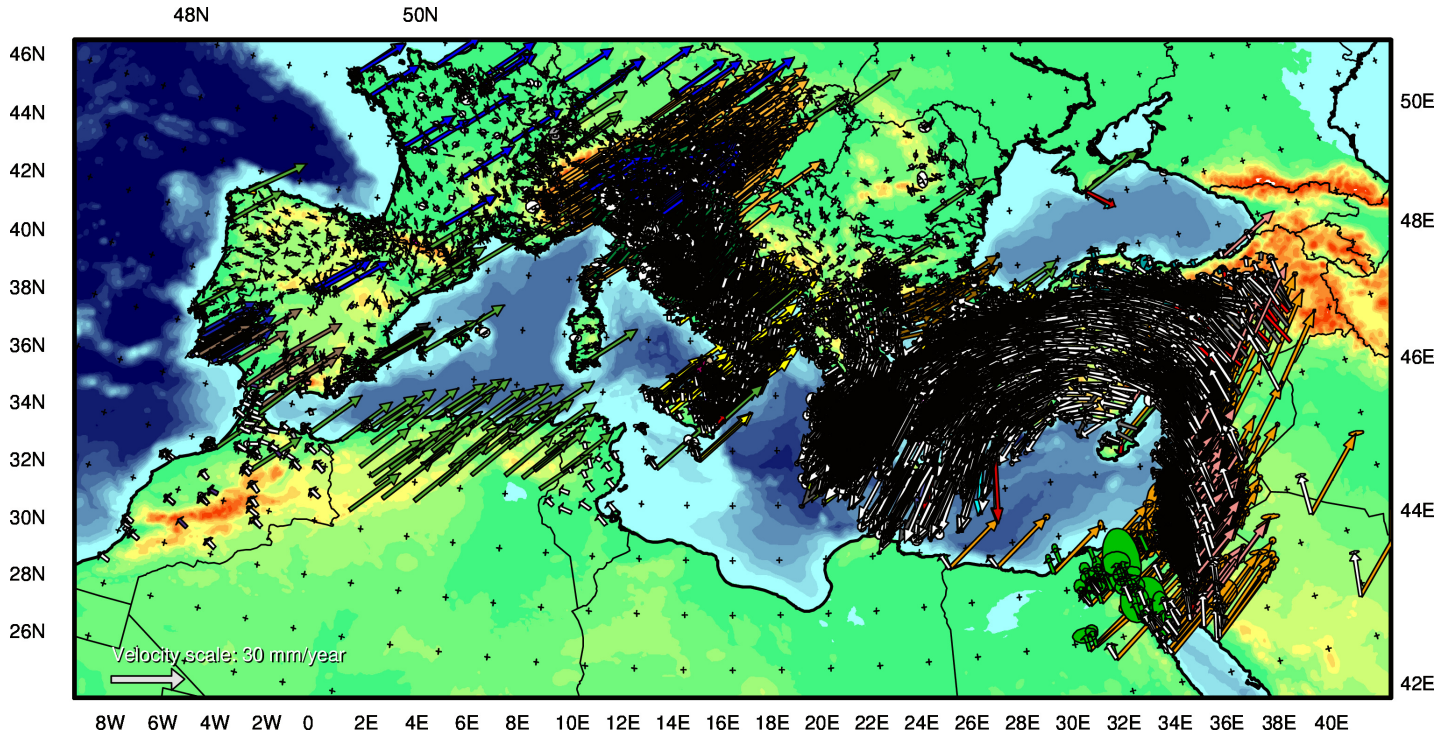


Figure 2: Compiled 8969 GPS vectors of the Mediterranean together with their 95% confidence error ellipses. Each of the 45 geodetic networks is presented in its published reference frame, e.g. the global [Kreemer et al. \[2014\]](#) (in white) and Algerian [Bougrine et al. \[2019\]](#) (green) datasets are tied to the Eurasian and ITRF2014-frames, respectively. Note that the Tunisian [Bahrouni et al. \[2020\]](#) network (also in white) has been added to the Kreemer dataset, see Section 4.3.1 for details, and that the 25 data outliers in Figure A.6 have already been deleted from the compilation. Moreover, note that we decide to incorporate the Egyptian [Saleh and Becker \[2015\]](#) (green) and [Pietrantonio et al. \[2016\]](#) (orange) networks into our dataset despite their large error ellipses since Egypt is poorly sampled by the Kreemer dataset alone (Figure A.2).

2 GPS Data Compilation

Following the increasing availability of GPS data over the last three decades, many geodetic studies of crustal deformation have been conducted in the Mediterranean [e.g. [Kreemer et al., 2014](#); [Metois et al., 2015](#); [Palano et al., 2015](#); [Saleh and Becker, 2015](#); [Nguyen et al., 2016](#); [Serpelloni et al., 2016](#); [Sánchez et al., 2018](#); [Bougrine et al., 2019](#); [Özdemir and Karshoğlu, 2019](#); [Bahrouni et al., 2020](#); [Civiero et al., 2020](#); [D’Agostino et al., 2020](#); [Gomez et al., 2020](#)]. This allows us to create from issued datasets an extensive regional compilation of surface motions.

Figure 2 shows the spherical box with southwestern (-11° , 34°) and northeastern (43° , 50°) longitude-latitude corners inside which geodetic data is collected for our research. Published data consist of continuous GPS (CGPS) and episodic survey GPS (SGPS) data from permanent stations and campaign-style measurements, respectively, capturing the long-term interseismic crustal deformation field over a period of several (≥ 2) years at minimum (Table A.1). Seven parameters serve as the necessary input for a kinematic experiment, being the east and north components of the data locations, velocities, and velocity standard deviations, and their east-north data correlation if documented, else put to zero. Unless reported otherwise, we assume $1-\sigma$ data variances and geographical (ellipsoidal) site coordinates, which we then convert to spherical coordinates.

In the end, 8969 GPS vectors from 45 papers are merged into one Mediterranean horizontal motion field (Figure 2; Table A.1). As is evident from Figure 2 and Table A.1, the 45 datasets have been determined relative to different plate motion and global geodetic frames such as the Eurasia-fixed, No-Net-Rotation (NNR), and International Terrestrial Reference frames (ITRF). To be able to reliably analyse surface velocities, all data have to be rotated into a common plate motion reference frame. In the Spakman-Nyst method, this

is done by correcting for uniform network rotations relative to a reference dataset, see Section 3.1.1 and 4.3.1 for technical details and experiments. We adopt the worldwide data compilation by [Kreemer et al. \[2014\]](#), hereafter the Kreemer dataset, as the reference network since it is by far our largest and most widely distributed dataset with 3981 vectors (Figure A.2), and because all motions have been homogeneously transformed into the same reference frame [[Kreemer et al., 2014](#)], here the Eurasian frame. The 4988 velocities from the 44 post-[Kreemer et al. \[2014\]](#) studies (Figure A.3) comprise both newly published observation sites in areas poorly covered by the Kreemer network, e.g. Algeria [[Bougrine et al., 2019](#)], the central Balkans (Bulgaria, Serbia, Montenegro) [[Metois et al., 2015](#); [D’Agostino et al., 2020](#)], the southern Black Sea region [[Ergintav et al., 2014](#); [Aktuř et al., 2015](#); [Özdemir and Karshođlu, 2019](#)], Egypt [[Saleh and Becker, 2015](#); [Pietrantonio et al., 2016](#); [Gomez et al., 2020](#)], and Tunisia [[Bahrouni et al., 2020](#)], and numerous reprocessed measurements at station locations shared with the Kreemer dataset. Such network overlap is used to invert for relative network rotations (Section 3.1.1, 3.2, 4.3.1).

After visual inspection of all networks in the Kreemer Eurasia frame (Figure A.4-A.5), 25 vectors clearly not representing regionally consistent motion, i.e. data outliers, have been removed (Figure A.6). We choose to not delete data based on their error ellipses, e.g. in Egypt [[Saleh and Becker, 2015](#); [Pietrantonio et al., 2016](#)] (Figure 2, A.4-A.5), noting that the influence of noisy data on the model solution is weighed down by the inversion anyway. Given the difficulty to check thousands of GPS observations individually, we suppose the 45 papers to have already correctly identified and discarded most data outliers, and focus the search for outliers on Algeria and Tunisia where data are relatively sparse, meaning that outlying data may dominate the inverse problem in these model parts where the number of relative motion data would be especially low. 16 vectors excluded from interpretation by [Bougrine et al. \[2019\]](#) and [Bahrouni et al. \[2020\]](#) have been removed (Figure A.6).

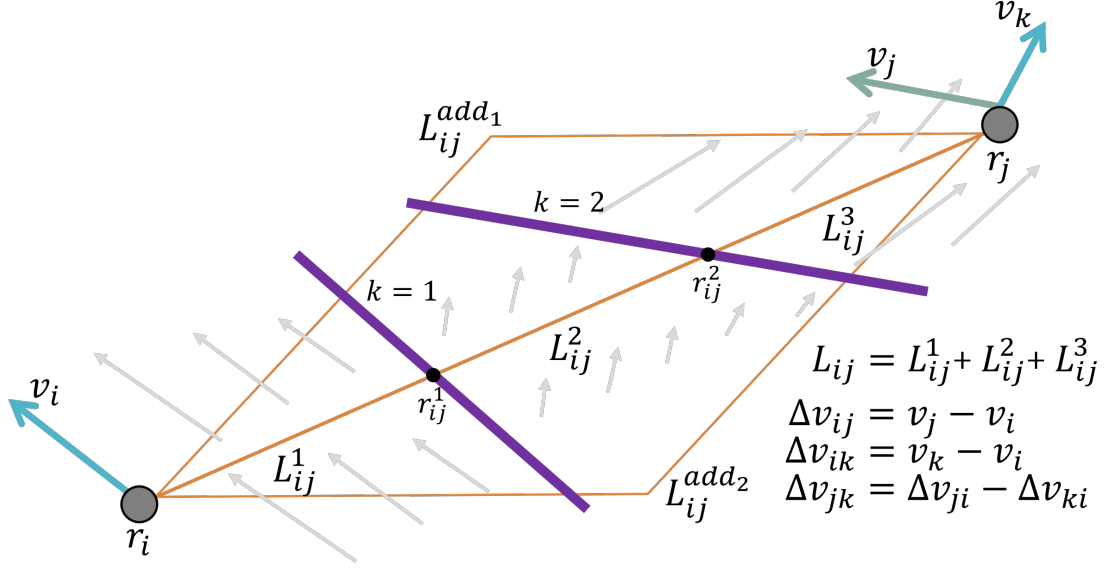


Figure 3: Forward problem of linking relative motion vector $\Delta\mathbf{v}_{ij}$ or $\Delta\mathbf{v}_{ik}$ between observation sites i and j to the geodesic L_{ij} or any other arbitrary (additional) integration path L_{ij}^{add} over the unknown velocity gradient field $\nabla\mathbf{v}$. Integration over $\nabla\mathbf{v}$ is done by parts such that $\nabla\mathbf{v}$ can be discontinuous across faults. The "true" crustal flow field (grey vectors) would have to be kinematically estimated from $\nabla\mathbf{v}$ and possible surface fault creep \mathbf{f}_k , here the slip vectors $\mathbf{f}_{1,2}$ at intersections $r_{ij}^{1,2}$ between the faults and L_{ij} . A third geodetic (i.e. technical) contribution to $\Delta\mathbf{v}_{ij}$ is, taking the blue network of \mathbf{v}_i and \mathbf{v}_k as the reference dataset, an unknown Euler rotation $\boldsymbol{\Omega}_j \times r_j$ of \mathbf{v}_j with respect to \mathbf{v}_i . In the case of relative motion $\Delta\mathbf{v}_{jk} = \Delta\mathbf{v}_{ji} - \Delta\mathbf{v}_{ki}$ between the co-located observations \mathbf{v}_j and \mathbf{v}_k , it would be simply equivalent to $-\boldsymbol{\Omega}_j \times r_j$.

3 Methods

We use the inversion method developed by Spakman and Nyst [2002] to estimate the strain and rotation rate fields, surface fault slip/creep, and GPS network rotations from relative motion data in the Mediterranean. The theory behind the technique is explained in line with the current *Tetra* software implementation.

3.1 The Spakman-Nyst Method

The Spakman-Nyst method describes the observed relative motion between any two positions at the surface in terms of the kinematics underlying crustal deformation. This description is purely kinematic, so does not depend on assumptions of crustal dynamics and rheology.

3.1.1 The Observation Equation

At any two sites i and j , the measured velocity vectors \mathbf{v}_i and \mathbf{v}_j can be connected by an integration path L_{ij} of arbitrary geometry along which an unknown surface deformation field is to be estimated from the relative motion $\Delta\mathbf{v}_{ij} = \mathbf{v}_j - \mathbf{v}_i$ (Figure 3). $\Delta\mathbf{v}_{ij}$ is linked to the velocity gradient field $\nabla\mathbf{v}$, surface creep \mathbf{f}_k on fault segment k , and geodetic network rotation vectors $\boldsymbol{\Omega}_{i,j}$ by the observation equation [Spakman and Nyst, 2002]

$$\Delta\mathbf{v}_{ij} = \sum_{l=1}^{K+1} \int_{L_{ij}^l} \nabla\mathbf{v}(\mathbf{r}) \cdot d\mathbf{r} + \sum_{k=1}^K \alpha_k \mathbf{f}_k(r_{ij}^k) + \boldsymbol{\Omega}_j \times r_j - \boldsymbol{\Omega}_i \times r_i \quad (1)$$

where L_{ij}^l is the l^{th} path segment on L_{ij} , which crosses K fault segments, $\nabla\mathbf{v}(\mathbf{r})$ is the velocity gradient field as a function of position \mathbf{r} , α_k is a factor ± 1 controlled by the fault orientation relative to the direction of integration, \mathbf{f}_k is the fault slip rate vector on segment k at the intersection r_{ij}^k between L_{ij}^l and the fault

segment, and $\mathbf{\Omega}_j \times r_j - \mathbf{\Omega}_i \times r_i$ is the Euler rotation difference $\mathbf{\Omega}_m$ between the observation networks at site locations r_j and r_i . Eq. (1) has the following notable properties: (1) it is implemented in a spherical coordinate frame; (2) it is exact in practice, i.e. compared to the error in $\Delta \mathbf{v}_{ij}$ the theoretical errors in $\nabla \mathbf{v}$, \mathbf{f}_k and $\mathbf{\Omega}_m$ are negligibly small; (3) it is purely linear in the three unknown quantities; and (4) it offers a complete kinematic description of the relative crustal motion $\Delta \mathbf{v}_{ij}$, which is assumed to reflect the interseismic velocity field.

The first part on the right-hand side of Eq. (1) represents the contribution of distributed surface deformation to $\Delta \mathbf{v}_{ij}$. Partial integration over the velocity gradient field allows $\nabla \mathbf{v}$ to be discontinuous across the K faults (Figure 3). The velocity gradient tensor is composed of the strain rate field $\boldsymbol{\epsilon} = 1/2(\nabla \mathbf{v} + (\nabla \mathbf{v})^T)$ (symmetric part) and rotation rate field $\boldsymbol{\omega} = 1/2(\nabla \mathbf{v} - (\nabla \mathbf{v})^T)$ (antisymmetric part) according to $\nabla \mathbf{v} = \boldsymbol{\epsilon} + \boldsymbol{\omega}$. In the spherical 2D ϕ, θ -coordinate frame, this identity becomes

$$\begin{bmatrix} v_{\phi\phi} & v_{\phi\theta} \\ v_{\theta\phi} & v_{\theta\theta} \end{bmatrix} = \begin{bmatrix} \epsilon_{\phi\phi} & \epsilon_{\phi\theta} \\ \epsilon_{\phi\theta} & \epsilon_{\theta\theta} \end{bmatrix} + \begin{bmatrix} 0 & -\omega_{\theta\phi} \\ \omega_{\theta\phi} & 0 \end{bmatrix} \quad (2)$$

where the $\nabla \mathbf{v}$ -tensor consists of the lateral velocity derivatives, which can be decomposed into the associated strain and rotation rate components. Note that $\epsilon_{\theta\phi} = \epsilon_{\phi\theta}$, $\omega_{\phi\theta} = -\omega_{\theta\phi}$, and that there are effectively three strain rate components and one rotation rate component to be calculated: $\epsilon_{\phi\phi}$, $\epsilon_{\phi\theta}$, $\epsilon_{\theta\theta}$, and $\omega_{\theta\phi}$. Eq. (2) is used to model horizontal deformation at the surface in a two-dimensional spherical geometry independently of the radial velocity derivatives, which are not considered here. In the Tetra software, Eq. (2) is substituted into Eq. (1) to directly solve for $\boldsymbol{\epsilon}$ and $\boldsymbol{\omega}$.

The second and third right-hand side Eq.(1)-parts relate $\Delta \mathbf{v}_{ij}$ to a step in crustal motion at faults and to a possible relative network rotation. The total fault motion results from surface slip on the K faults intersected by a path L_{ij} (Figure 3). A significant GPS network rotation may exist between the velocity vectors \mathbf{v}_i and \mathbf{v}_j if they have been established with respect to (slightly) different reference frames, e.g. ITRF2008 and ITRF2014. One of the vectors can be set to zero, such that the Euler rotation relative to the corresponding network is solely described by $\mathbf{\Omega}_i$ or $\mathbf{\Omega}_j$ (Figure 3). Note that \mathbf{f}_k and $\mathbf{\Omega}_m$ respectively consist of two fault-normal and -parallel, and three east, north, and radial vector components.

3.1.2 The Forward and Inverse Problem

Generalizing the single i - j data pair to a set of J geodetic observations enables many unique i - j combinations to be incorporated into a dataset of relative motions between sites (Section 3.2). The number of observation equations (1) rendered by such strategy is

$$N \leq \frac{J(J-1)}{2} \quad (3)$$

where N equals $J(J-1)/2$ if all data were to be uniquely paired. The N equations (1) are coupled through geodesics L_{ij} or other great circle integration paths that sample a triangulated model domain (Figure 3, 5). This study region is divided into a set of M model nodes spanned by triangulation, with the components of $\nabla \mathbf{v}$ and \mathbf{f}_k being the model parameters at the nodes and fault segments, respectively. Two parametrizations are substituted into Eq. (1) to obtain a linear matrix system. First, a linear dependence of $\nabla \mathbf{v}$ on the spatial coordinates in each triangle is adopted, allowing for quadratic velocity in triangles and for continuity of $\nabla \mathbf{v}$ across vertices. Secondly, \mathbf{f}_k is implemented as a linear variation of fault slip between the segment endpoints, which deviates from the description in Spakman and Nyst [2002] where \mathbf{f}_k is parametrized as a segment-dependent constant rate.

The ordinary set of N coupled equations (1) can be assembled into matrix-vector form written as $\mathbf{A}\mathbf{m} = \mathbf{d}$, where \mathbf{A} is the observation matrix collecting the L_{ij}^l - and α_k -coefficients, \mathbf{m} is the model parameter vector, and \mathbf{d} is the relative motion data vector of minimum length N . The N equations (1) can be extended with additional integration paths using the same $\Delta \mathbf{v}_{ij}$ dataset since the relative motion between two points is independent of the choice of L_{ij} (Figure 3). Extra data connections help to better constrain a locally underdetermined inverse problem in areas with a detailed triangulation and restricted amount of observations. Furthermore, they ensure that the model is a deformation field by forcing internal consistency between $\nabla \mathbf{v}$

and \mathbf{f}_k across faults, and by constraining the velocity gradient field to be curl-free ($\nabla \times \nabla \mathbf{v} = \mathbf{0}$) in the special case of closed path loops $L_{ij} - L_{ji}$, which always yield zero relative motion. Closed paths can be explicitly included in Tetra at present because the curl-free parametrization from Spakman and Nyst [2002] is not implemented. By default, Tetra produces circular and triangular loops around model nodes and inside triangles along the vertices, respectively. Attaching these additional path equations to $\mathbf{A}\mathbf{m} = \mathbf{d}$ defines the extended data vector $\hat{\mathbf{d}} = [\mathbf{d} \ \mathbf{0}]^T$.

Inversion of our matrix-vector system leads to practical issues due to the non-unique choice of L_{ij} and inconsistencies in the set of observation equations associated with data errors. To deal with non-uniqueness, data errors, and ill-conditioning of the matrix, an inversion procedure is utilized that selects a solution minimizing both the data residual in a least squares sense, and some model norm as regulated by damping. The model is damped by appending equations of the form $\alpha \mathbf{D}\mathbf{m} = \mathbf{0}$ to $\mathbf{A}\mathbf{m} = \hat{\mathbf{d}}$, where α is a tuning parameter controlling the trade-off between the data misfit and weighed model norm, and \mathbf{D} is a damping matrix. The regularization equations implemented in Tetra allow for amplitude damping of all model parameters, first derivative damping of fault slip rate, and second derivative damping of the velocity gradient field to either uniformly or locally regulate the solution.

The object function to be minimized in the regularized least squares is [Spakman and Nyst, 2002]

$$\Phi(\mathbf{m}) = (\hat{\mathbf{d}} - \mathbf{A}\mathbf{m})^T \mathbf{C}_d^{-1} (\hat{\mathbf{d}} - \mathbf{A}\mathbf{m}) + \alpha_0^2 \mathbf{m}^T \mathbf{m} + \alpha_1^2 \mathbf{m}^T \mathbf{D}_1^T \mathbf{D}_1 \mathbf{m} + \alpha_2^2 \mathbf{m}^T \mathbf{D}_2^T \mathbf{D}_2 \mathbf{m} \quad (4)$$

where \mathbf{C}_d is the covariance matrix of relative motion data, $\mathbf{D}_{1,2}$ are the first and second derivative damping operators, and $\alpha_{0,1,2}$ are the weighing factors of amplitude and derivative damping. The inverse of the data covariance matrix would be challenging, if not impossible, to compute owing to its size of N by N elements. Therefore, \mathbf{C}_d is taken as a diagonal matrix built only from the standard deviations belonging to data vector $\hat{\mathbf{d}}$ [Bos et al., 2003]. The regularized least squares solution minimizing $\Phi(\mathbf{m})$ is [Spakman and Nyst, 2002]

$$\tilde{\mathbf{m}} = (\mathbf{A}^T \mathbf{C}_d^{-1} \mathbf{A} + \alpha_0 \mathbf{I} + \alpha_1^2 \mathbf{D}_1^T \mathbf{D}_1 + \alpha_2^2 \mathbf{D}_2^T \mathbf{D}_2)^{-1} \mathbf{A}^T \mathbf{C}_d^{-1} \hat{\mathbf{d}} \quad (5)$$

where \mathbf{I} is the identity matrix for amplitude damping, and with the respective expressions of the posteriori model covariance and model resolution kernel, which denotes the linear dependence between model parameters, given by [Spakman and Nyst, 2002]

$$\mathbf{C} = (\mathbf{A}^T \mathbf{C}_d^{-1} \mathbf{A} + \alpha_0 \mathbf{I} + \alpha_1^2 \mathbf{D}_1^T \mathbf{D}_1 + \alpha_2^2 \mathbf{D}_2^T \mathbf{D}_2)^{-1} \quad (6)$$

$$\mathbf{R} = \mathbf{C} \mathbf{A}^T \mathbf{C}_d^{-1} \mathbf{A} \quad (7)$$

where $\mathbf{R} = \mathbf{I}$ implies that the model parameters are perfectly linearly resolved. More specifically, the model resolution kernel maps the ideal ("true") solution vector \mathbf{m}_{true} of unknown $\nabla \mathbf{v}$ -, \mathbf{f}_k -, and/or Ω_m -parameters, as projected upon the linear model parametrization, onto the inversion solution $\tilde{\mathbf{m}}$ (5) with [Rawlinson and Spakman, 2016]

$$\tilde{\mathbf{m}} = \mathbf{R} \mathbf{m}_{true} \quad (8)$$

where $\tilde{\mathbf{m}} = \mathbf{m}_{true}$ if $\mathbf{R} = \mathbf{I}$, see Section 5.1 for discussion. The model resolution and covariance matrices constitute the main model quality estimators in Tetra together with the data misfit $\mathbf{e} = \mathbf{d} - \mathbf{A}\tilde{\mathbf{m}}$ and velocity field prediction (Section 3.3).

From Eq. (4) to (7), the model-normalized data misfit χ_ν^2 , average solution amplitude \tilde{s}_m , average standard deviation $\tilde{\sigma}_m$, and average resolution \tilde{r}_m can be derived, respectively: [Bos et al., 2003]

$$\chi_\nu^2 = \frac{1}{\nu} \sum_{i=1}^N \frac{e_i^2}{\sigma_i^2} \quad (9)$$

$$\tilde{s}_m = \frac{1}{M} \sum_{i=1}^M \tilde{m}_i \quad (10)$$

$$\tilde{\sigma}_m = \frac{1}{M} \sum_{i=1}^M \sqrt{C_{ii}} \quad (11)$$

$$\tilde{r}_m = \frac{1}{M} \sum_{i=1}^M R_{ii} \quad (12)$$

where M is the number of model parameters, $\nu = N - M$ is the degree of model freedom, σ_i is the $1\text{-}\sigma$ data variance, and C_{ii} and R_{ii} are the diagonal elements of the model covariance (6) and model resolution (7) matrices. Since the degrees of freedom are high for the millions of relative motion data and thousands of model parameters in the Mediterranean model ($N \gg M$; Section 3.2, 4.1), we ideally want a data fit of $\chi_\nu^2 \sim 1$. Meanwhile, we aim for solutions with little regularization, a proper covariance, i.e. model standard deviations that are much smaller than the model amplitudes ($\tilde{\sigma}_m/\tilde{s}_m \ll 10\%$), and a proper resolution ($\tilde{r}_m \sim 1$).

3.2 Data Connection Strategy

Integration over the Mediterranean dataset is carried out numerically with Tetra. Geodetic observations are combined by looping over the Tetra input file containing the spherical site coordinates, the east and north velocity, standard deviation and data correlation components, and station codes. For us, the basic data file consists of the 8969 GPS vectors compiled from the 45 papers.

The most straight-forward way of connecting the data is to uniquely pair them all, which requires $8969(8969 - 1)/2$ (~ 40.217 million) observation equations (1). However, solving tenths of millions of coupled equations (1) is impractical due to the intensity of computing the coefficient matrices \mathbf{A} , \mathbf{A}^T , and $\mathbf{A}^T \mathbf{A}$. In addition, it is unnecessary to link data from opposite sides of the model domain, e.g. in Bitlis and Iberia, when there are locally already enough data to constrain the solution. If sites are absent over large distances, e.g. in between Algerian and Egyptian stations, the need to integrate across the unsampled region can be omitted by inserting synthetic data of rigid plate motion here (Section 4.2). On the other hand, combining vectors taken from different studies and sharing the same site, i.e. site multiples, is also not needed because their network Euler rotation can be calculated using the two velocities with respect to another station (Figure 3).

For these reasons, we invert subsets of the 40.217 million relative motion data rather than all of them. To select data subsets, the Tetra matrix program is employed. A double i - j Fortran loop is implemented that, for any fixed datum with record number i , loops over data j in an arbitrarily sorted data file of length J (e.g. 8969), where $i = 1, \dots, J - 1$ and $j = i + 1, \dots, J$. The criteria by which certain data j are linked to datum i define the data connection strategy. Initially, the Tetra code combined observations within a preset distance interval. This procedure proved to be unwarrantedly dependent on the ordering of the input data array. That is, by permuting the geographical (longitude or latitude) or alphabetical (station code) order of file entries before inversion, somewhat different solutions appeared using the original software, see Section 5.2 for further discussion.

The old "distance" strategy has been replaced with a "dartboard" algorithm in an attempt to assure an azimuthally balanced spread of relative motion pairs (Figure 4; Table 1). Around each datum i , a cylindrical mesh of azimuthal and angular distance intervals is centred. Within the dartboard-like grid, all available i - j combinations are scanned with the restriction that no more than n'_{max} links can be generated in each azimuth-distance segment following

$$n'_{max} = \max \left(1, \text{nint} \left(n_{max} * \frac{A_{segment}}{A_{dartboard}} \right) \right) \quad (13)$$

where max and $nint$ are elemental Fortran functions, n_{max} is the user-set maximum number of allowed connections in the entire dartboard, $A_{segment}$ is the surface area of a particular sector, and $A_{dartboard}$ is the dartboard surface area. Note that if the number of possible i - j pairs in a segment exceeds n'_{max} , an implicit bias against the excluded data listed after the n'_{max} -th linked datum j occurs, see Section 5.2 for discussion.

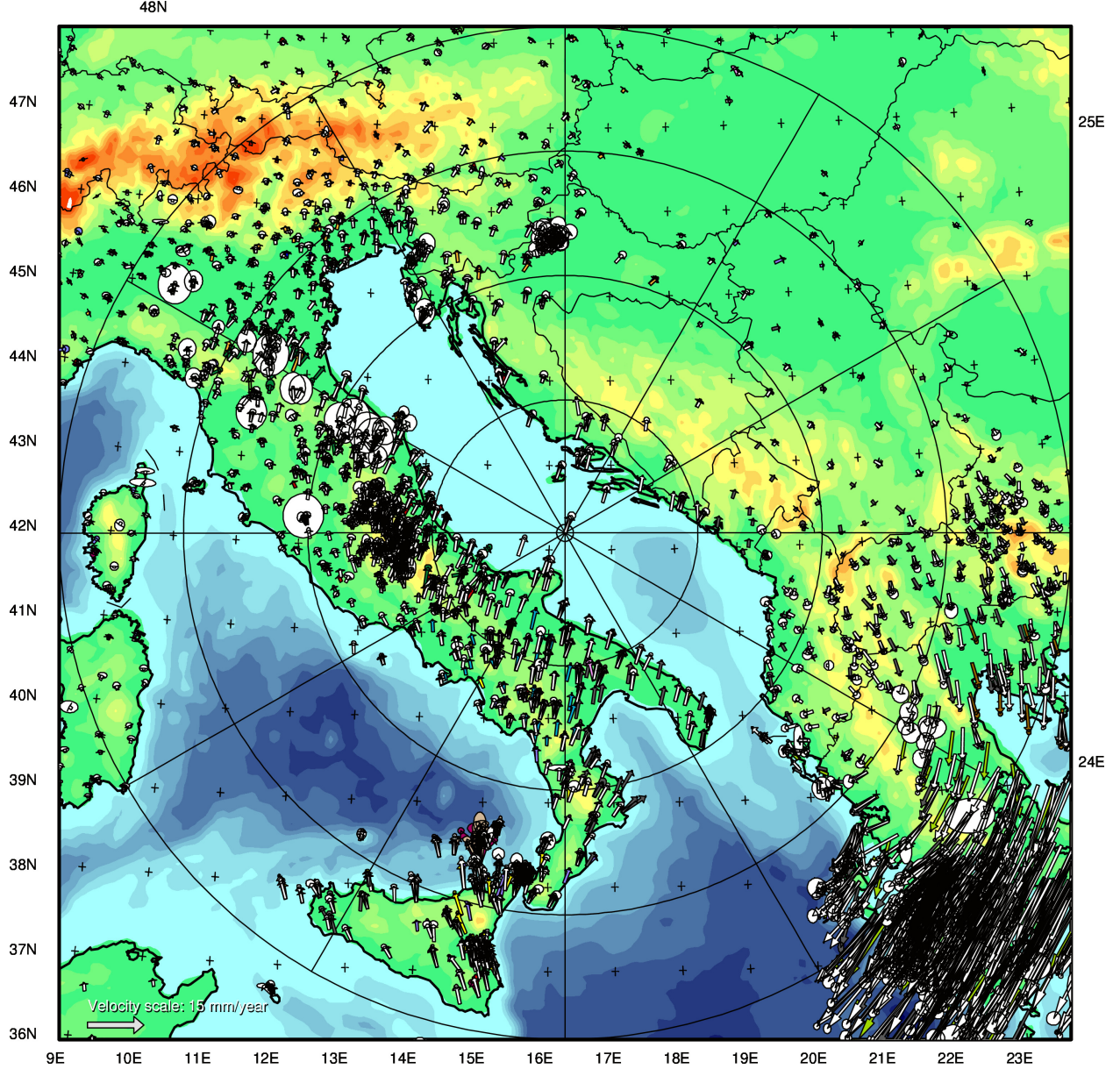


Figure 4: Data connection dartboard of radius 5.9° (~ 649 kilometres) around an isolated station in the central Adriatic Sea, see Table 1 for the number of integration paths made inside each of the 48 azimuth-distance sectors. The site vectors with 95% confidence error ellipses plotted here are part of the 8969 GPS observations corrected for network rotations relative to the Kreemer Eurasia dataset, but left in their original 43 network colours, see Figure A.5 for the entire dataset.

<i>azimuth</i> ($^\circ$):	30	60	90	120	150	180	210	240	270	300	330	360
$d = 1.6^\circ$	11	4	1	0	0	11	11	11	11	4	0	5
$d = 3.0^\circ$	0	7	14	13	26	32	32	32	32	32	16	24
$d = 4.5^\circ$	14	16	22	52	35	25	52	4	8	52	52	52
$d = 6.0^\circ$	23	7	66	72	72	0	72	14	17	57	72	67

Table 1: Number of i - j data combinations made within each of the 48 azimuth-distance dartboard segments from Figure 4, where azimuth is measured clockwise, d denotes the distance away from central datum i , and the applied dartboard settings are $d_{min} = 0.1^\circ$, $d_{max} = 6^\circ$, $n_{max} = 2000$, and $i_{multiples} = 1$. Note that the dartboard strategy optimizes a both azimuthal and distance homogeneity in site connections, e.g. whereas only 32 pairs have been produced in the 300° - 3.0° sector of high data density, 16 of them have been created in the adjacent sparse 330° - 3.0° sector.

However, its effects on inversion are negligible when an appropriate dartboard geometry is used, covering 12 azimuthal intervals of 30° and 4 distance intervals in our study (Figure 4; Table 1). Furthermore, some observations located in a dartboard field around i may already be paired with this datum (now j) in their own dartboard.

In a typical dartboard experiment, we adjust n_{max} , the dartboard size as defined by a minimum (d_{min}) and maximum (d_{max}) radial distance away from the centre, and the option ($i_{multiples}$) to incorporate site multiples, where $i_{multiples} = 0, 1$, respectively meaning that multiples are either omitted or included. Data j are identified as site multiples within $d_{multiples} \times d_{multiples}$ blocks of a local mesh projected on the dartboard of each datum i , where $d_{multiples}$ is an arc distance, normally chosen to be a few kilometres ($\sim 0.01^\circ$). Usually, if at the same location multiple data j are present, solely the first one encountered in the loop is combined with datum i ($i_{multiples} = 0$), unless connection to all of them is enabled ($i_{multiples} = 1$), being a good strategy for estimating relative network rotations (Section 4.3.1).

3.3 Post-processing Tools

A powerful tool for our analysis of acceptable models is the posteriori computation of a crustal flow field on a regular synthetic grid covering the triangulation (Figure 12). At each grid point i , a single velocity vector \mathbf{v}_i^{pred} is calculated by averaging the motion vectors deduced from the predicted relative motions $\Delta\mathbf{v}_{ij}^{pred}$ between node i and all P available data j found within a dartboard centred around i , i.e.

$$\mathbf{v}_i^{pred} = \frac{1}{P} \sum_{j=1}^P \left[\mathbf{v}_j^{datum} + \Delta\mathbf{v}_{ij}^{pred} \right] \quad (14)$$

where \mathbf{v}_j^{datum} is a velocity vector linked to virtual site i , and $\Delta\mathbf{v}_{ij}^{pred}$ is predicted by integration of the inversion model along the geodesic pairing i with j . This relative velocity is extracted from the vector \mathbf{d}^{pred} that assembles all synthetic station-real observation relative motions gathered within the dartboard. \mathbf{d}^{pred} is computed as

$$\mathbf{d}^{pred} = \mathbf{A}^{pred} \tilde{\mathbf{m}} \quad (15)$$

where \mathbf{A}^{pred} is the matrix of integration path coefficients, and $\tilde{\mathbf{m}}$ is the solution vector (5) of estimated $\nabla\mathbf{v}$ - and \mathbf{f}_k -parameters. Errors in $\tilde{\mathbf{m}}$ are assumed to be purely reflected in the scatter of the P predicted velocities. The corresponding mean 1- σ standard deviation, or prediction error, of vector \mathbf{v}_i^{pred} is a useful indicator of local model uncertainty. In Tetra, above prediction method is also applied to the computation of data misfit vectors using $\mathbf{v}_i^{misfit} = \mathbf{v}_i^{datum} - \mathbf{v}_i^{pred}$, in which case \mathbf{d}^{pred} collects all dartboard relative motions connecting a real datum i to data j .

Importantly, Tetra requires removal of all relative network Euler rotations prior to the calculation of an interpretable flow field. In addition, rotation into a reference velocity frame allows for averaging multiple observations at common points into single vectors. Regarding the numerous site multiples in the Mediterranean, the advantage of averaging multiples is a substantial decrease in computation time of the forward problem. Observations are identified as multiples on a high resolution mesh similarly to the dartboard strategy. If n vectors share a grid cell (i.e. location), they are averaged by summing the variances of each vector component, ignoring error correlations between the multiples, with

$$\sigma_{avg} = \sqrt{\frac{1}{n} \sum_{i=1}^n \sigma_i^2} \quad (16)$$

where σ_i is the east or north standard deviation of the i -th multiple, and σ_{avg} is the averaged component. Note that the simple approach from Eq. (16) is supported by the generally highly variable error of GPS data.

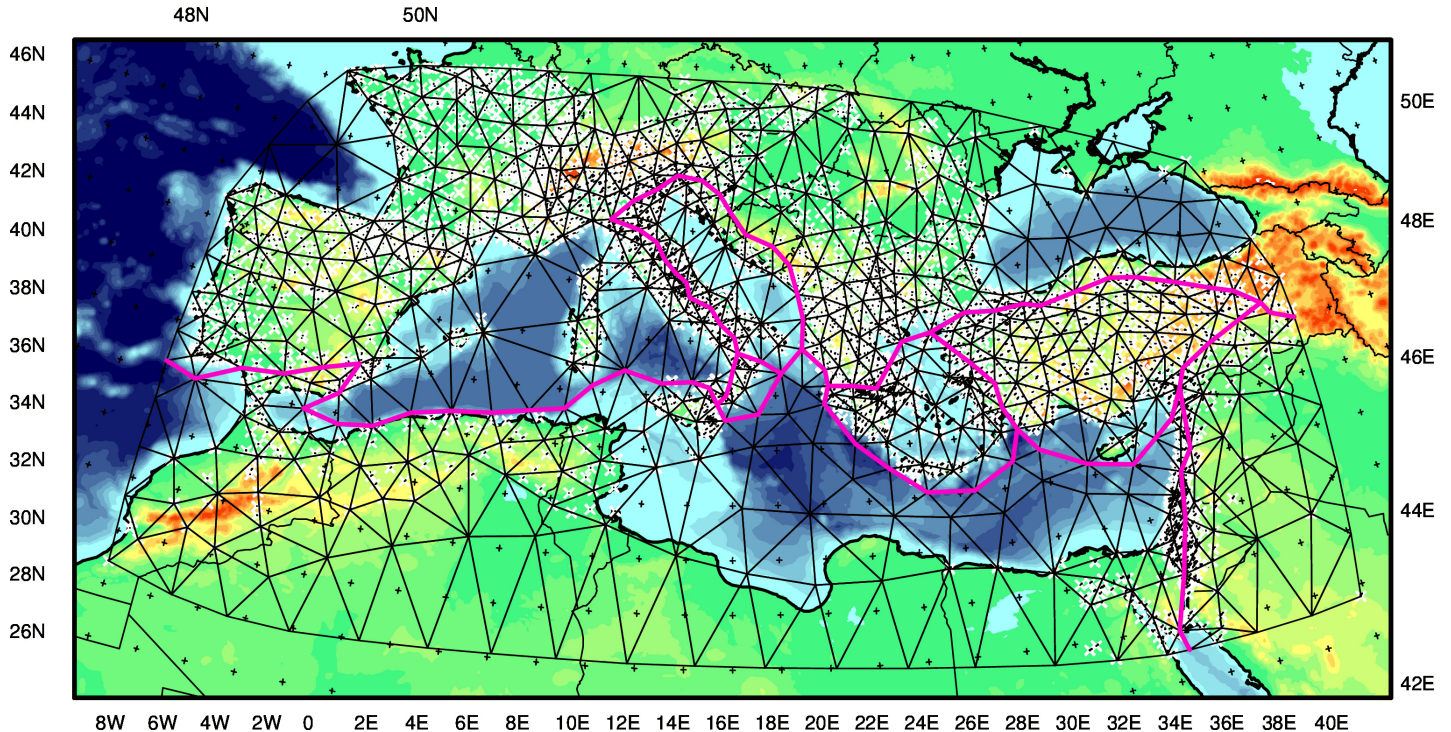


Figure 5: Convex Delaunay triangulation network that parametrizes our Mediterranean models. The model parametrization has been adjusted to the locations (white crosses) of the 8969 GPS observations, local data density, regions with no data, and plate boundary fault traces (pink lines), which define the seven Adriatic, Aegean, African, Anatolian, Arabian, Calabrian, and Eurasian plates, see Figure A.1 for geological features marking the faults. This leads to 1111 triangles spanned by 584 nodal points and 97 fault segments. Note the smaller triangles in Greece, Italy, and Israel, where the data density is high, and the larger ones in the unsampled model (boundary) portions of the African and Arabian inner plates, Bay of Biscay, Black Sea, Ionian Sea, and Mediterranean Ridge. Here, synthetic data vectors have been placed, see Figure 7.

4 Experiments

Tetra allows to separately solve for the velocity gradient tensor ($\nabla\mathbf{v}$), rotation rate field ($\omega_{\theta\phi}$), surface fault slip vectors (\mathbf{f}_k), or geodetic network Euler rotations (Ω_m), or any combination of them. We are interested in four alternative kinematic descriptions of crustal deformation, being

- pure rigid block motion along unlocked faults (\mathbf{f}_k -model 1);
- rigid block rotation accommodated by unlocked faults ($\omega_{\theta\phi}$, \mathbf{f}_k -model 2);
- diffuse crustal flow while faults are assumed to be locked ($\nabla\mathbf{v}$ -model 3);
- the two endmember scenarios (model 3 and 1) mixed ($\nabla\mathbf{v}$, \mathbf{f}_k -model 4)

where, in model 2 to 4, it may be appropriate to invert and correct GPS observations coming from different papers for uniform relative network rotations, leading to seven different types of inversion. We continue with setting up a framework for subsequent experiments with several of the kinematic inversion types.

4.1 Model Parametrization

The study region is parametrized with Delaunay triangulation using the software of Shewchuk [1996] (Figure 5). A convex model boundary is created to prevent great circle integration paths from intersecting the boundary, hence from becoming unusable for inversion. The model parametrization has been iteratively refined through many inversions to improve the data fit as long as the model resolution is unaffected.

However, although the Mediterranean dataset is locally sufficiently dense to model high resolution patterns of deformation, particularly in Greece, Italy, and Israel, we keep the triangulation relatively coarse with triangles covering areas of around 1° by 1° on average. This is done in view of our objective to approximate the regional deformation field.

We adapt the velocity gradient parametrization to the GPS data distribution, surface traces of plate boundary faults, and model (boundary) parts with null data, resulting in a total of 1111 triangles spanned by 584 node positions and 97 fault segments (Figure 5). In this nodal network, fault lines connect doubled velocity gradient nodes that are not placed at observation points, enabling discontinuity of the velocity gradient field across slipping faults. For each of the four models, the number of kinematic parameters to be calculated is

- model 1: $2 \times 98 \mathbf{f}_k$ -components;
- model 2: 691 $\omega_{\theta\phi}$ - and $2 \times 98 \mathbf{f}_k$ -components;
- model 3: $4 \times 584 \nabla \mathbf{v}$ -components;
- model 4: $4 \times 691 \nabla \mathbf{v}$ - and $2 \times 98 \mathbf{f}_k$ -components

where model 1, 2 and 4 contain double velocity gradient nodes, and the number of Kreemer network rotation Ω_m -components is 3×43 (Section 4.3.1).

As is visible in Figure 5 and A.1, incorporated plate boundary faults divide the model domain into seven regions, comprising the major lithospheric African, Arabian, and Eurasian plates, and the Adriatic, Aegean, Anatolian, and Calabrian microplates. In the Western Mediterranean, the locations of the Africa-Eurasia plate boundary are digitized from Argus et al. [2011] for the Algerian Basin, and from Spakman et al. [2018] for the Alboran Basin and Betics. We shift the Argus et al. [2011] plate boundary at the Tell Atlas offshore (northwards) towards the Algerian Basin in line with Bougrine et al. [2019].

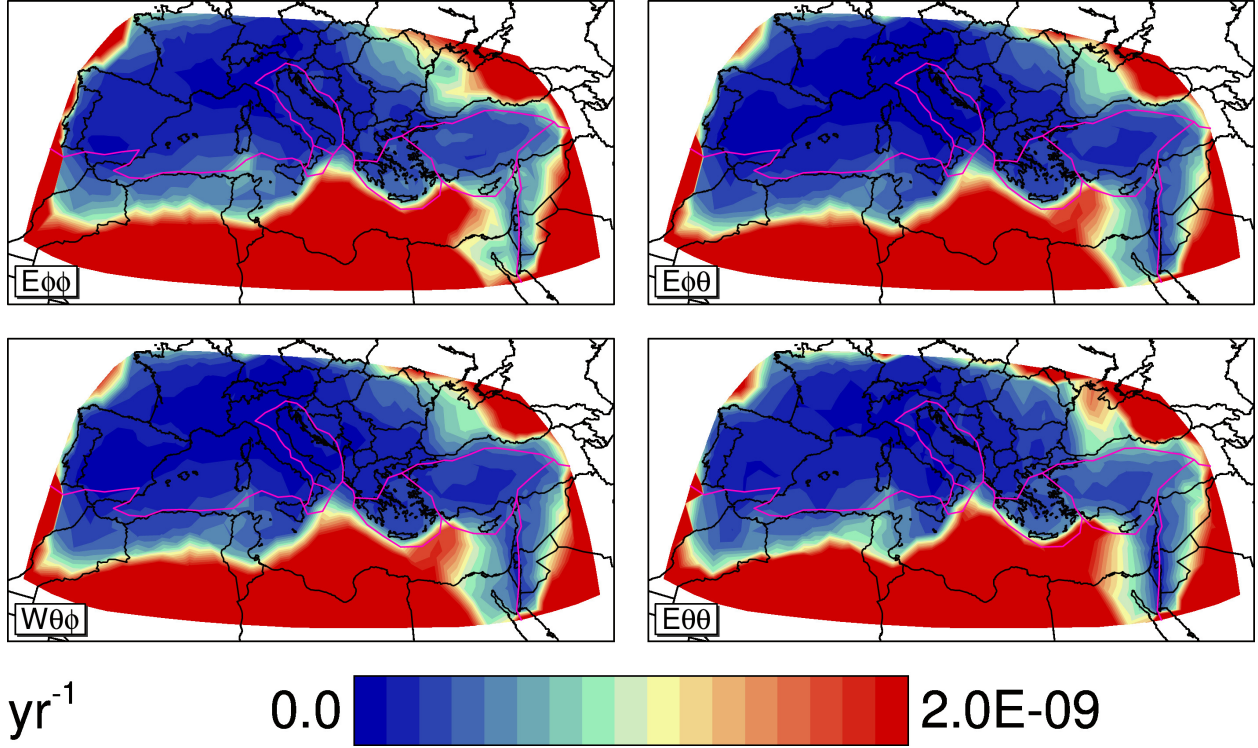
The Central Mediterranean Africa-Eurasia plate boundary coordinates are taken from Argus et al. [2011] and tuned to Nijholt et al. [2018] at the Aeolian Islands and in Sicily. To establish the Adriatic and Calabrian crustal blocks (Figure A.1), we base the fault locations in the Albanides, Alpine Arc, Apennines, Calabrian Peninsula, Dinarides, and Hellenides on the GPS velocity trends in the Adriatic, Calabrian, and Eurasian plate motion frames (Section 4.3.2), as well as on the tectonic settings outlined in Faccenna et al. [2014] (Figure 1), Nijholt et al. [2018], and van Unen et al. [2019]. The plate boundary traces of Argus et al. [2011] are adopted for the entire Eastern Mediterranean, except at Cephalonia Island, the Cyprian Arc, the Karasu Rift, and in the Rhodes Basin (Figure A.1), where they are adjusted to Faccenna et al. [2014].

In general, we approximate the digitized fault lines from Argus et al. [2011] and Spakman et al. [2018] with extended fault segments since the station density near these surface traces is often too low to construct a more detailed triangulation here, and because our focus is on modelling regional deformation patterns. The elongated fault lines are adapted to the GPS motion trends in fault-adjacent sampled areas.

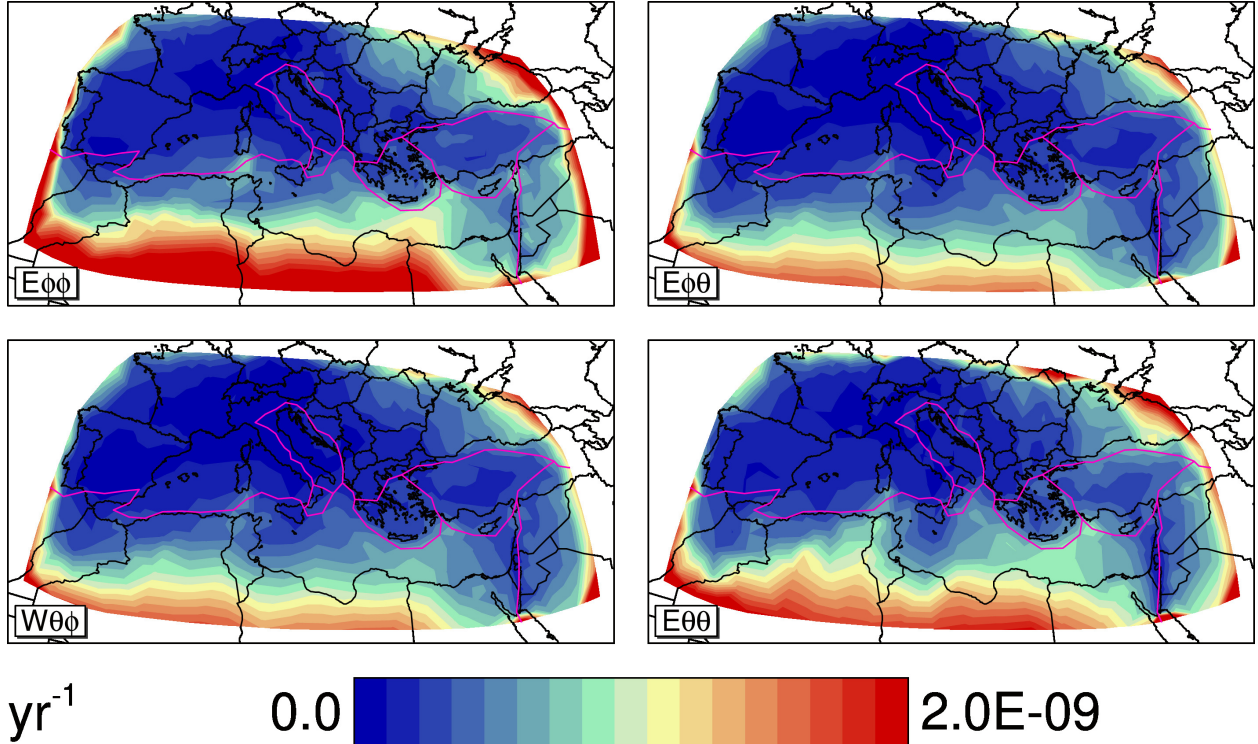
Considering unsampled regions (Figure 5, A.1), we parametrize the African and Arabian inner plates, Bay of Biscay, Black Sea, Ionian Sea, and Mediterranean Ridge to condition the inverse problem here with a combination of synthetic data and damping (Section 4.2). The nearby station clusters, model boundary, and African plate boundary geometry guide our design of a coarse regular grid. For example, triangles in the Eastern Mediterranean Sea are roughly aligned with the Ionian Sea and Mediterranean Ridge according to Faccenna et al. [2014] (Figure 1).

4.2 Synthetic Data Constraints and Strain Rate Damping

Coupled tuning of the synthetic data input, amount of damping, and model parametrization in areas deficient of relative velocity observations is key to constraining the inverse problem here. In a first trial inversion, we invert the 8969 GPS motions for the velocity gradient tensor and network Euler rotations relative to the Kreemer dataset. Fault creep, which may introduce further complications (see Section 5 for discussion), is involved in a later experiment (Section 4.4). For now, we are dealing with the natural locked state of faults. Dartboard settings of $d_{min} = 0.1^\circ$, $d_{max} = 6^\circ$, $n_{max} = 2000$, and $i_{multiples} = 1$ are applied to connect



(a) GPS data-only model. Excessive amplitude errors are visible where relative velocity observations are lacking.



(b) GPS and synthetic data model. The synthetic Euler vectors suppress the unwarranted amplitude errors, but not completely.

Figure 6: Undamped velocity gradient standard deviations obtained from $\nabla \mathbf{v}$, Ω_m -inversion of (a) the 8969 original GPS observations, and (b) these data plus 212 synthetic plate motion observations put where spuriously high errors marked by contoured reddish colours, or values of $\geq \sim 2.0 \cdot 10^{-9} \text{ yr}^{-1}$ (i.e. 10% of the solution amplitudes or more), are present in absence of any sites, being along the model boundary and inside the African and Arabian plates, Atlantic Ocean, Bay of Biscay, Black Sea, Ionian Sea, and Mediterranean Ridge, see Figure A.1 for a map with these geological attributes. For reference, fault traces (in pink) are visualized. The displayed strain ($\epsilon_{\phi\phi}$, $\epsilon_{\phi\theta}$, $\epsilon_{\theta\theta}$) and rotation rate ($\omega_{\theta\phi}$) components are ordered according to $\begin{bmatrix} \epsilon_{\phi\phi} & \epsilon_{\phi\theta} \\ \omega_{\theta\phi} & \epsilon_{\theta\theta} \end{bmatrix}$, see Eq. (2).

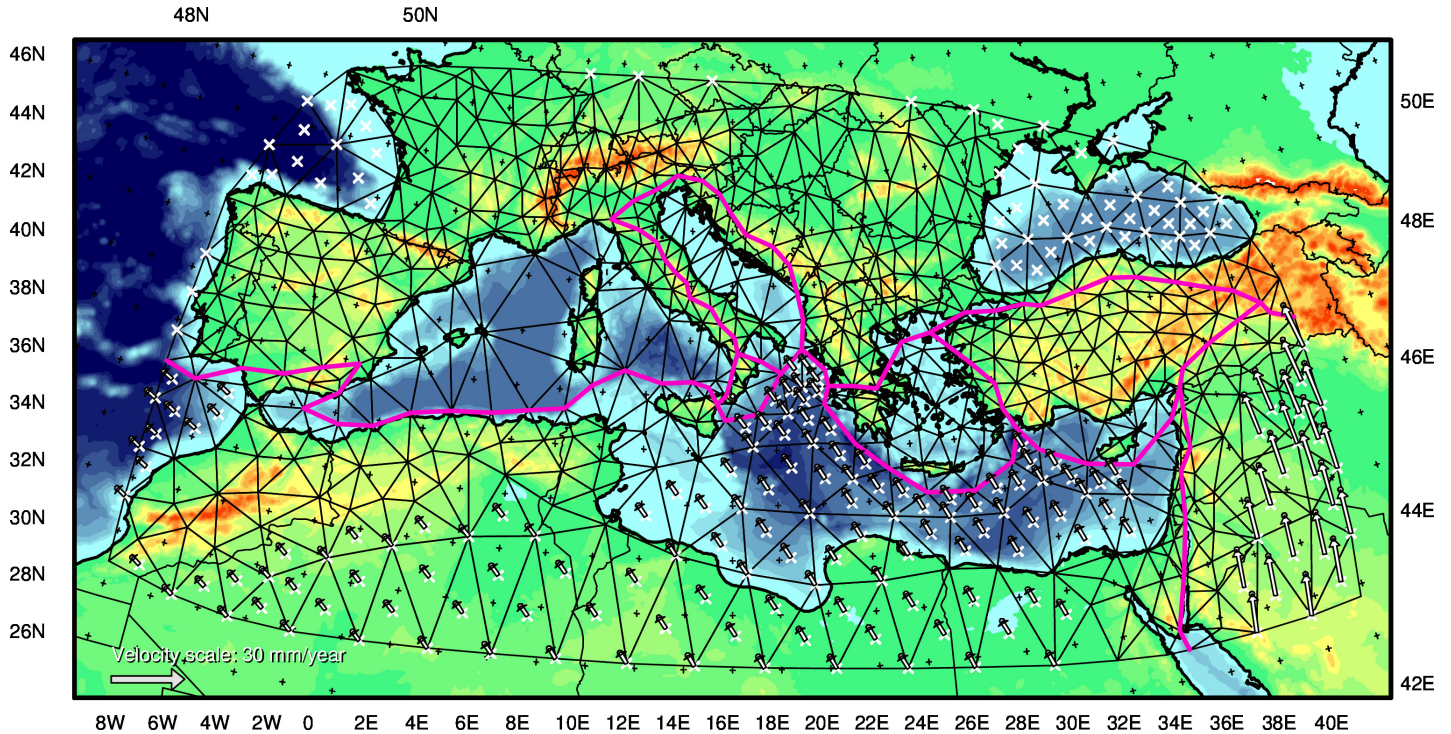


Figure 7: 212 synthetic Euler observations of rigid African, Arabian, and Eurasian (zero) plate velocity relative to the Kreemer Eurasia frame, together with their 95% confidence 1.0 mm/yr -error ellipses and locations (white crosses). For reference, the mesh and fault traces (in pink) are plotted. The synthetic motions mimic uniformly rotating stiff lithosphere at internal model nodes, boundary nodes, and triangle centers, away from geodetic stations to avoid that the synthetic velocities affect the real surface deformation field. Note that above synthetic dataset has become the preferred one out of several others, see Section 5.3 for discussion.

numerous data vectors and include site multiples (Figure 4), producing 11849467 observation equations (1) set up along geodesics, which are inverted together with 1158 node and 2222 triangle loop equations. The GPS data-only model ($\chi^2_\nu = 6.77$) has a perfect resolution ($\tilde{r}_m = 1.00$), hinting at an overdetermined inverse problem in which there are plenty (i.e. millions) of relative motion data to perfectly resolve thousands (2465) of model parameters. However, our solution displays excessive amplitude errors ($\geq \sim 2.0 \cdot 10^{-9} \text{ yr}^{-1}$) compared to the average velocity gradient amplitude ($\tilde{s}_m^v = 1.85 \cdot 10^{-8} \text{ yr}^{-1}$) in model parts where observations are absent (Figure 6a), being inside the African and Arabian plates, Atlantic Ocean, Bay of Biscay, Black Sea, Ionian Sea, and Mediterranean Ridge (Figure A.1), and along the model boundary where integration paths normally are relatively sparse.

To remedy above situation, we can either impose zero deformation by locally damping the amplitude extremes to zero, or use the best we know, which is the uniform Euler plate motion as an average of the true velocity field. We choose to exploit such extra information while requiring no internal deformation, i.e. zero strain rate, but still allowing for rigid block rotation. To this end, a Fortran program (*synth_data.f*) has been developed that enables easy definition of synthetic Euler plate velocities in triangles and close to fault zones. Synthetic vectors are created relative to Eurasia by adding African and Arabian Euler motions to points of initially zero velocity (Figure 7). Eurasian motions are fixed at zero.

We may derive the necessary Africa-Eurasia and Arabia-Eurasia Euler poles from any of the Pacific, IGS08-, or NNR-frames in which Kreemer et al. [2014] published poles. The relative Euler pole computation is done by, taking IGS08 as an example, subtracting the global Cartesian Eurasia-IGS08 pole coordinates and angular pole velocity from those of the Africa- and Arabia-IGS08 poles. We find a very small difference in Africa-Eurasia and Arabia-Eurasia poles between the three reference frames, so the choice of the original Kreemer frame is arbitrary. We pick the IGS08-frame. According to the syntax of longitude ($^\circ$), latitude ($^\circ$),

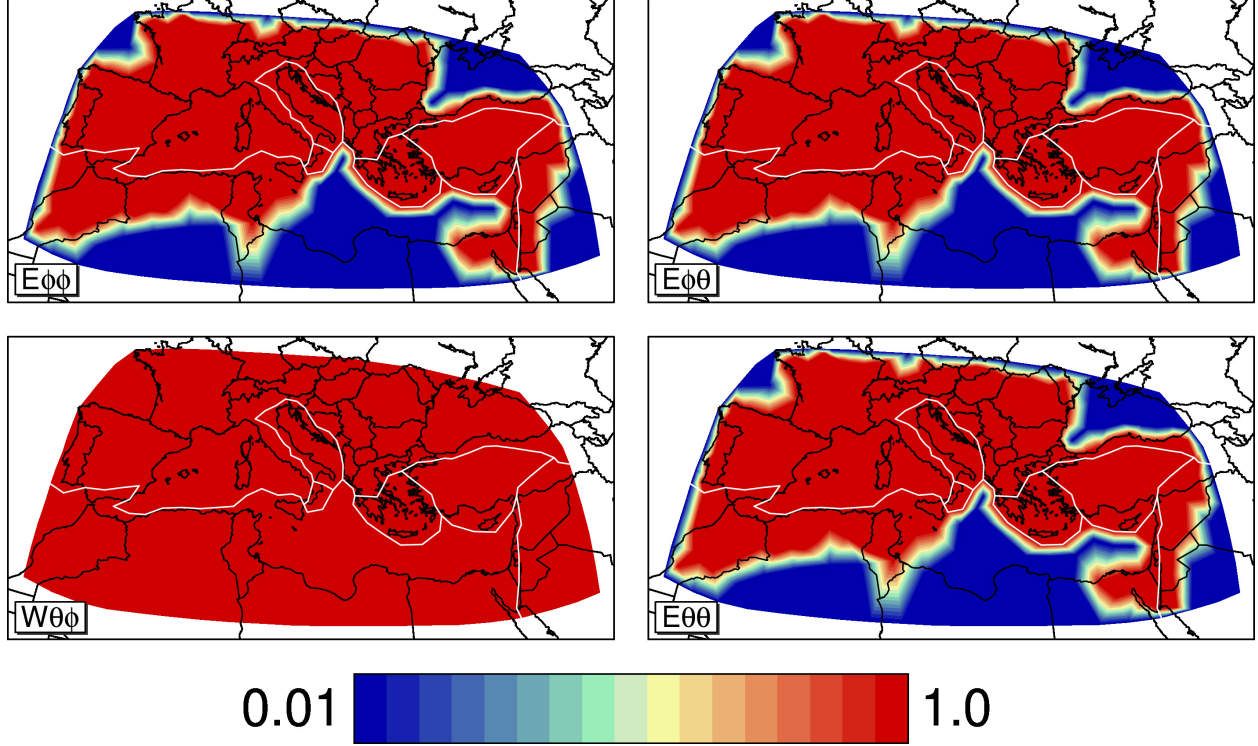


Figure 8: Damping of the strain rate diagonal elements from the model resolution matrix (7) associated with $\nabla \mathbf{v}$, Ω_m -inversion of the 8969 original GPS and 212 synthetic observations. For reference, fault traces (in white) are visualized. The displayed strain ($\epsilon_{\phi\phi}$, $\epsilon_{\phi\theta}$, $\epsilon_{\theta\theta}$) and rotation rate ($\omega_{\theta\phi}$)-components are ordered according to $\begin{bmatrix} \epsilon_{\phi\phi} & \epsilon_{\phi\theta} \\ \omega_{\theta\phi} & \epsilon_{\theta\theta} \end{bmatrix}$, see Eq. (2). While the strain rate resolution has been damped to zero, see the deep blue contoured colours, along the entire model boundary and at all internal nodes where synthetic Euler vectors have been inserted (Figure 7), the rotation rate resolution stays perfect (i.e. deep red). Note that the continuous deformation-only and -fault creep solutions (model 3-4) of the GPS motion inversion experiments are characterized by approximately the same resolution diagonal elements as shown here (Section 4.4.2.1).

and angular velocity ($^{\circ}/Myr$), the two IGS08-based poles are

- -27.736 -4.805 0.0598 (*Africa-Eurasia pole*);
- 9.488 26.838 0.3411 (*Arabia-Eurasia pole*)

which yield synthetic motions that are consistent with the overall GPS velocity trends within the African and Arabian plates (Figure 9a). Last of all, we assign an east and north standard deviation of 1.0 mm/yr and data correlation of zero to the synthetic observations (Figure 7), where the former represents the average GPS data error.

After experimenting with various spatial distributions of synthetic data (Section 5.3), 212 synthetic Euler vectors are placed away from GPS station positions at node locations and triangle centers to incorporate rigid rotation of the African, Arabian, and Eurasian plates (Figure 7), simultaneously preserving patterns of the actual crustal deformation revealed by geodetic observations. Synthetic data have also been put at model boundary nodes as a boundary condition on the deformation field. Inversion of the 9181 GPS and synthetic velocities, i.e. 12152657 equations (1) belonging to geodesics plus the 3380 closed loop equations, shows that the synthetic observations slightly lower the data fit ($\chi^2_{\nu} = 6.82$) in exchange for a partially successful elimination of the unwarranted amplitudes (Figure 6b). To exclude intraplate deformation along the entire model boundary and at all internal nodes with synthetic motions, we damp the strain rate field to zero here using a scaling coefficient of $\alpha_0 = 2 \times 10^{11}$ (Figure 13b-c, 17). A decrease in data fit ($\chi^2_{\nu} = 6.90$) and resolution ($\tilde{r}_m = 0.886$) is observed as a consequence of the damping, which zeroes the strain rate diagonal elements of the model resolution matrix (Figure 8).

4.3 Network Euler Rotations

With all previous tuning of the forward and inverse problems, we are ready for several experiments, starting with the estimation of relative network Euler rotations.

4.3.1 Correction for Relative Network Rotations and Site Multiples

Homogeneous rotational differences between our 45 subdatasets may exist as a result of the possible different coupling of each network to a global geodetic reference frame. This is a technical issue in the form of a uniform Euler rotation of GPS network data with respect to a chosen reference dataset. Relative network rotations cause unwanted data scatter, thus need to be removed. We rotate the 44 non-reference networks into the Kreemer dataset with network Euler poles estimated by inverting the 9181 GPS and synthetic observations for the velocity gradient field and network rotations (Table 2). The mixed parameter inversion is performed to make sure that real surface deformation is not being mapped into the Euler poles. We use the same dartboard ($d_{min} = 0.1^\circ$, $d_{max} = 6^\circ$, $n_{max} = 2000$, $i_{multiples} = 1$) and strain rate damping ($\alpha_0 = 2 \times 10^{11}$) as before.

Given multiple geodetic datasets, the correction for relative network rotations is an iterative process of various inversions in which datasets are progressively rotated (with stepwise smaller rotations) into and attached to the reference network when their Euler poles become statistically insignificant (Table 2), as measured in Tetra using the inverse ratio σ/ω between the angular velocity ω and its standard deviation σ converging to e.g. ≥ 0.8 . By merging corrected networks with the reference dataset, still to be included networks may better overlap with the expanding reference dataset in an increasing number of common points, resulting in a higher potential of Euler pole convergence for the yet independent networks in a next inversion. Besides the σ/ω -ratio, dataset characteristics (e.g. the data error) and the pole location relative to the associated network may also be inspected in the interpretation of Euler pole significance. Because we avoid to inspect thousands of GPS data individually, this analysis is kept fairly basic.

Four inversions are eventually carried out, in which most of the 44 network Euler poles could be iteratively determined from the stagewise incorporation of successfully rotated datasets into the Kreemer network (Table 2). Especially important in the procedure are datasets containing a relatively large amount of observations ($\geq \sim 150$) that are widespread and share many sites with the Kreemer network and local datasets. Assuming such regional networks to be helpful in fitting the rotation of smaller datasets, we define ten of them [Metois et al., 2015; Palano et al., 2015; Nguyen et al., 2016; Pietrantonio et al., 2016; Serpelloni et al., 2016; Sánchez et al., 2018; Özdemir and Karshoğlu, 2019; Civiero et al., 2020; D’Agostino et al., 2020; Gomez et al., 2020] (Figure A.7). Extending the Kreemer dataset with these networks in the first two inversions appears to be beneficial since almost all of the remaining Euler poles converge in the subsequent inversion (Table 2).

Prior to inversion, the Bahrouni et al. [2020] dataset is directly added to the Kreemer network because otherwise the inversion fails owing to an absence of common network positions. Other remarkable datasets have an unclear pole convergence trend, being the Barreca et al. [2014b], Marinou et al. [2015], Walpersdorf et al. [2015], Nguyen et al. [2016], Sánchez et al. [2018], and Walpersdorf et al. [2018] networks (Table 2). In particular, the sharp increase in angular velocity for Marinou et al. [2015] and Walpersdorf et al. [2015] between inversions suggests an unreliable trend, and for Sánchez et al. [2018] the pole velocity relative to this network falls within the data error, implying an insignificant pole. Possible reasons underlying an ill-defined convergence trend may be little to no overlap with the (expanded) Kreemer dataset for Walpersdorf et al. [2015] and Marinou et al. [2015], respectively, and very small data errors, e.g. in the case of Sánchez et al. [2018], see Section 5.1 for further discussion. We adopt the Euler poles from the first inversion for rotating the six networks with an unclear trend one time before attaching them to the Kreemer dataset (Table 2).

Through the inversions, the data fit χ^2_ν (9) progressively improves from 6.90 to 5.91, but reduces to 6.01 in the last inversion due to all poles having converged (Table 2), which means that relative network rotations cannot explain the data anymore. Once each non-reference dataset is corrected for Euler rotations, we invert for the velocity gradient field only and observe the same converged fit of $\chi^2_\nu = 5.91$, confirming that all rotations relative to the Kreemer network have been approximately removed. Lastly, the dataset size is shrunk by averaging site multiples into single vectors, leading to the final dataset consisting of 4118

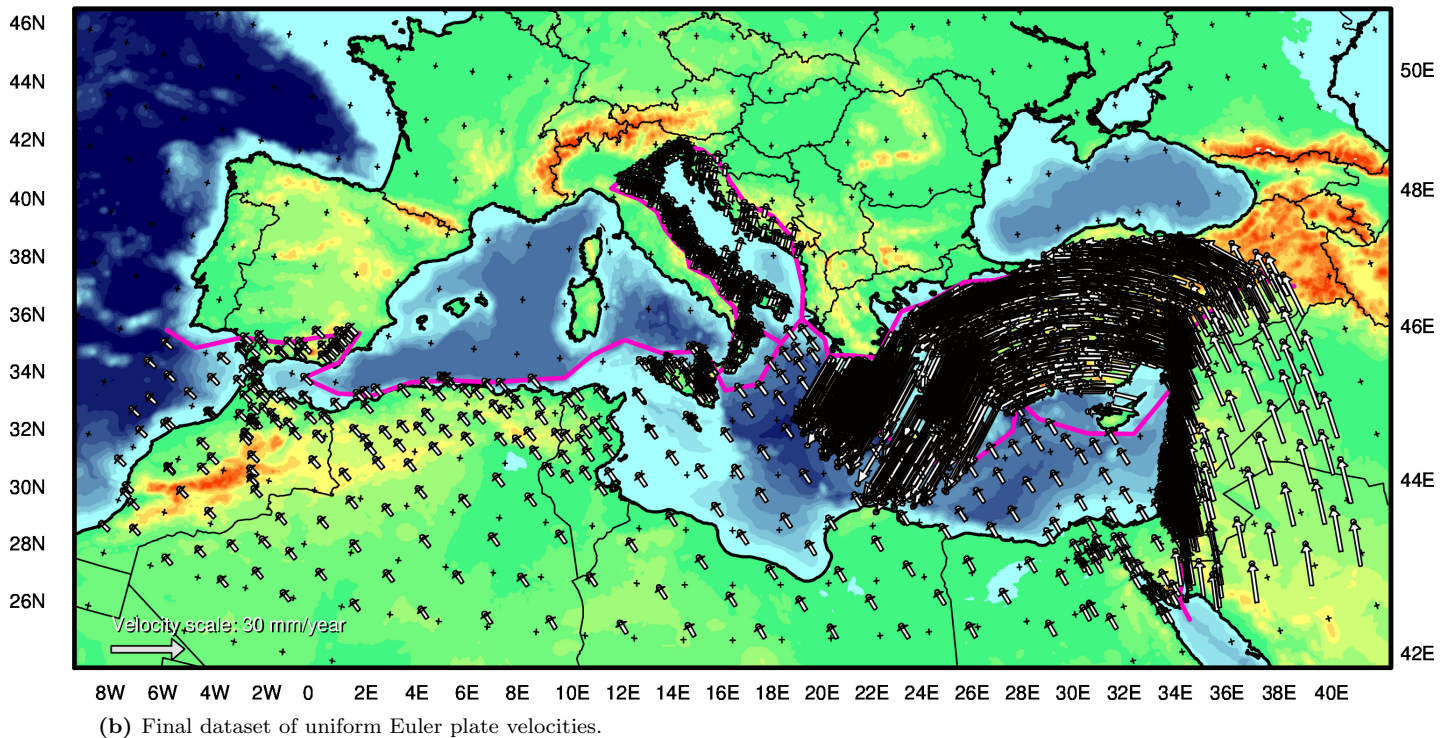
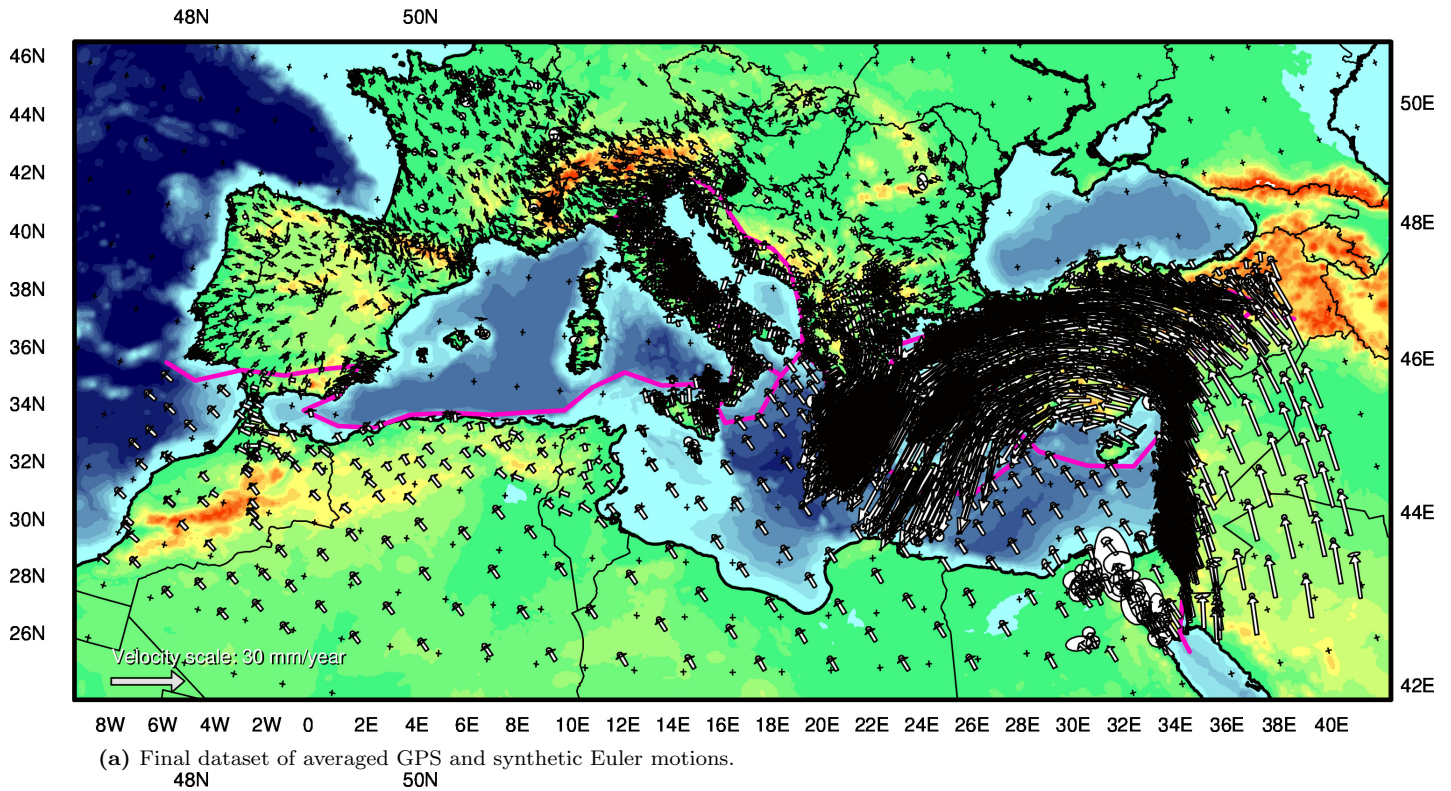
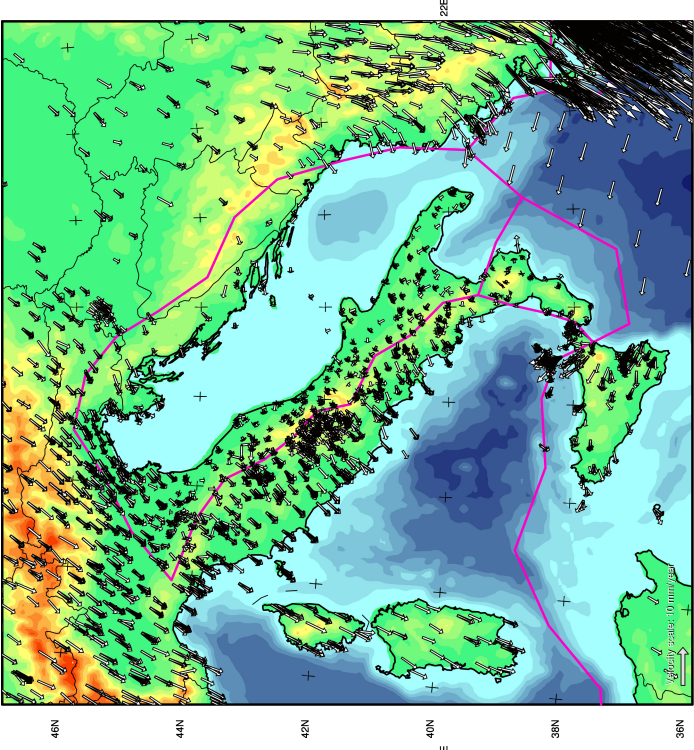
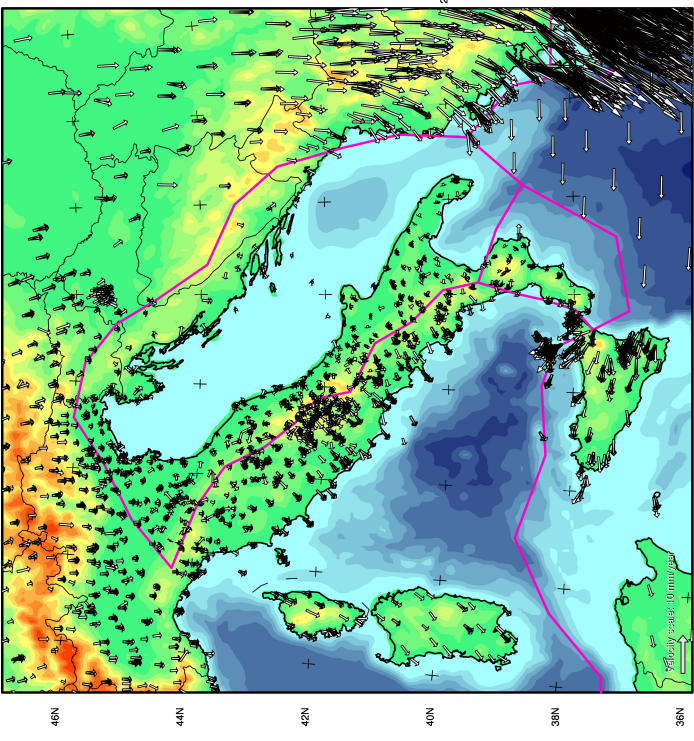


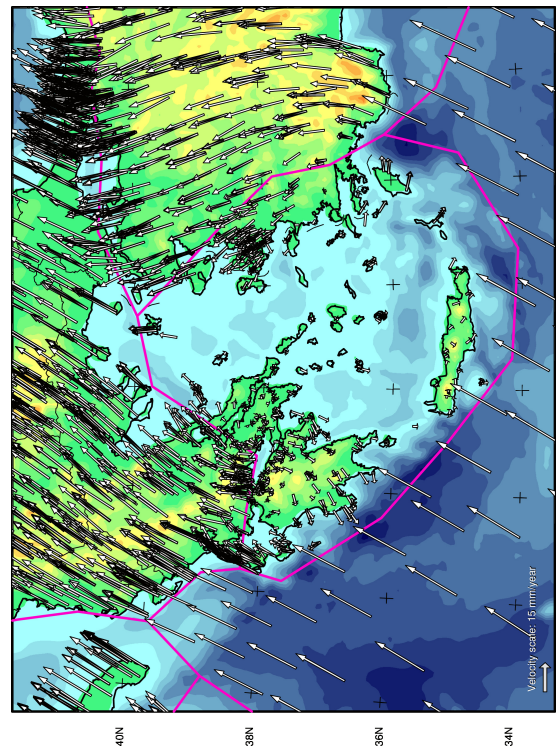
Figure 9: Final GPS and Euler datasets relative to Eurasia obtained by thorough experimentation, both comprising the 212 synthetic Euler velocities and, respectively, (a) the 4118 GPS vectors corrected for site multiples after the original 8969 observations had been corrected for network rotations into the Kreemer Eurasia dataset, and (b) the same 4118 averaged motions replaced with the Euler pole velocity of the African, Adriatic, Aegean, Anatolian, Arabian, or Calabrian plate where each of the GPS stations is located (with zero velocity for Eurasia). For reference, fault traces (in pink) are visualized. The data vectors are plotted together with their 95% confidence error ellipses, which are associated with an 1.0 mm/yr east and north standard deviation for the synthetic and substituted Euler data.



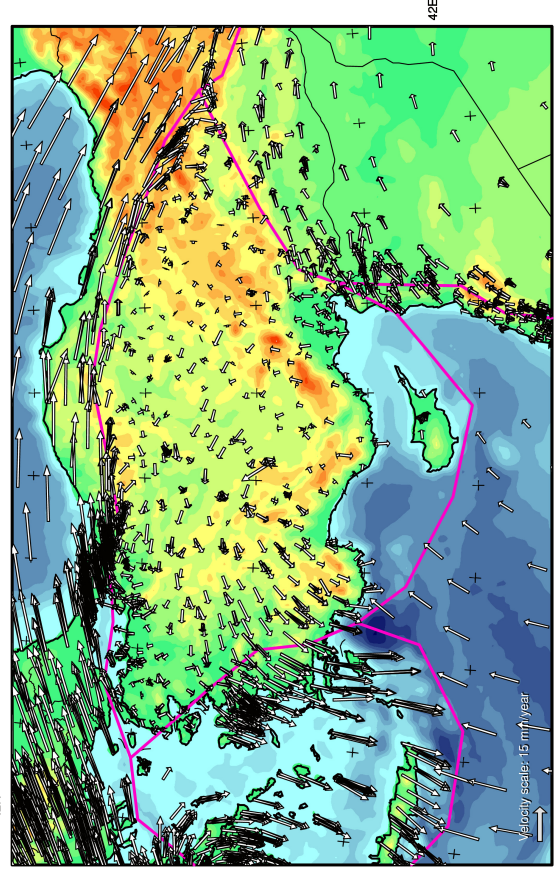
(a) Motions relative to Adria. Note the small vectors in Calabria.



(b) Motions relative to Calabria. Note the small vectors in Adria.



(c) Motions relative to the Aegean Region. Note the velocity outliers here.



(d) Motions relative to Anatolia. Note the velocity outliers here.

Figure 10: Synthetic and corrected geodesic motions, together with their 95% confidence error ellipses, rotated into the Euler pole velocity frames of the (a) Adriatic, (b) Calabrian, (c) Aegean, and (d) Anatolian microplates containing the respective 1024, 120, 567, and 817 non-averaged GPS observations from which the poles have been estimated. For reference, fault traces (in pink) are plotted. Within each platelet, the subtracted average tectonic rotation is roughly equivalent to many (thus near-zero) GPS motions, especially in Adria and Calabria. However, several data clusters clearly deviate from the Aegean and Anatolian velocity frames, see (c) the Aegean vectors at the islands of Cephalonia, Lemnos, and the Dodecanese, and in the Izmir Province and Peloponnese Peninsula, and (d) the Anatolian vectors along the North Anatolian Fault and in the Western Anatolian Extension Zone and Nur Mountains (Figure A.1). These velocity frame outliers signal intraplate deformation, see Section 5.1 for discussion. Note that there is little relative motion between Adria and Calabria.

GPS and 212 synthetic motions with respect to Eurasia (Figure 9a).

4.3.2 Microplate Euler Poles

Now that the geodetic data are corrected for relative network rotations, we can try to estimate the average tectonic rotations described by observations located within model parts enclosed by plate boundary faults. First, a user-friendly Fortran program (*contour_data.f*) has been written to select such data points. Using a separate program (*euler_pole.f*) of the Tetra suite, we determine Euler poles relative to Eurasia of the established Adriatic, Aegean, Anatolian, and Calabrian blocks from 1024, 567, 817, and 120 sampled GPS observations, respectively. To include as much (original) data as possible into the pole computation, site multiples have not yet been averaged, and no observations inside the microblocks have been omitted from the four subdatasets. We calculate Euler poles with longitude-latitude coordinates ($^{\circ}$), angular velocities ω ($^{\circ}/Myr$), variances σ ($^{\circ}/Myr$), and σ/ω -ratios (%) of

- -5.585 44.820 0.1399 0.0010, 0.7% (*Adria-Eurasia pole*);
- -16.292 48.353 -0.5003 0.0022, 0.4% (*Aegean Region-Eurasia pole*);
- 31.753 30.592 1.1193 0.0016, 0.1% (*Anatolia-Eurasia pole*);
- 38.770 27.921 -0.0987 0.0169, 17% (*Calabria-Eurasia pole*)

which are well-resolved apart from the more statistically uncertain Calabria pole. This significant error may be largely related to a lack of observations (120) and small plate surface area contributing to pole estimation.

We note the sharp contrast between our Aegean Region pole and the Kreemer Aegean Sea-Eurasia pole (-108.318 6.351 -0.3186), i.e. the Eurasia-IGS08 pole reported by Kreemer et al. [2014] subtracted from their Aegean Sea-IGS08 pole. Nonetheless, the Euler motions that correspond to the Aegean Region and Sea poles are comparable, see Figure 9b for an overprint of the Aegean GPS data with the Aegean Region-Eurasia pole velocity. In the dataset from Figure 9b, each of the 4118 (averaged) station vectors has been replaced with the Euler pole motion of the African, Adriatic, Aegean, Anatolian, Arabian, or Calabrian plate containing the observations (with zero velocity for Eurasia), see Section 4.4 for elaboration and inversion experiments. Euler plate velocities relative to Eurasia have also been calculated at fault nodes, see Figure A.8.

As another visual check, we inspect the motion frames of our microblock Euler poles by subtracting the pole velocities from all 212 synthetic and 8969 corrected GPS motions (Figure 10). Inside the plates, most vectors become (very) small relative to the data outside the block, demonstrating that the GPS velocities generally show a homogeneous Euler rotation within the closed plate boundary contours. The remaining scatter in the data hints at (strong) local internal deformation of the platelets, see the Aegean motion frame outliers at the islands of Cephalonia, Lemnos, and the Dodecanese, and in the Izmir Province and Peloponnese Peninsula (Figure 10c), and the outlying Anatolian motions along the North Anatolian Fault and in the Western Anatolian Extension Zone and Nur Mountains (Figure 10d), see Figure A.1 for a map of the Mediterranean with these geological/geographical attributes.

4.4 GPS and Euler Motion Inversions

We are left with two final GPS and Euler velocity datasets in the Kreemer Eurasia frame (Figure 9), which are inverted for different purposes. Since the geodetic data may represent both continuous deformation and rigid block motion, we evaluate which kinematic description (model 1-4) fits them the best in a GPS (and synthetic) velocity inversion. Meanwhile, because our Euler pole motion data purely reflect the uniform rotation of stiff plates, we may gain insights into intraplate deformation from the differences between the GPS and Euler velocity inversions. Furthermore, the Euler data inversion may offer a baseline model for testing the Tetra software in the form of a simplified solution of the deformation field. Below, we address some technical complications and, next, perform GPS and Euler inversion experiments.

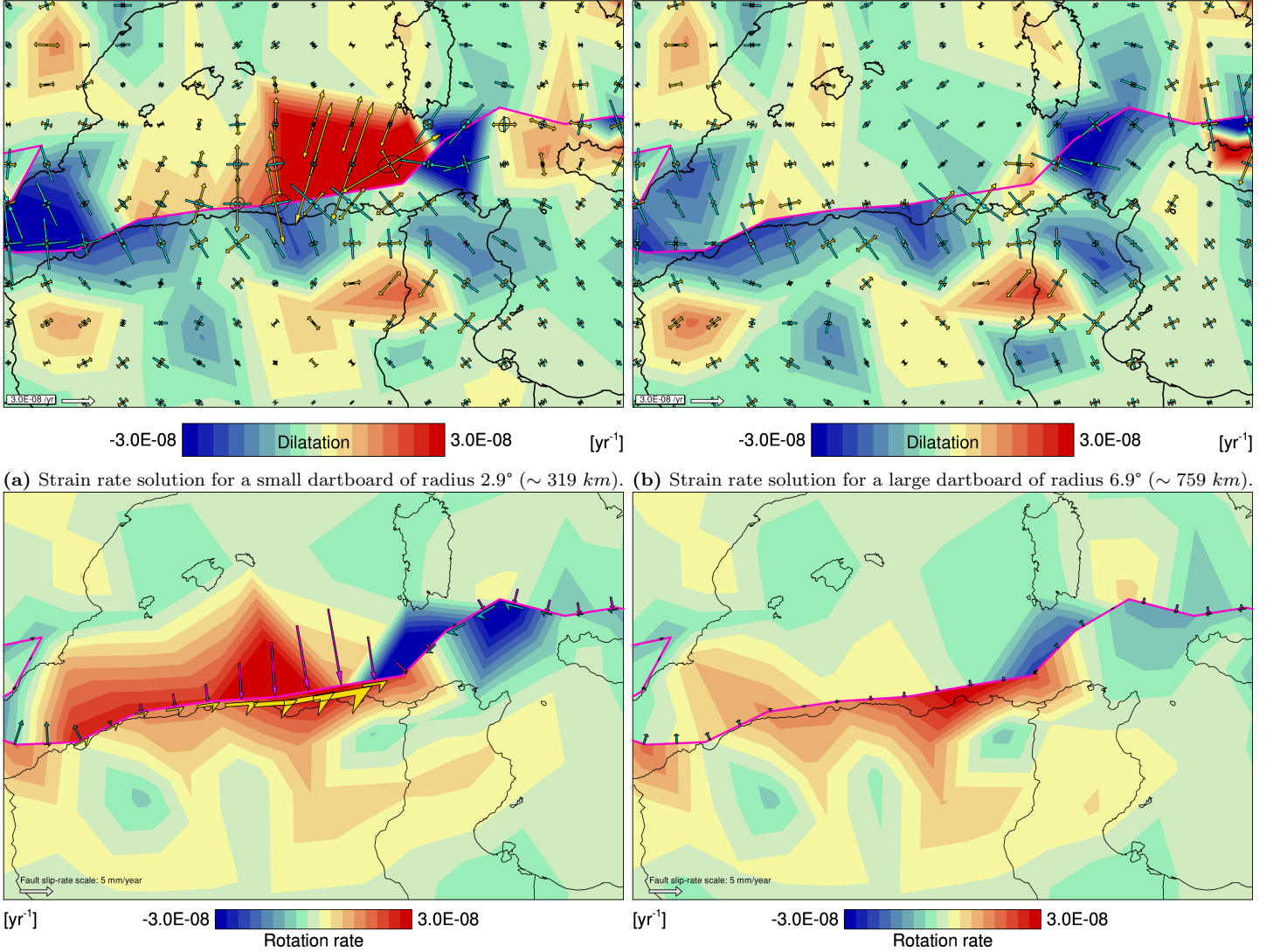


Figure 11: Surface kinematics around Algeria estimated from damped $\nabla \mathbf{v}$, \mathbf{f}_k -inversion of the 4330 averaged GPS and synthetic observations using (a, c) a small ($d_{min} = 0.1^\circ$, $d_{max} = 3^\circ$, $n_{max} = 200$, $i_{multiples} = 0$) and (b, d) large site connection dartboard ($d_{min} = 0.1^\circ$, $d_{max} = 7^\circ$, $n_{max} = 1000$, $i_{multiples} = 0$).

For reference, the Africa-Eurasia plate boundary fault (in pink) is visualized. Subfigures (a-b) show the principal axes and amplitudes of strain rate, with blue vectors and contoured bluish colours (or negative values) denoting contraction, and yellow vectors and reddish colours (positive values) indicating extension. Subfigures (c-d) display fault slip vectors and rotation rate amplitudes, where the vector colours are associated with types of fault motion (yellow: sinistral; lighter blue: dextral; darker blue: normal faulting; pink: reverse faulting), and the contoured bluish and reddish colours correspond to counterclockwise and clockwise rotation, respectively. Note that a rotation rate of $3.0 \cdot 10^{-8} \text{ yr}^{-1}$ is analogous to $1.7^\circ/\text{Myr}$. In the Algerian Basin, if too few fault-intersecting integration paths are made, a clear trade-off between fault creep and the velocity gradient tensor occurs, as revealed by the large fault slip rates and strongly discontinuous strain and rotation rate fields across the fault, see (c) and (a). One way to lower the trade-off is to employ a regional dartboard, due to which locked fault behaviour is approximated and the velocity gradient discontinuities are restricted in the Algerian Basin, see (d) and (b). Alternative ways are discussed in Section 5.1.

Model	χ_ν^2		$\nabla\mathbf{v}$ (10^{-8} yr^{-1})				\mathbf{f}_k (mm yr^{-1})				\tilde{r}_m	
	GPS	Euler	GPS		Euler		GPS		Euler		GPS	Euler
			\tilde{s}_m^v	$\tilde{\sigma}_m^v$	\tilde{s}_m^v	$\tilde{\sigma}_m^v$	\tilde{s}_m^f	$\tilde{\sigma}_m^f$	\tilde{s}_m^f	$\tilde{\sigma}_m^f$		
1	55.2	9.58	-				5.63	0.0151	6.76	0.0259	1.00	1.00
2	23.8	3.57	1.16	0.0198	0.832	0.0312	4.95	0.0186	6.59	0.0312	1.00	1.00
3	4.30	3.51	1.23	0.0203	1.03	0.0105	-				0.879	0.3723
4	3.59	1.19	1.54	0.0324	1.11	0.0289	1.42	0.0379	3.74	0.0635	0.902	0.5016

Table 3: Results from inversion of the averaged GPS and homogeneous Euler plate velocity datasets (Figure 9) for increasingly complex kinematic descriptions of crustal deformation (model 1-4). Model 1: fault slip-only; model 2: rigid block rotations; model 3: continuous deformation-only; model 4: continuous deformation and fault creep; χ_ν^2 (9): model-normalized data misfit; $\nabla\mathbf{v}$: velocity gradient tensor field; \mathbf{f}_k : fault slip rate; \tilde{r}_m (12): average model resolution; \tilde{s}_m^v (10): average velocity gradient amplitude; $\tilde{\sigma}_m^v$ (11): average velocity gradient standard deviation; \tilde{s}_m^f (10): average fault slip amplitude; $\tilde{\sigma}_m^f$ (11): average fault slip standard deviation. Note the following: (1) the data fit χ_ν^2 improves with rising model complexity in both the GPS and Euler motion inversions; (2) the velocity gradient field is merely composed of its rotation rate ($\omega_{\theta\phi}$ -)component in the block fault solution (model 2); (3) the $\tilde{\sigma}_m/\tilde{s}_m$ -ratio ranges between 1.02% and 3.75%, with a mean of $\sim 2\%$, for the velocity gradient tensor, and between 0.27% and 2.67% for fault creep; (4) the rotation rate ($\tilde{s}_m^{\omega\theta\phi}$) and fault slip (\tilde{s}_m^f) amplitudes ($1.16 \cdot 10^{-8} \text{ yr}^{-1}$; 5.63, 4.95, 1.42 mm yr^{-1}) of the GPS models (1-2, 4) are respectively higher/lower than for the Euler solutions ($0.832 \cdot 10^{-8} \text{ yr}^{-1}$; 6.76, 6.59, 3.74 mm yr^{-1}); (5) the undamped resolution \tilde{r}_m of the fault creep-only and rigid block rotation models (1-2) is perfect; and (6) the resolution \tilde{r}_m of the distributed deformation-only and -fault slip Euler solutions (model 3-4) is very low (0.3723, 0.5016) due to the strain rate damping of the entire internal and boundary nodal network.

4.4.1 Experiment Set-up

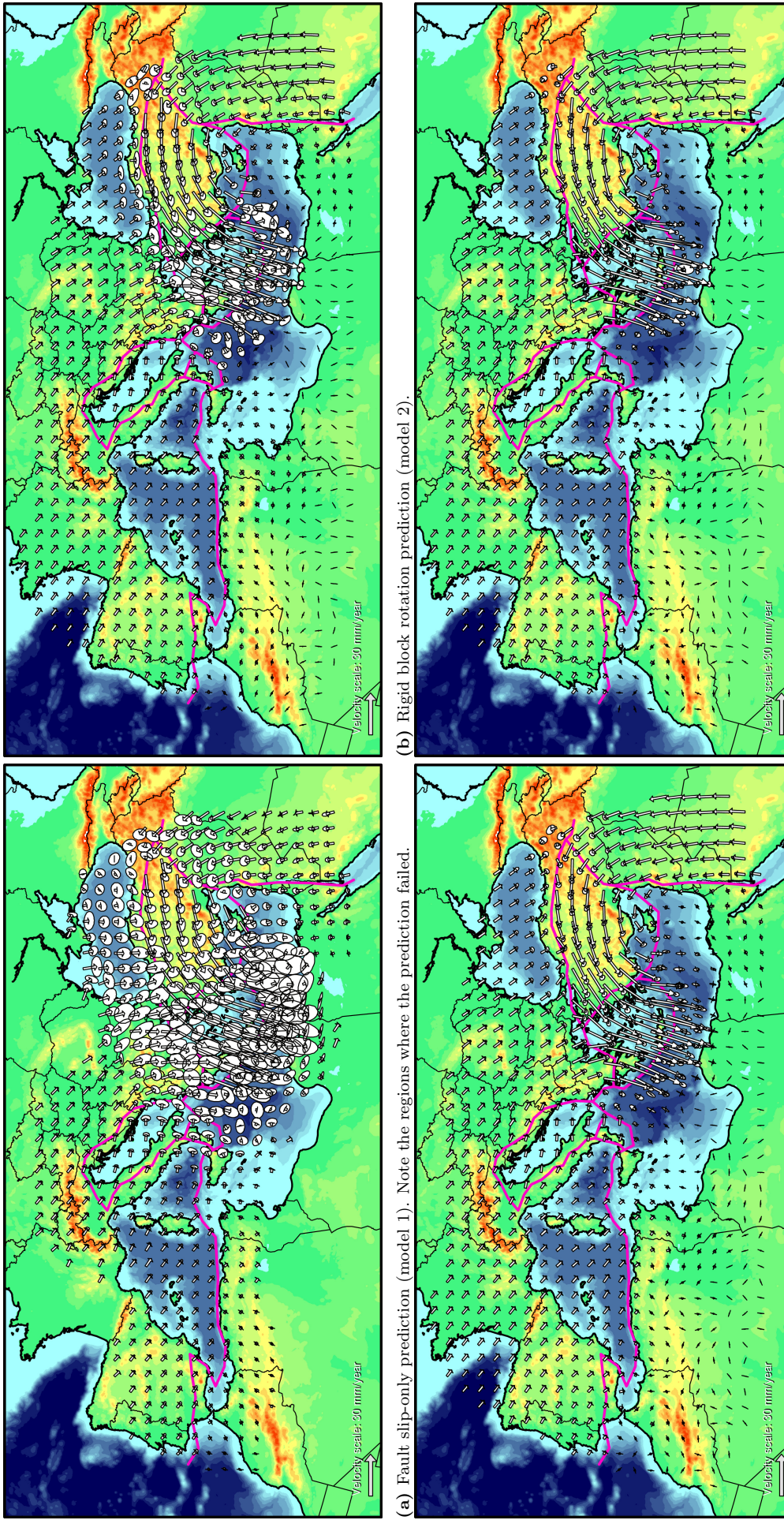
First of all, a large dartboard ($d_{min} = 0.1^\circ$, $d_{max} = 7^\circ$, $n_{max} = 1000$, $i_{multiples} = 0$) is applied to pair numerous single observations through geodesics, generating 2600125 equations (1) (plus the 3380 closed loop equations). This strategy is particularly valuable for the joint velocity gradient-fault slip inversion (model 4), which can produce locally strong trade-offs between the velocity gradient tensor and fault creep if a small dartboard of $\leq 3^\circ$ radius is used. Intense strain and rotation rate discontinuities across faults may characterize the trade-off, e.g. in the Algerian Basin (Figure 11). A large dartboard limits such artefacts by ensuring that the solution is constrained with enough data everywhere, especially in areas like the Algerian Basin where integration paths are relatively sparse.

On the other hand, it is usually better to adopt a small dartboard for the flow field prediction because model errors inside a large dartboard and faraway from the synthetic sites ($> 3^\circ$) may unnecessarily increase the prediction error. An exception is the fault slip-only model (1), for which employing a small dartboard has the disadvantage of failing to make a prediction at grid points positioned at a distance larger than the dartboard radius from faults, so no fault-intersecting paths can be created (Figure 12a). To compromise between issues of error propagation and remote prediction points, we choose fault slip-only (model 1) dartboard settings of $d_{min} = 0.1^\circ$, $d_{max} = 5^\circ$, $n_{max} = 300$, and $i_{multiples} = 0$ for the velocity prediction. In the normal situation (model 2-4), the flow field dartboard is given by $d_{min} = 0.1^\circ$, $d_{max} = 3^\circ$, $n_{max} = 200$, and $i_{multiples} = 0$.

Regarding the model regularization, we effectuate the same strain rate damping ($\alpha_0 = 2 \times 10^{11}$) as previously, assuring that the strain rate amplitudes at model boundary and synthetic data nodes are zeroed (model 3-4; Figure 17). In addition, doubled strain rate nodes at fault endpoints coinciding with the model boundary are also damped (model 4), and all strain rate nodes are damped to zero in the Euler models except for plate boundary nodes (model 3-4). By allowing for internal deformation along faults, we explore whether the Euler motions are translated into nearly zero strain rates at plate boundary nodes, as would be expected for data that solely express homogeneous block rotations. Note that the east and north variances of the Euler vectors are set to 1.0 mm/yr (Figure 9b), which is an indication of the average GPS (and synthetic) data error.

4.4.2 Inversion Results

In the following, we give an integrated description of the GPS and Euler data inversion experiments. For each dataset, inversion results from the four kinematic models (1-4) are presented (Table 3).



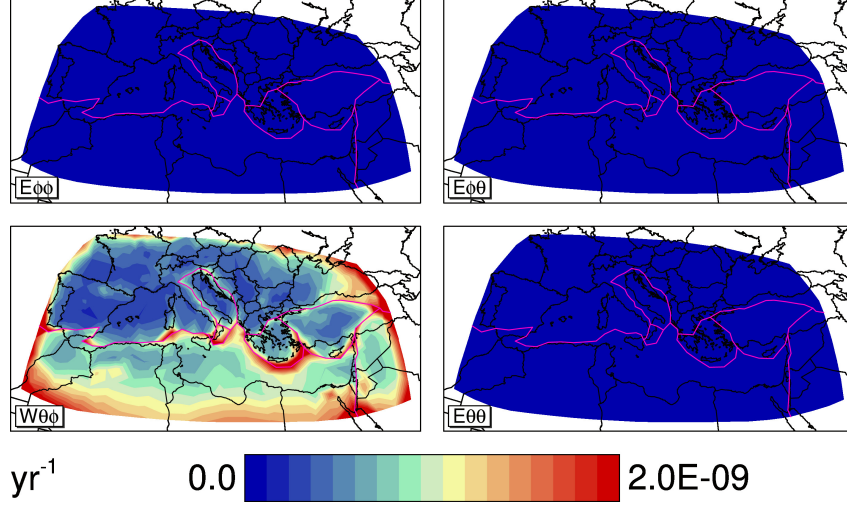
(a) Fault slip-only prediction (model 1). Note the regions where the prediction failed.

(b) Rigid block rotation prediction (model 2).

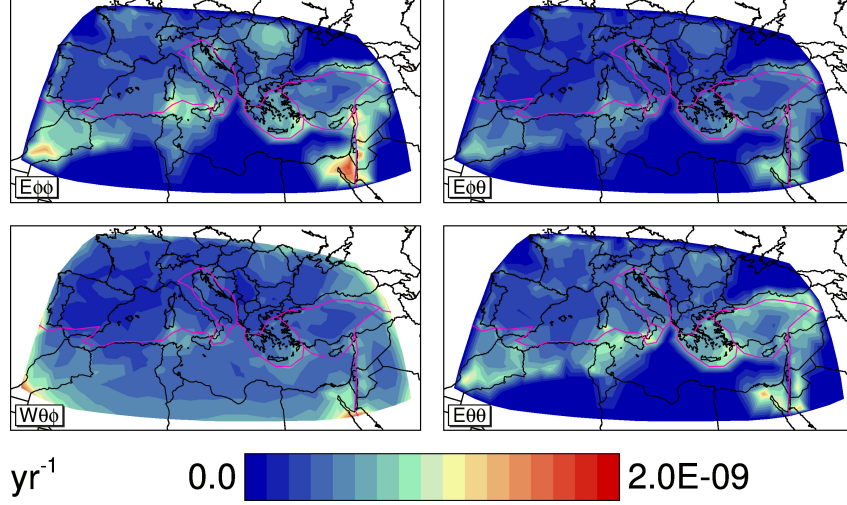
(c) Continuous deformation-only prediction (model 3).

(d) Continuous deformation-fault creep prediction (model 4).

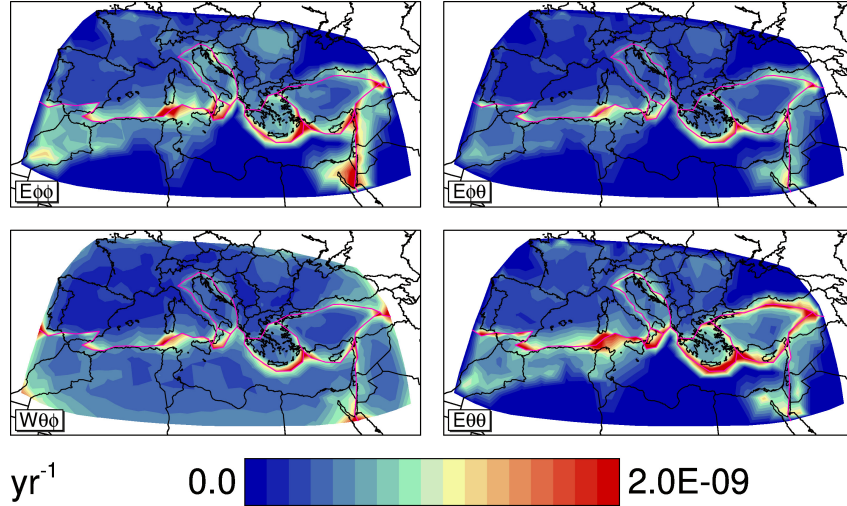
Figure 12: Crustal flow field predictions relative to the African plate derived from damped (a) \mathbf{f}_k^- , (b) $\omega_{\theta\phi}$, \mathbf{f}_k^- , (c) $\nabla\mathbf{v}$, \mathbf{f}_k^- , and (d) $\nabla\mathbf{v}$, \mathbf{f}_k^- -inversions (model 1-4) of the 4330 averaged GPS and synthetic observations. Whereas a local velocity prediction dashboard ($d_{min} = 0.1^\circ$, $d_{max} = 3^\circ$, $n_{max} = 200$, $i_{multiples} = 0$) has been adopted for the block fault (model 2; b) and diffuse flow solutions (model 3-4; c-d), a larger one ($d_{min} = 0.1^\circ$, $d_{max} = 5^\circ$, $n_{max} = 300$, $i_{multiples} = 0$) has been applied to the fault slip-only solution (model 1; a) in an effort to produce predictions faraway from faults (in pink) and, at the same time, keep prediction errors down. With rising model complexity (model 1-4), the 95% confidence error ellipses of the predicted vectors become progressively smaller, especially in the Eastern Mediterranean plate boundary zone. Moreover, from (a) to (d), the inversion fits the synthetic zero Africa velocities increasingly well.



(a) Rigid block rotation model (2). Note the very high amplitude errors.



(b) Continuous deformation-only model (3).



(c) Continuous deformation-fault slip model (4) Note the very high amplitude errors.

Figure 13: Velocity gradient standard deviations associated with damped (a) $\omega_{\theta\phi}$, \mathbf{f}_{k^-} , (b) $\nabla\mathbf{v}$ -, and (c) $\nabla\mathbf{v}$, \mathbf{f}_{k^-} -inversions (model 2-4) of the 4330 averaged GPS and synthetic observations. The displayed strain ($\epsilon_{\phi\phi}$, $\epsilon_{\phi\theta}$, $\epsilon_{\theta\theta}$) and rotation rate ($\omega_{\theta\phi}$ -) components are ordered according to $\begin{bmatrix} \epsilon_{\phi\phi} & \epsilon_{\phi\theta} \\ \omega_{\theta\phi} & \epsilon_{\theta\theta} \end{bmatrix}$, see Eq. (2). Unwarrantedly high amplitude errors, as marked by contoured reddish colours or values of $\geq \sim 2.0 \cdot 10^{-9} \text{ yr}^{-1}$ (i.e. 10% of the model amplitudes or more), prevail along faults (in pink) in the rigid block rotation and combined solutions (model 2, 4; a, c), and along the model boundary in the former model (2; a). Overall, the continuous deformation-only solution shows the lowest velocity gradient variances (model 3; b).

4.4.2.1 Model Quality Estimators

Damped inversion of the GPS dataset shows that the data fit χ_ν^2 (9) improves from 55.4 (model 1) to 23.8 (model 2), 4.30 (model 3), and 3.59 (model 4; Table 3) with growing model complexity. Similarly, the velocity field predictions of the respective four solutions display increasingly smaller error ellipses (Figure 12), in particular around the Eastern Mediterranean plate boundaries, and show vectors in the Ionian Sea and Mediterranean Ridge that become progressively closer to the synthetic data (i.e. zero velocity relative to Africa). These two trends suggest that rigid block motions alone describe the observations poorly (model 1-2), and that distributed deformation explains them relatively well (model 3-4).

Looking at the velocity gradient standard deviations (Figure 13), despite the acceptable $\tilde{\sigma}_m^v/\tilde{s}_m^v$ -ratios of about 2% (Table 3), excessive amplitude errors ($> 2.0 \cdot 10^{-9} \text{ yr}^{-1}$) relative to the overall amplitudes ($\sim 1.5 \cdot 10^{-8} \text{ yr}^{-1}$) are present along most of the model boundary in the rigid block rotation solution (model 2), and along extensive portions of the faults in this model and the continuous deformation-fault slip model (4). Lower standard deviations dominate the continuous deformation-only solution (model 3; Figure 13b). Taking into account the fault slip variances (Table 3), the near-zero $\tilde{\sigma}_m^f/\tilde{s}_m^f$ -values of the rigid block motion models (1-2) are slightly better than for the combined model (4; $\tilde{\sigma}_m^f/\tilde{s}_m^f = 2.7\%$). Nevertheless, we consider the former two solutions as poor in view of their data fit χ_ν^2 (55.4, 23.8), prediction error ellipses (Figure 12a-b), and velocity gradient standard deviations (Figure 13a).

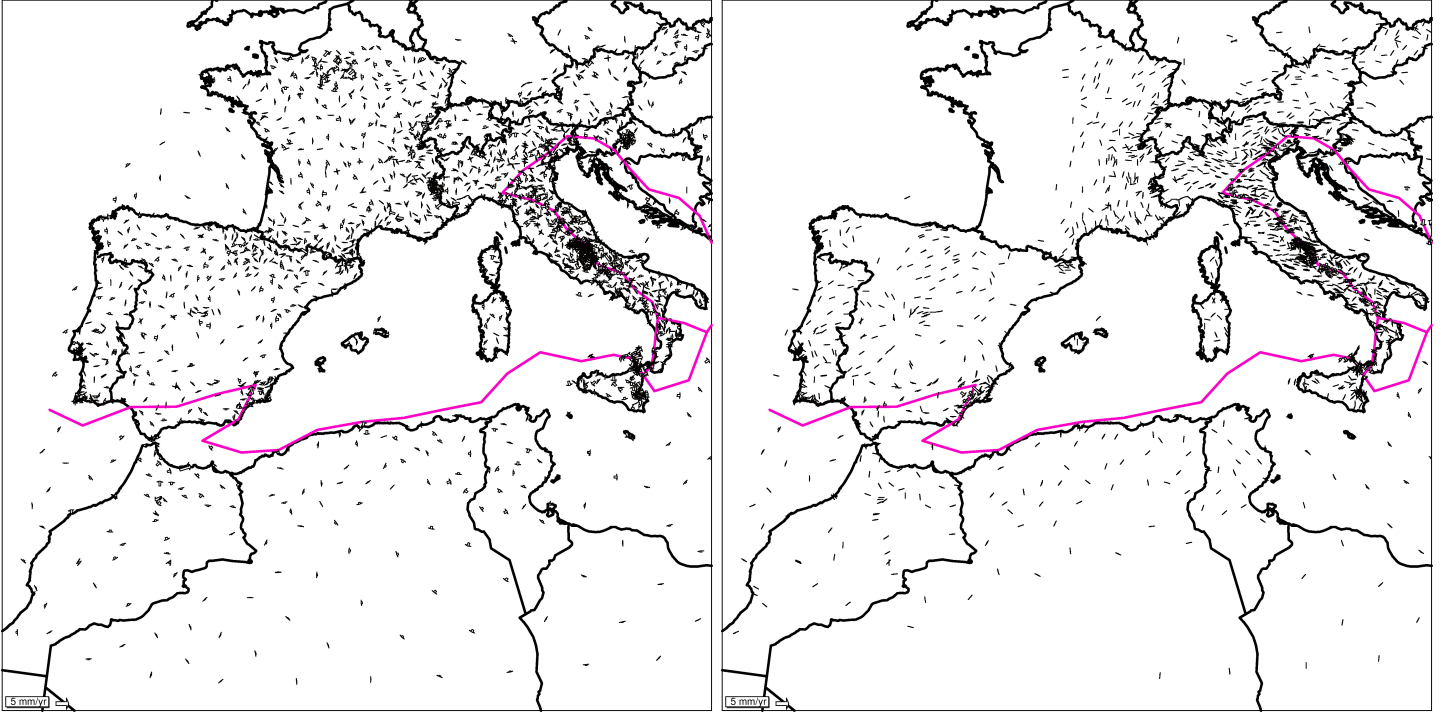
Our continuous deformation-only and -fault slip models (3-4) constitute acceptable solutions with a reasonable data fit χ_ν^2 (4.30, 3.59), flow field prediction (Figure 12c-d), and model resolution \tilde{r}_m (0.879, 0.902), where the former model has the best velocity gradient variances, and the latter has the best data fit, velocity prediction, and resolution. Note that the velocity gradient diagonal elements from the model resolution matrices of our two preferred solutions (model 3-4) are more or less equivalent to the ones displayed in Figure 8, and that the resolution is perfect ($\tilde{r}_m = 1.00$) if undamped (model 1-2; Table 3), as would also be the case for the velocity gradient-only and mixed velocity gradient-fault slip inversions (model 3-4).

Inversion of the Euler dataset likewise enhances the data fit χ_ν^2 from 9.58 to 3.57, 3.51, and 1.19 (model 1-4; Table 3). Interestingly, local rigid motion much better represents the Euler velocities than the real observations (model 1-2), and diffuse surface flow fits the Euler data surprisingly well (model 3-4). The GPS and Euler data misfit vectors from the continuous deformation-fault slip solutions (model 4) demonstrate that most misfits are very small in the Western Mediterranean (Figure 14a-b), with sizes ($\sim 1 \text{ mm/yr}$, $< 1 \text{ mm/yr}$; respectively) that are comparable to the average data error ($\sim 1 \text{ mm/yr}$), implying that the vectors would probably often fall within their prediction error ellipses. That is, usually the errors of the predicted misfits are larger than the original data errors if a regional solution dartboard is utilized since including faraway model errors may result in a relatively large scatter in all possible site predictions (14). Note that the data fit is statistically significant, or very good, if misfit vectors can be enclosed by their model error ellipses.

In contrast to the Western Mediterranean, the data misfits from the GPS and Euler solutions are substantially pronounced in the Eastern Mediterranean (Figure 14c-d), where large vectors ($\geq 5 \text{ mm/yr}$, $\geq 3 \text{ mm/yr}$; respectively) are mainly concentrated near plate boundaries, more specifically around the East and North Anatolian Fault, Western Anatolian Extension Zone, Cephalonia Fault, Corinth Rift, Hellenic Arc, Karasu Rift, and Rhodes Basin (Figure A.1). Such misfit outliers typically fall outside their prediction error ellipses, e.g. see the fit of the synthetic African motions situated close to the Cephalonia Fault and Hellenic Arc (Figure 15a-b). Still, numerous observations located in and near the Aegean Region and Anatolian block fit well (Figure 15), especially for the Euler model.

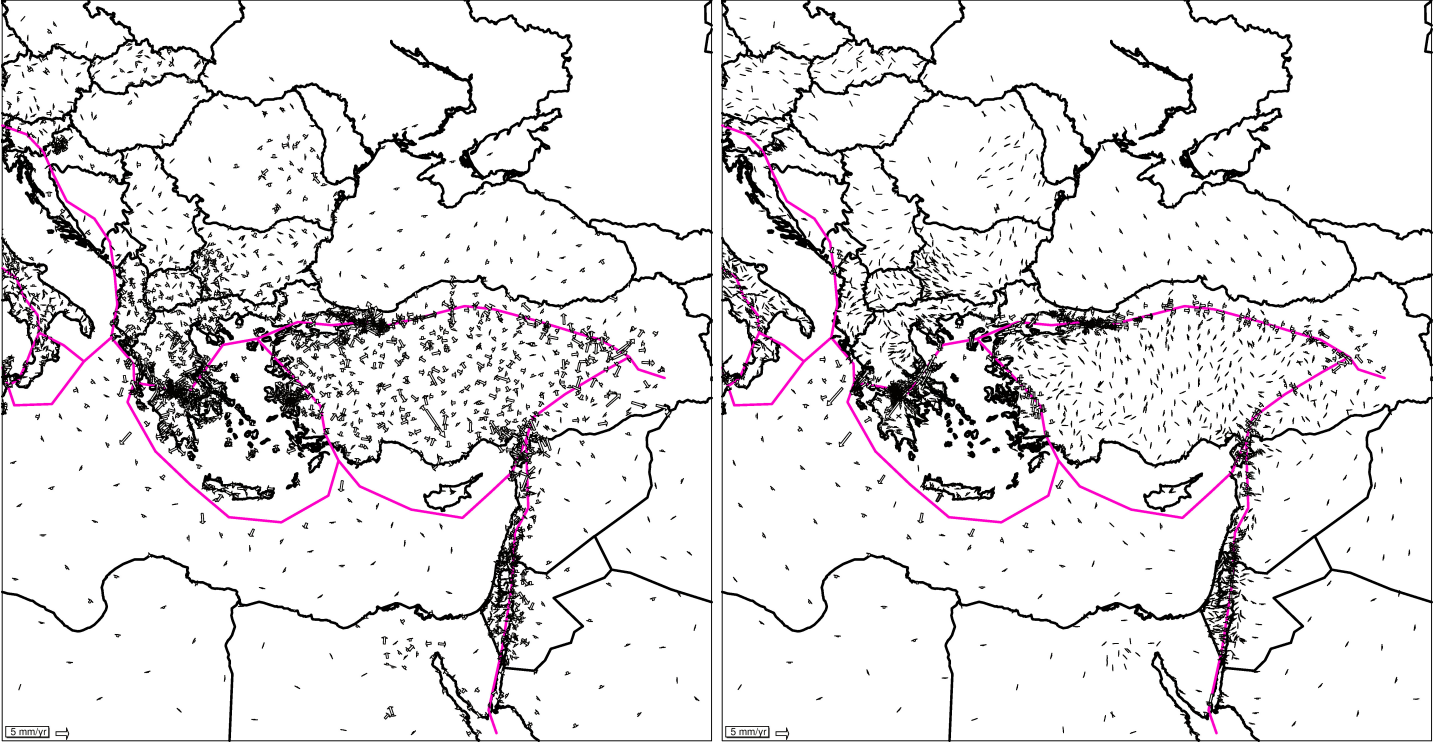
4.4.2.2 Fault Slip, Rotation, and Strain Rate Solutions

Further scrutiny of the GPS and Euler solutions indicates that inverting uniform plate velocities preserves the large-scale kinematic features derived from the real data (Figure 16-17). The best example of this similarity is the fault slip-only model (1; Figure 16a-b), which shows that the average of all fault-crossing integration paths pairing the GPS and synthetic data leads to the same faulting styles as for the Euler dataset. However, the local solution amplitudes may vary significantly between the two data inversion types, being a sign of



(a) Data fit of the joint GPS model (4) in the Western Mediterranean.

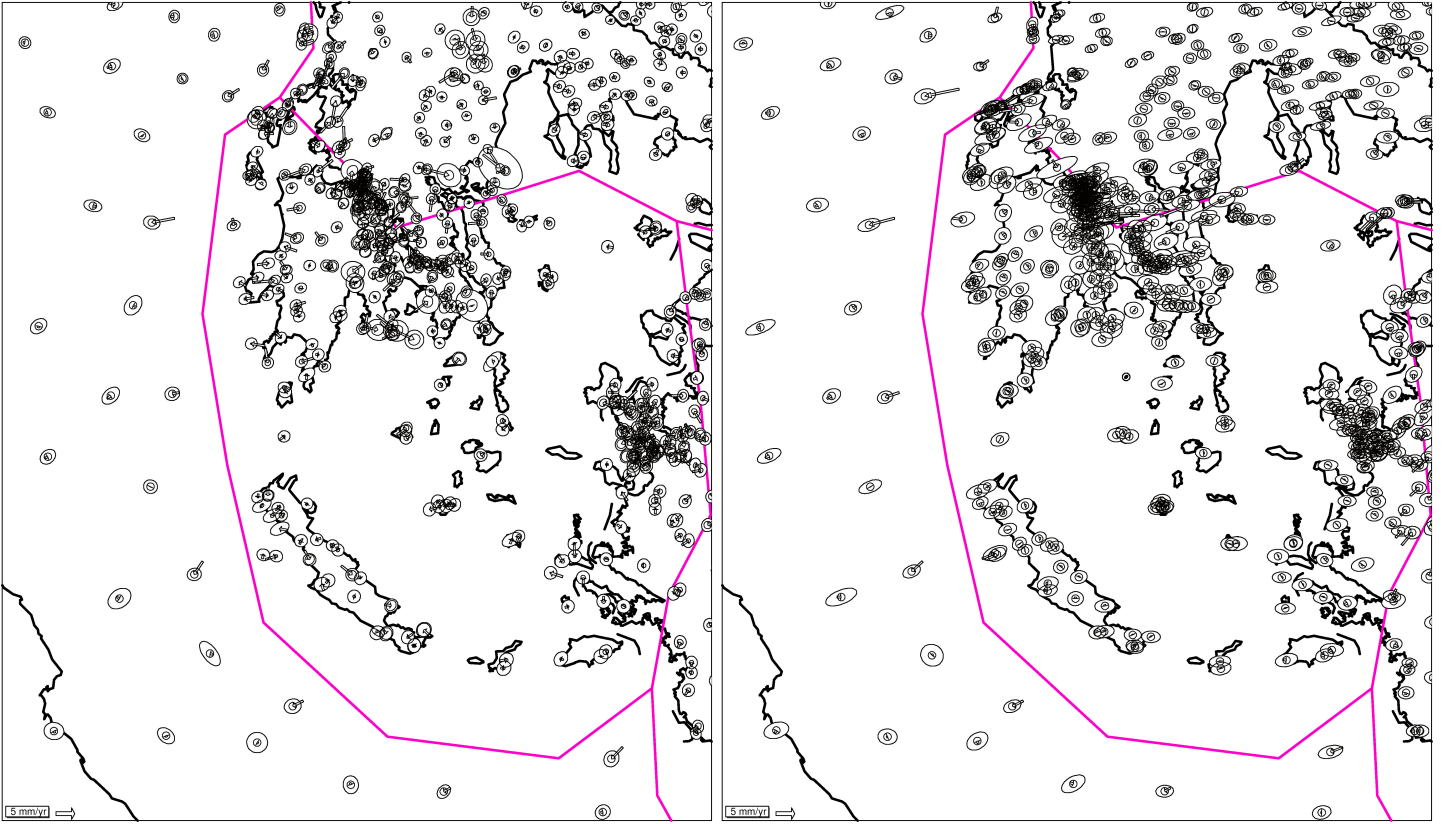
(b) Data fit of the joint Euler model (4) in the Western Mediterranean.



(c) Data fit of the joint GPS model (4) in the Eastern Mediterranean.

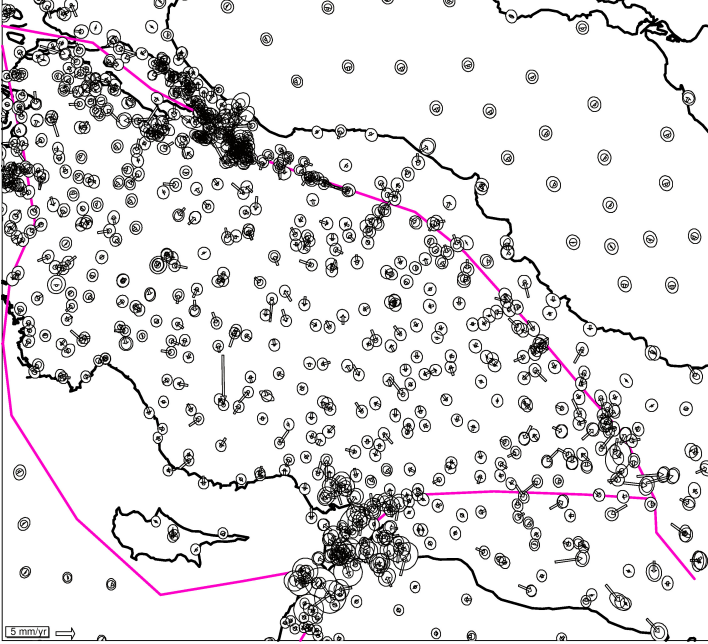
(d) Data fit of the joint Euler model (4) in the Eastern Mediterranean.

Figure 14: Data misfit vectors obtained from damped $\nabla \mathbf{v}$, \mathbf{f}_k -inversion (model 4) of the (a, c) averaged GPS and (b, d) uniform Euler plate motion datasets (Figure 9). In general, the vectors are very small in the Western Mediterranean (a-b), with typical sizes of (a) $\sim 1 \text{ mm/yr}$ and (b) $< 1 \text{ mm/yr}$, hence the data fit is probably (very) good. On the other hand, much larger vectors with notable sizes of (c) $\geq 5 \text{ mm/yr}$ and (d) $\geq 3 \text{ mm/yr}$ characterize the Eastern Mediterranean, in particular near the plate boundary segments (in pink) of the East and North Anatolian Fault, Western Anatolian Extension Zone, Cephalonia Fault, Corinth Rift, Hellenic Arc, Karasu Rift, and Rhodes Basin, see Figure A.1 for a map with these geological features. To assess the statistical significance of the misfit vectors, their data and model error ellipses need to be plotted, see Figure 15. Note that, on average, the data fit is likely better for the Euler than for the GPS model, as is also supported by their model-normalized data fits χ^2_{ν} (9) of 1.19 and 3.59, respectively (Table 3).

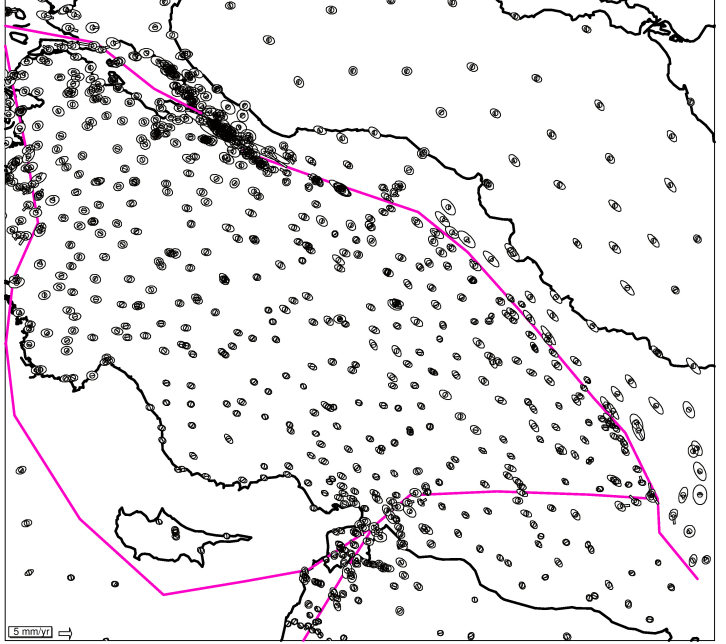


(a) Data fit of the combined GPS model (4) in the Aegean Region.

(b) Data fit of the combined Euler model (4) in the Aegean Region.



(c) Data fit of the combined GPS model (4) in Anatolia.



(d) Data fit of the combined Euler model (4) in Anatolia.

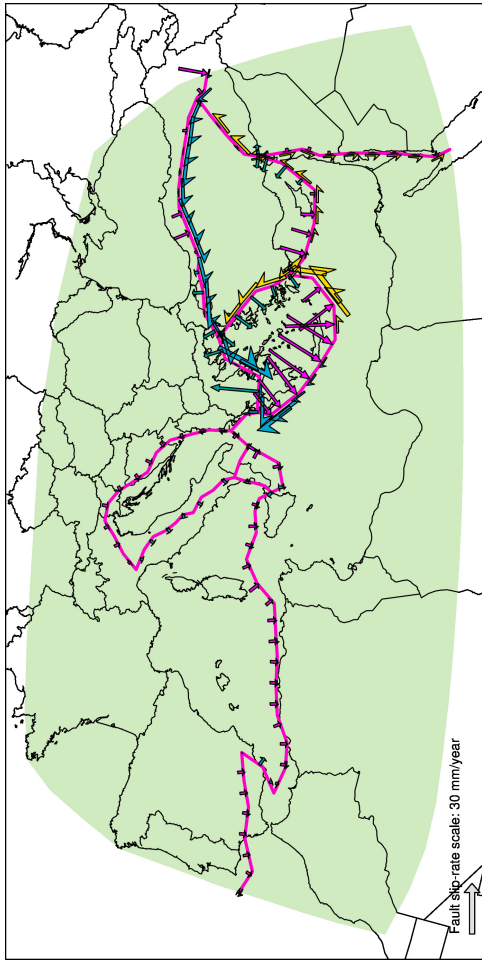
Figure 15: Data misfit vectors in the (a-b) Aegean Region and (c-d) Anatolian block, which belong to damped $\nabla \mathbf{v}$, \mathbf{f}_k -inversion (model 4) of the (a, c) averaged GPS and (b, d) homogeneous Euler plate velocity datasets (Figure 9). The orientation of the Aegean and Anatolian map projections has been rotated clockwise with 40° and 30° relative to the North, respectively. The vectors are visualized together with double 95% confidence error ellipses, where the smaller ellipse usually represents the original data error, and the larger one normally corresponds to the model prediction error. Note the statistically significant misfit vectors that fall outside their model error ellipses and are predominantly found close to faults (in pink), e.g. see (a-b) the synthetic African motions located near the Cephalonia Fault and Hellenic Arc, and (c) the GPS velocities clustered around the triple junction between the East-North Anatolian Fault and Bitlis-Zagros Belt, see Figure A.1 for a map with these geological attributes. Nonetheless, many vectors can be accommodated by their outer ellipses, denoting a (very) good data fit.

internal deformation. This is better illustrated using rigid block rotations (model 2; Figure 16c-d) than solely fault motions (model 1), see the fault slip vector and rotation rate differences between Figure 16c and 16d at the North Aegean Trough, Bitlis-Zagros Belt, southern Calabrian Arc, Cephalonia Fault, Corinth Rift, eastern Cyprian Arc, Dead Sea Fault, Dodecanese, and western Hellenic Arc, and in the Alboran Basin and Betics (Figure A.1).

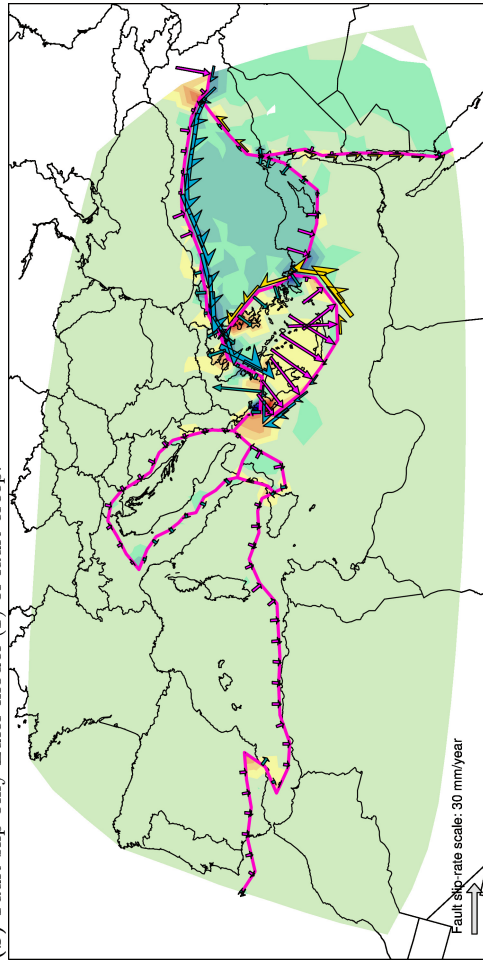
When enabling fault creep as well as distributed deformation (model 4; Figure 16e-f), the fault slip and rotation rate differences are largest at the North Aegean Trough, North Anatolian Fault, Bitlis-Zagros Belt, Cephalonia Fault, Corinth Rift, and Florence Rise (Figure A.1). They are also noteworthy in the entire Western Anatolian Extension Zone and at the East Anatolian Fault and Karasu Rift, where smaller differences can be detected in the block fault solution (model 2; Figure 16c-d). In general, as is apparent from Table 3 and Figure 16, the inversion puts less data signal from the geodetic observations into fault creep than from the Euler velocities (vice versa for rotation rate), resulting in smaller fault slip vectors (and stronger rotation amplitudes) relative to the Euler models. Additionally, overall, the rotation rate field is less homogeneous within individual plates for the GPS inversion than for the Euler one (Figure 16c-f), reflecting intraplate deformation. Note that the Florence Rise, Hellenic Arc, and Marmara fault segment are the only faults with vectors of substantial size in the joint GPS solution (model 4; Figure 16e). The rest of the faults are approximately locked, i.e. have very small slip rates, which may nonetheless signify ongoing fault creep.

For continuous deformation-only (model 3), the same plate boundary parts as for rigid block rotations (model 2) stand out, but now in terms of the variation in principal axes and amplitudes of strain rate between the GPS and Euler models (Figure 17a-b). In Figure 17a and 17b, strain rate differences are visible at the plate boundaries mentioned above for rigid rotation (model 2), East Anatolian Fault, and Karasu Rift, and in the entire Western Anatolian Extension Zone, Alpine Arc, and central Apennines (Figure A.1). After allowing for fault slip (model 4; Figure 17c-d), notable strain rate differences can be seen at the same faults where fault creep and rotation rate differences are present, apart perhaps from the northern Calabrian Arc (Figure 16e-f), which is locked in both the GPS and Euler solutions but has a varying strain and rotation rate.

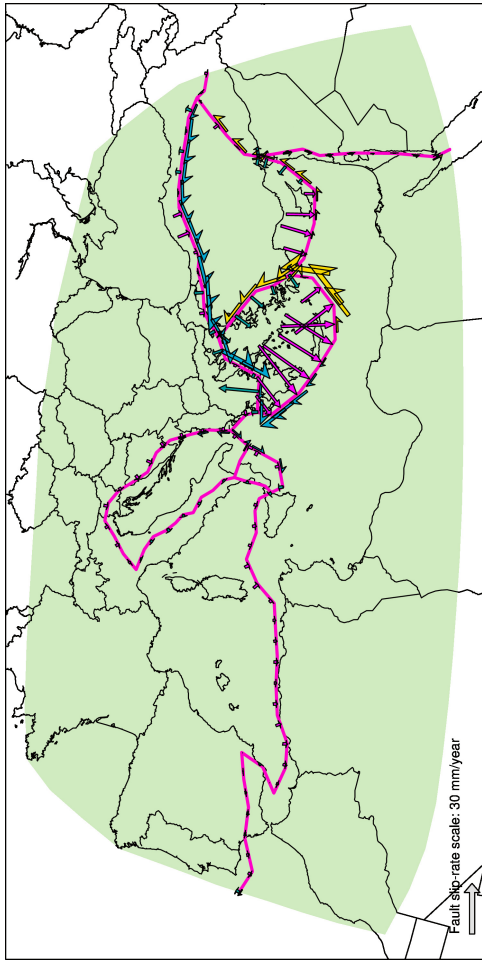
An interesting pattern emerges in the combined Euler model (4) of strain rate accumulating in under-sampled fault-adjacent areas (Figure 17d), particularly in the Western Anatolian Extension Zone, Marmara Sea, and Sardinia Channel, and near the North Aegean Trough, Apulian-Ionian Margin, Bitlis-Zagros Belt, Calabrian Arc, Cephalonia Fault, Corinth Rift, Florence Rise, Hellenic Arc, and Karasu Fault (Figure A.1). In contrast, very low strain rates are obtained at plate boundary nodes if abundant observations are nearby (Figure 17d), e.g. in the Betics and at the East Anatolian Fault and Dead Sea Fault. All in all, the joint Euler inversion (model 4) defines trade-offs between the strain rate and fault slip solutions where fault-local data are lacking, see Section 5.1 for discussion.



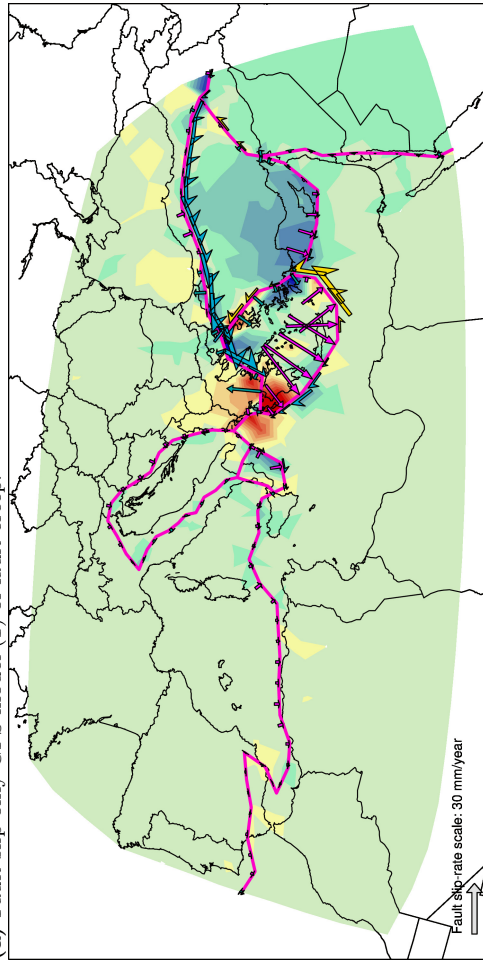
(a) Fault slip-only GPS model (1) of fault creep.



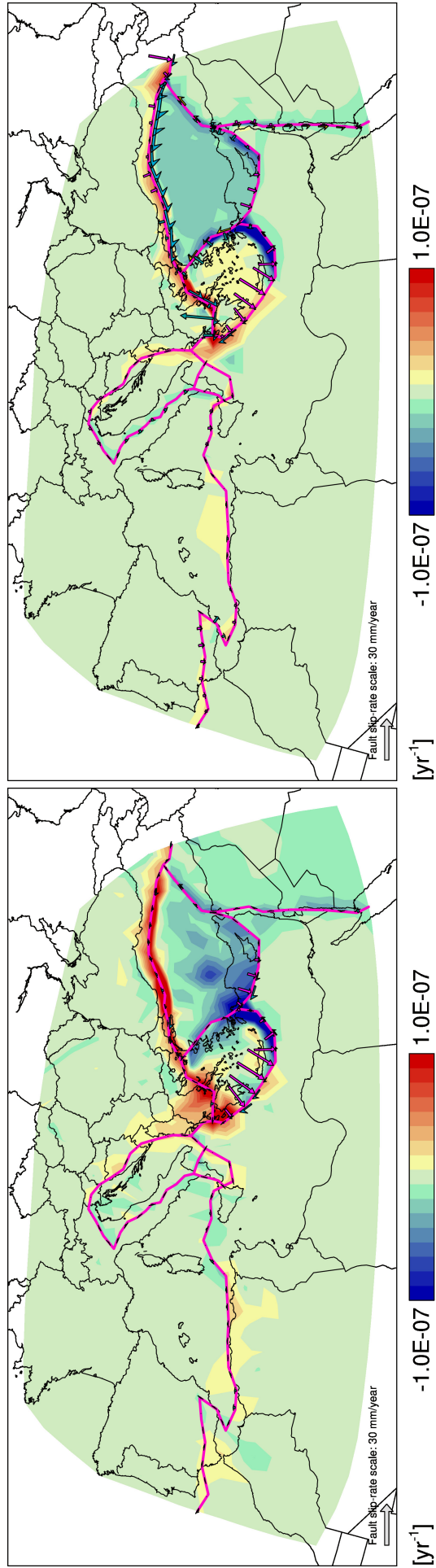
(b) Fault slip-only Euler model (1) of fault creep.



(c) Rigid block rotation GPS model (2) of fault creep and rotation rate.



(d) Rigid block rotation Euler model (2) of fault creep and rotation rate.



(e) Continuous deformation-fault slip GPS model (4) of fault creep and rotation rate.

Figure 16: Fault slip and rotation rate solutions estimated from damped (a-b) \mathbf{f}_k^- , (c-d) $\omega_{\theta\phi}$, and (e-f) $\nabla\mathbf{v}$, \mathbf{f}_k^- , and (e-f) averaged GPS and (b, d, f) uniform Euler plate motion datasets (Figure 9). For reference, fault traces (in pink) are plotted. The fault slip vector colours indicate styles of faulting (yellow: sinistral; lighter blue: dextral; darker blue: normal faulting; pink: reverse faulting), and the contoured bluish (negative) and reddish colours (positive values) of the rotation rate field denote counterclockwise and clockwise rotation, respectively. Note that a rotation rate of $1.0 \cdot 10^{-7} \text{ yr}^{-1}$ is equivalent to $5.7^\circ/\text{Myr}$. Fault creep and rotation rate differences between the GPS and Euler data inversions, where the Euler models generally show larger fault slip vectors and smaller rotation rates, can be interpreted in terms of internal deformation, see the notable differences at (c-d) the southern Calabrian Arc and Dodecanese, and in the Betics; (c-d, e-f) at the North Aegean Trough, Bitlis-Zagros Belt, Cephalonia Fault, Corinth Rift, eastern Cyprian Arc, Dead Sea Fault, and western Hellenic Arc, and in the Alboran Basin; (e-f) at the East and North Anatolian Fault, Florence Rise, and Karasu Rift, and in the entire Western Anatolian Extension Zone, see Figure A.1 for a map with all these geological features. Another indicator of intraplate deformation is the homogeneity of the rotation rate field inside individual plates, often being higher for the Euler solutions than for the GPS ones (model 2, 4; c-f). Nevertheless, overall, the inversion of homogeneous plate velocities represents an averaged version of the actual deformation field, as is best illustrated with the fault-slip only inversion (model 1), see (a-b) the Euler and GPS models that are locally very similar in fault motion type. Note that almost all faults are approximately locked in the joint GPS solution (model 4; e), i.e. have very small creep rates, apart from the Florence Rise, Hellenic Arc, and Marmara fault segment.

(f) Continuous deformation-fault slip Euler model (4) of fault creep and rotation rate.

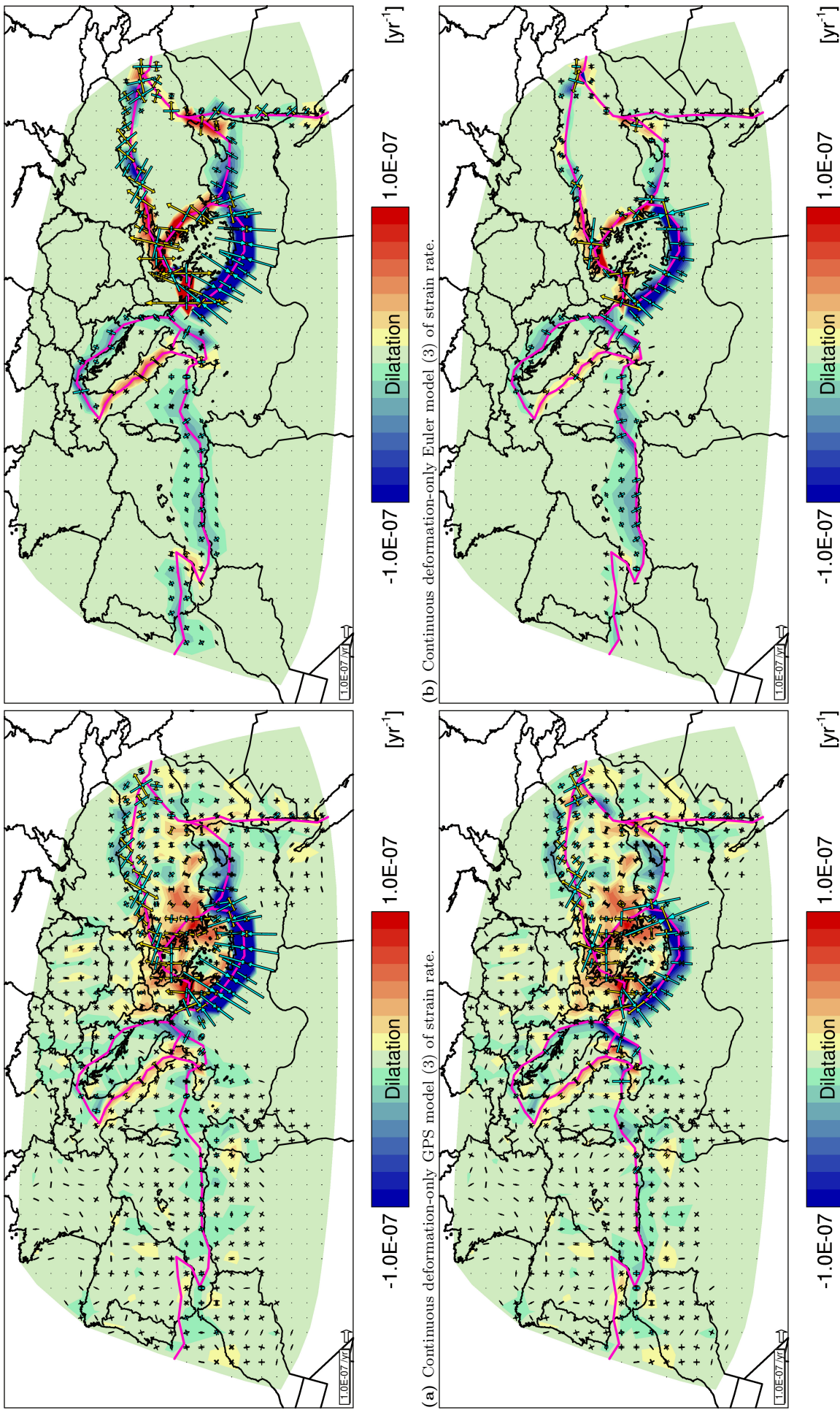


Figure 17: Strain rate solutions estimated from damped (a-b) ∇v - and (c-d) ∇v - and f_k -inversions (model 3-4) of the (a, c) averaged GPS and (b, d) uniform Euler plate motion datasets (Figure 9). For reference, fault traces (in pink) are visualized. The respective blue and yellow vector colours of the principal strain axes are associated with contraction and extension, so are the contoured bluish (negative) and reddish colours (positive values) of the strain rate amplitudes. Differences in the principle axes and amplitudes of strain rate can be interpreted in terms of internal deformation, see the noteworthy differences at (a-b) the southern Calabrian Arc and in the Alpine Arc, central Apennines, and Betics; (a-b, c-d) at the North Aegean Trough, East Anatolian Fault, Bitlis-Zagros Belt, Cephalonia Fault, Corinth Rift, eastern Cyprian Arc, Dead Sea Fault, western Hellenic Arc, and Karasu Rift, and in the Alboran Basin and Western Anatolian Extension Zone; (c-d) at the North Anatolian Fault, northern Calabrian Arc, and Florence Rise, see Figure A.1 for a map with all these geological attributes. Note that, in the combined Euler model (4; d), while strain rates are amplified in data-deficient regions bounding faults, especially in the Western Anatolian Extension Zone, Marmara Sea, and Sardinia Channel, and near the North Aegean Trough, Apulian-Ionian Margin, Bitlis-Zagros Belt, Calabrian Arc, Cephalonia Fault, Corinth Rift, Florence Rise, Hellenic Arc, and Karasu Fault, strain rates are very low in fault-adjacent areas with abundant data, e.g. in the Betics and at the East Anatolian Fault and Dead Sea Fault. In other words, the amount of observations close to faults determines the local trade-off between strain rate and fault slip, see Section 5.1 for discussion.

5 Discussion

Here, our inversion experiments and encountered technical complications are discussed in the broad context of finding better models, software development, and geodynamics.

5.1 Mixed Parameter Inversions

From the geodetic data and Euler motion inversions, we acquire insights into the problematic trade-off between surface fault creep and the velocity gradient tensor in regions short of observations. If few stations close to faults are used for inversion, Tetra generates fault slip estimates reflecting long-term crustal block motion (e.g. at the Hellenic Arc; Figure 16e), whereas incorporating GPS data near faults would lead to the actual zero fault motion (e.g. at the Dead Sea Fault) when the faults had been locked during the observation period. Analogously, in case uniform plate velocities are positioned insufficiently close to plate boundaries, the software locally amplifies strain rate (e.g. at the North Aegean Trough; Figure 17d) in spite of the surrounding Euler data not signalling internal deformation at all.

Essential for understanding trade-off phenomena is to inspect the diagonal elements of the model resolution kernel, ranging from 0 to 1. Basically, the larger they are, the lower the linear dependence (hence trade-off) between model parameters is. However, despite our model-inherent mixed parameter trade-off, which is clearest at the Hellenic Arc and Florence Rise (Figure 16e-f, 17c-d), the undamped resolution diagonal elements are all approximately equal to 1. Based on the resolution matrix product \mathbf{Rm}_{true} (8), we hypothesize that a very small loss of fault slip resolution along the diagonal elements, with typical values of $0.999\dots$, may nevertheless result in a strong trade-off between fault slip and strain-rotation rates due to the contrasting amplitude magnitudes ($10^{-3} m yr^{-1}$ versus $10^{-8} yr^{-1}$, respectively) expected for these parameters of different physical dimensions. Dealing with this requires a detailed examination of the resolution matrix coefficients.

We stress that inserting GPS sites near faults is the foremost solution to the trade-off issue. Secondly, synthetic Euler vectors can be added adjacent to faults if little to no observations are available. However, we may solely be able to improve the Mediterranean model by refining the yet coarse parametrization, potentially increasing the data fit, especially around plate boundaries (e.g. the Hellenic Arc; Figure 14c-d, 15a-b), and maintaining a high model resolution. While the detail of triangulation is appropriate for the Western-Central Mediterranean regarding the predominantly small data misfit vectors (Figure 14a-b), the mesh is locally too rough for fitting both GPS and Euler observations in the Eastern Mediterranean (Figure 14c-d; 15). Furthermore, while the locations of the Adriatic and Calabrian block boundaries are generally compatible with the GPS velocity trends (Figure 10a-b), the fault positions marking the North Anatolian Fault, Cephalonia Fault, Corinth Rift, Karasu Fault, and Western Anatolian Extension Zone are possibly inconsistent with some clustered GPS motions considering their deviation from the Aegean and Anatolian motion frames and their significant data misfit (Figure 10c-d; 14c; 15a, c).

Ways towards a better fault/model parametrization involve doubling the number of fault slip parameters per segment, experimenting with fault locations, constructing smaller fault-neighboring triangles, and/or adapting the triangulation to new fault traces, which may either implicitly (in a locked state) or explicitly contribute to a better data fit, e.g. around the plate boundaries named above. In addition, this future work may allow us to locally study in high resolution the intraplate deformation evident from our Aegean and Anatolian velocity frames and GPS-Euler inversion comparison at the North Anatolian Fault, Cephalonia Island, the Bitlis-Zagros Belt, the Dodecanese, and Lemnos Island, and in the Western Anatolian Extension Zone, Nur Mountains, and Peloponnese Peninsula (Figure 10c-d, 16-17). Useful for such analysis is to only activate faults of interest, which helps to understand the role of individual faults. By refining the grid in combination with placing synthetic data close to both sides of plate boundaries, e.g. at the Calabrian Arc, Florence Rise, and Hellenic Arc, and in the Sardinia Channel, the velocity gradient-fault creep trade-off may be suppressed here. Alternatively, to investigate the trade-off, one can experiment with damping fault slip and doubled velocity gradient nodes, and with equating the velocity gradient field across faults.

Regarding the correction for relative network rotations, the [Borque et al. \[2019\]](#) dataset indicates that the

factors underlying the success of network Euler pole convergence may be more complex than we previously thought. In contrast to the failing pole convergence/calculation of the [Marinou et al. \[2015\]](#), [Walpersdorf et al. \[2015\]](#), and [Bahrouni et al. \[2020\]](#) datasets, which have few to no stations in common with the (extended) Kreemer network, the Euler pole of the [Borque et al. \[2019\]](#) dataset nicely converges through the inversions in spite of the dataset not overlapping with observation points from other networks (Table 2). One reason for this discrepancy may be a trade-off between the velocity gradient field and relative network rotations, which can be explored by inverting for the rotation rate field and network rotations, and for network rotations only.

5.2 Software Complications

Much effort was not solely spent into designing experiments, but also into testing, debugging, and writing Fortran programs and Unix scripts. Early on, a serious software problem in the form of fault slip complications came to light when we noticed that reversing the integration direction erroneously produced different continuous deformation-fault creep solutions whereas the outcomes of a continuous deformation-only inversion stayed the same. During our study, both the fault slip inversion code and data connection strategy were improved, minimizing the model sensitivity to the integration direction and data file permutation, respectively. However, the current versions of the faulting and dartboard algorithms can still be substantially upgraded. We recommend implementing elastic fault loading, which may break the trade-off issue to some extent, and coding a dependency of dartboard size on data density in an attempt to create many relative motion combinations for each site, with a larger dartboard corresponding to a lower data density around datum i (see Section 5.3 for more ideas).

Using the original site connection procedure, we found an alternative solution of statistical nature to the data permutation discrepancy, being the random sorting of the J input data records to decrease the chance of azimuthal artefacts in the integration path distribution. It turns out that any random order of making data pairs gives rise to a robust model, which is insensitive to the permutation, if millions of Mediterranean relative velocity observations are included. Therefore, we argue that a randomly permuted data array is the most valid permutation for a to be inverted dataset. The default Tetra setting of sorting a data file on station code may also be a reasonable permutation if site multiples have been averaged, meaning that the probability of alphabetically grouped co-located observations, and an implicit ordering bias as a consequence, occurring in the data array is reduced. Simultaneously, however, we suppose that any data permutation has insignificant effects on inversion if a relative motion set is assembled with a large dartboard. Note that the ordering bias problem can be easily avoided for fairly small datasets with tens [[Spakman and Hall, 2010](#)] to hundreds [[Bos et al., 2003](#); [Bos and Spakman, 2005](#); [Spakman et al., 2018](#)] of GPS vectors, as the inversion of all of them combined into $J(J-1)/2$ relative velocities is computationally affordable.

5.3 Geodynamic Interpretation

Because of the software issues encountered when inverting for fault creep and linking nearly 10,000 geodetic data points, the focus of our research shifted towards technical experiments, away from the initial primary goal of geodynamic interpretation, for which the time frame proved to be too limited in the end. We have done preliminary work to geodynamic analysis by investigating the influence of several randomly permuted synthetic datasets on the Mediterranean flow field prediction using the old distance strategy.

First, we built the Fortran program *synth_data.f* and Unix scripts effectuating the automatic insertion of synthetic data vectors. Subsequently, the corrected GPS observations were inverted (for the velocity gradient tensor) together with three synthetic datasets of: (1) African, Arabian, and Eurasian motions only put at model boundary nodes, see the locations in Figure 7; (2) these motions placed in the same model portions as from Figure 7, except for the African plate boundary zone, comprising the Atlantic Ocean, Ionian Sea, and Mediterranean Ridge (Figure A.1), which were left unsampled; and (3) the same motions as in Figure 7. We also added synthetic velocities close to fault nodes on the African side, but did not proceed with the experiment due to the discovered fault complications. While the synthetic dataset from Figure 7 may have become the preferred one, it is solely one example of various distributions that need to be tested using the dartboard strategy for future geodynamic interpretation. Note that inversion of a relative motion set

obtained from the GPS data and synthetic dataset 1 with a data density-dependent dartboard would likely demonstrate its practicality, since one would be able to ensure that the model boundary Africa velocities are combined with enough observations without requiring an otherwise fixed dartboard of unnecessarily large radius (e.g. 8°) for all data.

We propose scrutiny of velocity field predictions to be the main step towards geodynamic interpretation-oriented experiments. From a microblock flow prediction, an Euler pole can be determined and visually compared to independently derived (geological) poles and poles estimated from the data, like our Adriatic, Aegean, Anatolian, and Calabrian poles, in terms of their locations and confidence intervals to see if they overlap. The rigid plate rotations may be further explored by varying the selected GPS observations contributing to the Euler poles, and by calculating poles for flow predictions in the data-deficient Adriatic and Aegean Sea. As another application of the velocity prediction tool, one can plot tomographic mantle structure acquired from [Amaru \[2007\]](#) below a prediction field at e.g. 200 or 150 km depth to find correlations. To interpret predicted vectors as an expression of geodynamic drivers, such as slab pull and rollback, the flow prediction may be rotated into a mantle-fixed absolute plate motion frame, which is offered by [Dobrovine et al. \[2012\]](#). These two options are meanwhile available.

It may also be interesting to compare the Mediterranean velocity prediction to that of [Kreemer et al. \[2014\]](#), and to subtract the output prediction field of an Euler motion inversion from that of a GPS data inversion for a more quantitative evaluation of internal deformation than in this study. Similarly, the difference vectors between estimated fault slip rates and "true" homogeneous Euler velocities at the plate boundaries, see Figure 16 and A.8, can be computed for the GPS and Euler inversions to gain deeper insights into intraplate deformation and the inversion itself, respectively. That is, we speculate that a residual between fault creep rates associated with the Euler pole motion calculation and the inversion of the same Euler motions overprinting GPS observations may be related to a loss of fault slip resolution. As a final suggestion, the flow field prediction may serve as an helpful kinematic boundary condition in modelling 3D mantle dynamics.

6 Conclusions

In conclusion, the Spakman-Nyst method and its *Tetra* implementation can be efficiently applied to thousands of observed crustal velocities. We exploited the merits of the dartboard site connection algorithm in combining up to 9181 motion observations through several millions of useful integration paths for pure kinematic inversion of relative velocity data. We were able to iteratively correct 43 merged GPS networks for uniform Euler rotations into the Eurasia-fixed [Kreemer et al. \[2014\]](#) network, leading to a dataset that is negligibly corrupted with technical reference frame artefacts. The large complex deformation field of the Mediterranean Region has been approximated using a coarse model parametrization, in which stiff lithosphere was locally simulated by inserting synthetic vectors and damping strain rate amplitudes. Rigid Euler plate motions were computed for various sub-regions bounded by major faults, inverted, and compared with the geodetic data (inversion) to arrive at a new research approach of analysing internal deformation in the plate boundary zone. This revealed that certain fault-adjacent areas in the Eastern Mediterranean are characterized by a significant data misfit and associated trade-off between the velocity gradient field and surface fault creep if the model resolution is not quite perfect, which illustrate the crucial need for fault-local observations and caution of making model interpretations near faults when these data do not exist.

Acknowledgements

Many thanks go to my supervisor prof. dr. Wim Spakman for providing and debugging the *Tetra* software, developing new software tools, making the software more user-friendly, his numerous inspiring suggestions, and his help whenever needed. Special thanks go to Gino Battistella for working together on our master's thesis projects, to prof. dr. Douwe van Hinsbergen for discussing the plate boundary locations of Adria, to my parents, girlfriend, and stepgrandfather for morally supporting me during the COVID-19 pandemic, and to the master's student crew for the delicious master's lunches and fun times at our workplace.

Data and Software Availability

All original data files of the individual 45 papers used in this study, the combined data files, more details on the data compilation, the *Tetra* software package, and two corresponding user manuals are available through prof. dr. Wim Spakman upon request.

References

- Aktuğ, B., Doğru, A., Özener, H., and Peyret, M. (2015). Slip rates and locking depth variation along central and easternmost segments of north anatolian fault. *Geophysical Journal International*, 202(3):2133–2149.
- Aktug, B., Ozener, H., Dogru, A., Sabuncu, A., Turgut, B., Halicioglu, K., Yilmaz, O., and Havazli, E. (2016). Slip rates and seismic potential on the east anatolian fault system using an improved gps velocity field. *Journal of Geodynamics*, 94:1–12.
- Amaru, M. (2007). *Global travel time tomography with 3-D reference models*, volume 274. Utrecht University.
- Argus, D. F., Gordon, R. G., and DeMets, C. (2011). Geologically current motion of 56 plates relative to the no-net-rotation reference frame. *Geochemistry, Geophysics, Geosystems*, 12(11).
- Aslan, G., Lasserre, C., Cakir, Z., Ergintav, S., Özarpci, S., Dogan, U., Bilham, R., and Renard, F. (2019). Shallow creep along the 1999 izmit earthquake rupture (turkey) from gps and high temporal resolution interferometric synthetic aperture radar data (2011–2017). *Journal of Geophysical Research: Solid Earth*, 124(2):2218–2236.
- Bahrouni, N., Masson, F., Meghraoui, M., Saleh, M., Maamri, R., Dhaha, F., and Arfaoui, M. (2020). Active tectonics and gps data analysis of the maghrebien thrust belt and africa-eurasia plate convergence in tunisia. *Tectonophysics*, 785:228440.
- Barreca, G., Bruno, V., Cocorullo, C., Cultrera, F., Ferranti, L., Guglielmino, F., Guzzetta, L., Mattia, M., Monaco, C., and Pepe, F. (2014a). Geodetic and geological evidence of active tectonics in south-western sicily (italy). *Journal of geodynamics*, 82:138–149.
- Barreca, G., Bruno, V., Cultrera, F., Mattia, M., Monaco, C., and Scarfi, L. (2014b). New insights in the geodynamics of the lipari–vulcano area (aeolian archipelago, southern italy) from geological, geodetic and seismological data. *Journal of Geodynamics*, 82:150–167.
- Beavan, J. and Haines, J. (2001). Contemporary horizontal velocity and strain rate fields of the pacific-australian plate boundary zone through new zealand. *Journal of Geophysical Research: Solid Earth*, 106(B1):741–770.
- Bijwaard, H., Spakman, W., and Engdahl, E. R. (1998). Closing the gap between regional and global travel time tomography. *Journal of Geophysical Research: Solid Earth*, 103(B12):30055–30078.
- Borque, M., Sánchez-Alzola, A., Martín-Rojas, I., Alfaro, P., Molina, S., Rosa-Cintas, S., Rodríguez-Caderot, G., de Lacy, C., García-Armenteros, J., Avilés, M., et al. (2019). How much nubia-eurasia convergence is accommodated by the ne end of the eastern betic shear zone (se spain)? constraints from gps velocities. *Tectonics*, 38(5):1824–1839.
- Bos, A. G. and Spakman, W. (2005). Kinematics of the southwestern us deformation zone inferred from gps motion data. *Journal of Geophysical Research: Solid Earth*, 110(B8).
- Bos, A. G., Spakman, W., and Nyst, M. C. (2003). Surface deformation and tectonic setting of taiwan inferred from a gps velocity field. *Journal of Geophysical Research: Solid Earth*, 108(B10).
- Bougrine, A., Yelles-Chaouche, A. K., and Calais, E. (2019). Active deformation in algeria from continuous gps measurements. *Geophysical Journal International*, 217(1):572–588.

- Bourne, S., Arnadottir, T., Beavan, J., Darby, D., England, P., Parsons, B., Walcott, R., and Wood, P. (1998). Crustal deformation of the marlborough fault zone in the south island of new zealand: Geodetic constraints over the interval 1982–1994. *Journal of Geophysical Research: Solid Earth*, 103(B12):30147–30165.
- Cabral, J., Mendes, V. B., Figueiredo, P., da Silveira, A. B., Pagarete, J., Ribeiro, A., Dias, R., and Ressurreição, R. (2017). Active tectonics in southern portugal (sw iberia) inferred from gps data. implications on the regional geodynamics. *Journal of Geodynamics*, 112:1–11.
- Cardozo, N. and Allmendinger, R. W. (2009). Sspcx: A program to compute strain from displacement/velocity data. *Computers & Geosciences*, 35(6):1343–1357.
- Chousianitis, K., Ganas, A., and Evangelidis, C. P. (2015). Strain and rotation rate patterns of mainland greece from continuous gps data and comparison between seismic and geodetic moment release. *Journal of Geophysical Research: Solid Earth*, 120(5):3909–3931.
- Çırmık, A., Pamukçu, O., Gönenç, T., Kahveci, M., Şalk, M., and Herring, T. (2017). Examination of the kinematic structures in izmir (western anatolia) with repeated gps observations (2009, 2010 and 2011). *Journal of African Earth Sciences*, 126:1–12.
- Civiero, C., Custódio, S., Duarte, J. C., Mendes, V. B., and Faccenna, C. (2020). Dynamics of the gibraltar arc system: A complex interaction between plate convergence, slab pull, and mantle flow. *Journal of Geophysical Research: Solid Earth*, 125(7):e2019JB018873.
- D’Agostino, N., Avallone, A., Cheloni, D., D’anastasio, E., Mantenuto, S., and Selvaggi, G. (2008). Active tectonics of the adriatic region from gps and earthquake slip vectors. *Journal of Geophysical Research: Solid Earth*, 113(B12).
- D’Agostino, N., Métois, M., Koci, R., Duni, L., Kuka, N., Ganas, A., Georgiev, I., Jouanne, F., Kaludjerovic, N., and Kandić, R. (2020). Active crustal deformation and rotations in the southwestern balkans from continuous gps measurements. *Earth and Planetary Science Letters*, 539:116246.
- D’Agostino, N., Silverii, F., Amoroso, O., Convertito, V., Fiorillo, F., Ventafridda, G., and Zollo, A. (2018). Crustal deformation and seismicity modulated by groundwater recharge of karst aquifers. *Geophysical Research Letters*, 45(22):12–253.
- Danesi, S., Pondrelli, S., Salimbeni, S., Cavaliere, A., Serpelloni, E., Danecek, P., Lovati, S., and Massa, M. (2015). Active deformation and seismicity in the southern alps (italy): The montello hill as a case study. *Tectonophysics*, 653:95–108.
- Davies, R., England, P., Parsons, B., Billiris, H., Paradissis, D., and Veis, G. (1997). Geodetic strain of greece in the interval 1892–1992. *Journal of Geophysical Research: Solid Earth*, 102(B11):24571–24588.
- Doubrovine, P. V., Steinberger, B., and Torsvik, T. H. (2012). Absolute plate motions in a reference frame defined by moving hot spots in the pacific, atlantic, and indian oceans. *Journal of Geophysical Research: Solid Earth*, 117(B9).
- Echeverria, A., Khazaradze, G., Asensio, E., and Masana, E. (2015). Geodetic evidence for continuing tectonic activity of the carboneras fault (se spain). *Tectonophysics*, 663:302–309.
- Ergintav, S., Reilinger, R., Çakmak, R., Floyd, M., Cakir, Z., Doğan, U., King, R., McClusky, S., and Özener, H. (2014). Istanbul’s earthquake hot spots: Geodetic constraints on strain accumulation along faults in the marmara seismic gap. *Geophysical Research Letters*, 41(16):5783–5788.
- Esposito, A., Pietrantonio, G., Bruno, V., Anzidei, M., Bonforte, A., Guglielmino, F., Mattia, M., Puglisi, G., Sepe, V., and Serpelloni, E. (2015). Eighteen years of gps surveys in the aeolian islands (southern italy): open data archive and velocity field. *Ann. Geophys*, 58(4):S0439.
- Faccenna, C., Becker, T. W., Auer, L., Billi, A., Boschi, L., Brun, J. P., Capitanio, F. A., Funicello, F., Horvath, F., Jolivet, L., et al. (2014). Mantle dynamics in the mediterranean. *Reviews of Geophysics*, 52(3):283–332.
- Galindo-Zaldivar, J., Gil, A., de Galdeano, C. S., Lacy, M., García-Armenteros, J., Ruano, P., Ruiz, A., Martínez-Martos, M., and Alfaro, P. (2015). Active shallow extension in central and eastern betic cordillera from cgps data. *Tectonophysics*, 663:290–301.
- Garate, J., Martin-Davila, J., Khazaradze, G., Echeverria, A., Asensio, E., Gil, A. J., de Lacy, M., Armenteros, J., Ruiz, A., Gallastegui, J., et al. (2015). Topo-iberia project: Cgps crustal velocity field in the iberian peninsula and morocco. *GPS Solutions*, 19(2):287–295.
- Gomez, F., Cochran, W. J., Yassminh, R., Jaafar, R., Reilinger, R., Floyd, M., King, R. W., and Barazangi, M. (2020). Fragmentation of the sinai plate indicated by spatial variation in present-day slip rate along the dead sea fault system. *Geophysical Journal International*, 221(3):1913–1940.

- Gonzalez-Castillo, L., Galindo-Zaldívar, J., de Lacy, M., Borque, M., Martínez-Moreno, F., García-Armenteros, J., and Gil, A. (2015). Active rollback in the gibraltar arc: Evidences from cgps data in the western betic cordillera. *Tectonophysics*, 663:310–321.
- Hackl, M., Malservisi, R., and Wdowinski, S. (2009). Strain rate patterns from dense gps networks. *Natural Hazards and Earth System Sciences*, 9(4):1177–1187.
- Haines, A. and Holt, W. (1993). A procedure for obtaining the complete horizontal motions within zones of distributed deformation from the inversion of strain rate data. *Journal of Geophysical Research: Solid Earth*, 98(B7):12057–12082.
- Hamiel, Y., Masson, F., Piatibratova, O., and Mizrahi, Y. (2018a). Gps measurements of crustal deformation across the southern arava valley section of the dead sea fault and implications to regional seismic hazard assessment. *Tectonophysics*, 724:171–178.
- Hamiel, Y., Piatibratova, O., and Mizrahi, Y. (2016). Creep along the northern jordan valley section of the dead sea fault. *Geophysical Research Letters*, 43(6):2494–2501.
- Hamiel, Y., Piatibratova, O., Mizrahi, Y., Nahmias, Y., and Sagy, A. (2018b). Crustal deformation across the jericho valley section of the dead sea fault as resolved by detailed field and geodetic observations. *Geophysical Research Letters*, 45(7):3043–3050.
- Howe, T. M. and Bird, P. (2010). Exploratory models of long-term crustal flow and resulting seismicity across the alpine-aegean orogen. *Tectonics*, 29(4).
- Kahle, H.-G., Cocard, M., Peter, Y., Geiger, A., Reilinger, R., Barka, A., and Veis, G. (2000). Gps-derived strain rate field within the boundary zones of the eurasian, african, and arabian plates. *Journal of Geophysical Research: Solid Earth*, 105(B10):23353–23370.
- Kreemer, C., Blewitt, G., and Klein, E. C. (2014). A geodetic plate motion and global strain rate model. *Geochemistry, Geophysics, Geosystems*, 15(10):3849–3889.
- Lamb, S. H. (1994). Behavior of the brittle crust in wide plate boundary zones. *Journal of Geophysical Research: Solid Earth*, 99(B3):4457–4483.
- Mantovani, E., Viti, M., Cenni, N., Babbucci, D., Tamburelli, C., Baglione, M., and D’Intinosante, V. (2015). Seismotectonics and present seismic hazard in the tuscan–romagna–marche–umbria apennines (italy). *Journal of Geodynamics*, 89:1–14.
- Marinou, A., Ganas, A., Papazissi, K., and Paradissis, D. (2015). Strain patterns along the kaparelli–asopos rift (central greece) from campaign gps data. *Annals of Geophysics*, 58(2):0219.
- Masson, F., Hamiel, Y., Agnon, A., Klinger, Y., and Deprez, A. (2015). Variable behavior of the dead sea fault along the southern arava segment from gps measurements. *comptes rendus geoscience*, 347(4):161–169.
- Masson, F., Lehujeur, M., Ziegler, Y., and Doubre, C. (2014). Strain rate tensor in iran from a new gps velocity field. *Geophysical Journal International*, 197(1):10–21.
- Metois, M., D’Agostino, N., Avallone, A., Chamot-Rooke, N., Rabaute, A., Duni, L., Kuka, N., Koci, R., and Georgiev, I. (2015). Insights on continental collisional processes from gps data: Dynamics of the peri-adriatic belts. *Journal of Geophysical Research: Solid Earth*, 120(12):8701–8719.
- Mouslopoulou, V., Saltogianni, V., Gianniou, M., and Stiros, S. (2014). Geodetic evidence for tectonic activity on the strymon fault system, northeast greece. *Tectonophysics*, 633:246–255.
- Nguyen, H., Vernant, P., Mazzotti, S., Khazaradze, G., and Asensio Ferreira, E. (2016). 3d gps velocity field and its implications on the present-day postorogenic deformation of the western alps and pyrenees. *Solid Earth*, 2016, vol. 7, p. 1349–1363.
- Nijholt, N., Govers, R., and Wortel, R. (2018). On the forces that drive and resist deformation of the south-central mediterranean: a mechanical model study. *Geophysical Journal International*, 214(2):876–894.
- Özdemir, S. and Karshoğlu, M. O. (2019). Soft clustering of gps velocities from a homogeneous permanent network in turkey. *Journal of Geodesy*, 93(8):1171–1195.
- Palano, M., González, P. J., and Fernández, J. (2015). The diffuse plate boundary of nubia and iberia in the western mediterranean: Crustal deformation evidence for viscous coupling and fragmented lithosphere. *Earth and Planetary Science Letters*, 430:439–447.
- Palano, M., Imprescia, P., Agnon, A., and Gresta, S. (2018). An improved evaluation of the seismic/geodetic deformation-rate ratio for the zagros fold-and-thrust collisional belt. *Geophysical Journal International*, 213(1):194–209.

- Pietrantonio, G., Devoti, R., Mahmoud, S., and Riguzzi, F. (2016). Kinematics of the suez-sinai area from combined gps velocity field. *Journal of geodynamics*, 102:231–238.
- Rabin, M., Sue, C., Walpersdorf, A., Sakic, P., Albaric, J., and Fores, B. (2018). Present-day deformations of the jura arc inferred by gps surveying and earthquake focal mechanisms. *Tectonics*, 37(10):3782–3804.
- Rawlinson, N. and Spakman, W. (2016). On the use of sensitivity tests in seismic tomography. *Geophysical Journal International*, 205(2):1221–1243.
- Reilinger, R., McClusky, S., Vernant, P., Lawrence, S., Ergintav, S., Cakmak, R., Ozener, H., Kadirov, F., Guliev, I., Stepanyan, R., et al. (2006). Gps constraints on continental deformation in the africa-arabia-eurasia continental collision zone and implications for the dynamics of plate interactions. *Journal of Geophysical Research: Solid Earth*, 111(B5).
- Rigo, A., Vernant, P., Feigl, K., Goula, X., Khazaradze, G., Talaya, J., Morel, L., Nicolas, J., Baize, S., Chery, J., et al. (2015). Present-day deformation of the pyrenees revealed by gps surveying and earthquake focal mechanisms until 2011. *Geophysical Journal International*, 201(2):947–964.
- Saleh, M. and Becker, M. (2015). New constraints on the nubia–sinai–dead sea fault crustal motion. *Tectonophysics*, 651:79–98.
- Sánchez, L., Völksen, C., Sokolov, A., Arenz, H., and Seitz, F. (2018). Present-day surface deformation of the alpine region inferred from geodetic techniques. *Earth System Science Data*, 10(3):1503–1526.
- Serpelloni, E., Vannucci, G., Anderlini, L., and Bennett, R. A. (2016). Kinematics, seismotectonics and seismic potential of the eastern sector of the european alps from gps and seismic deformation data. *Tectonophysics*, 688:157–181.
- Serpelloni, E., Vannucci, G., Pondrelli, S., Argnani, A., Casula, G., Anzidei, M., Baldi, P., and Gasperini, P. (2007). Kinematics of the western africa-eurasia plate boundary from focal mechanisms and gps data. *Geophysical Journal International*, 169(3):1180–1200.
- Shen, Z.-K., Jackson, D. D., and Ge, B. X. (1996). Crustal deformation across and beyond the los angeles basin from geodetic measurements. *Journal of Geophysical Research: Solid Earth*, 101(B12):27957–27980.
- Shewchuk, J. R. (1996). Triangle: Engineering a 2d quality mesh generator and delaunay triangulator. In *Workshop on Applied Computational Geometry*, pages 203–222. Springer.
- Silverii, F., D’Agostino, N., Borsa, A. A., Calcaterra, S., Gambino, P., Giuliani, R., and Mattone, M. (2019). Transient crustal deformation from karst aquifers hydrology in the apennines (italy). *Earth and Planetary Science Letters*, 506:23–37.
- Spakman, W., Chertova, M. V., van den Berg, A., and van Hinsbergen, D. J. (2018). Puzzling features of western mediterranean tectonics explained by slab dragging. *Nature Geoscience*, 11(3):211–216.
- Spakman, W. and Hall, R. (2010). Surface deformation and slab–mantle interaction during banda arc subduction rollback. *Nature Geoscience*, 3(8):562–566.
- Spakman, W. and Nyst, M. (2002). Inversion of relative motion data for estimates of the velocity gradient field and fault slip. *Earth and Planetary Science Letters*, 203(1):577–591.
- Tape, C., Musé, P., Simons, M., Dong, D., and Webb, F. (2009). Multiscale estimation of gps velocity fields. *Geophysical Journal International*, 179(2):945–971.
- Van Hinsbergen, D. J., Torsvik, T. H., Schmid, S. M., Mañenco, L. C., Maffione, M., Vissers, R. L., Gürer, D., and Spakman, W. (2020). Orogenic architecture of the mediterranean region and kinematic reconstruction of its tectonic evolution since the triassic. *Gondwana Research*, 81:79–229.
- van Unen, M., Matenco, L., Demir, V., Nader, F. H., Darnault, R., and Mandic, O. (2019). Transfer of deformation during indentation: Inferences from the post-middle miocene evolution of the dinarides. *Global and Planetary Change*, 182:103027.
- Ventura, B. M., Serpelloni, E., Argnani, A., Bonforte, A., Bürgmann, R., Anzidei, M., Baldi, P., and Puglisi, G. (2014). Fast geodetic strain-rates in eastern sicily (southern italy): New insights into block tectonics and seismic potential in the area of the great 1693 earthquake. *Earth and planetary science letters*, 404:77–88.
- Walpersdorf, A., Pinget, L., Vernant, P., Sue, C., Deprez, A., and team, R. (2018). Does long-term gps in the western alps finally confirm earthquake mechanisms? *Tectonics*, 37(10):3721–3737.
- Walpersdorf, A., Sue, C., Baize, S., Cotte, N., Bascou, P., Beauval, C., Collard, P., Daniel, G., Dyer, H., Grasso, J.-R., et al. (2015). Coherence between geodetic and seismic deformation in a context of slow tectonic activity (sw alps, france). *Journal of Geodynamics*, 85:58–65.
- Ward, S. N. (1998). On the consistency of earthquake moment rates, geological fault data, and space geodetic strain: the united states. *Geophysical Journal International*, 134(1):172–186.
- Wortel, M. and Spakman, W. (2000). Subduction and slab detachment in the mediterranean-carpethian region. *Science*, 290(5498):1910–1917.

Appendix

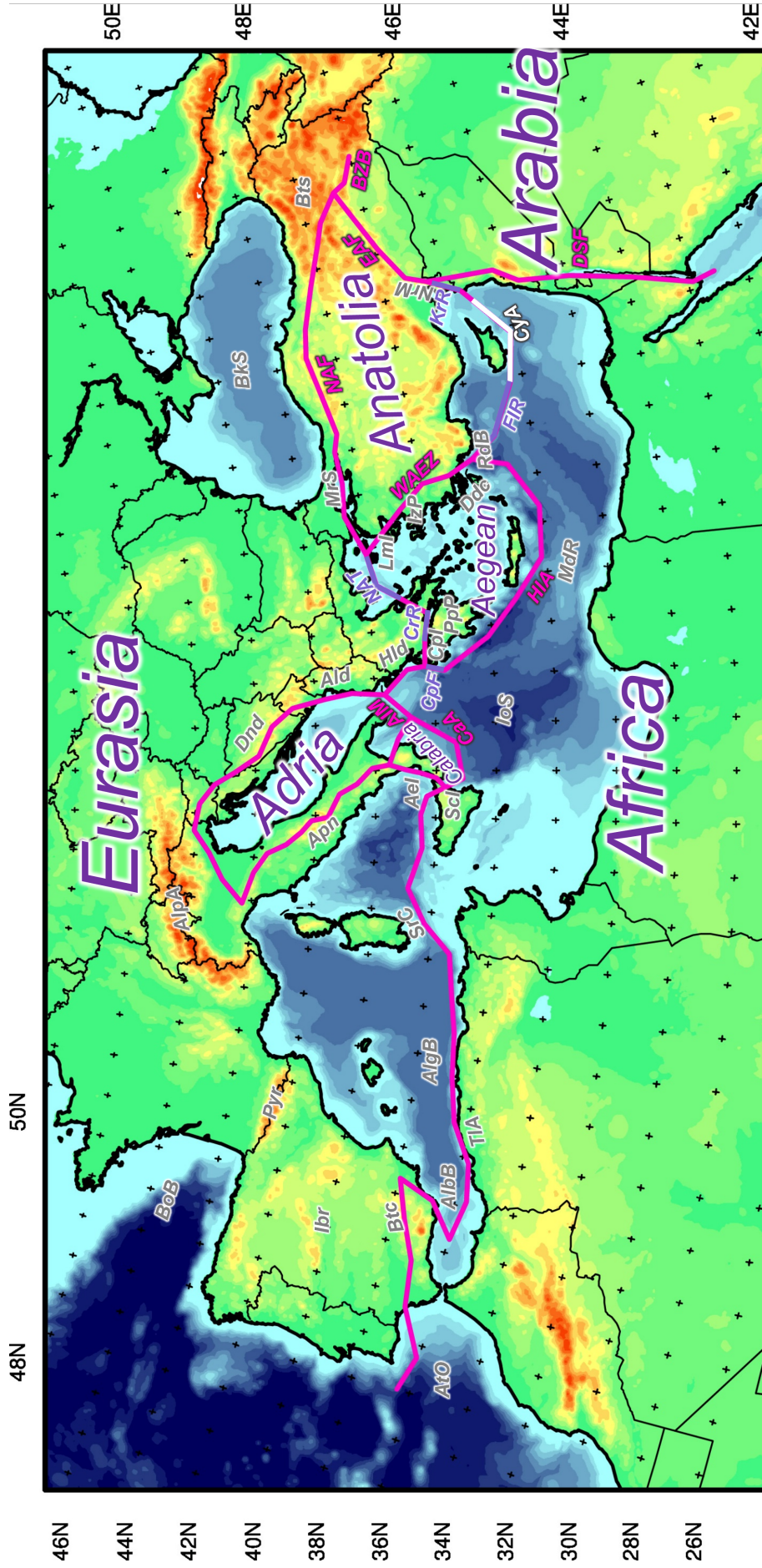


Figure A.1: Adopted fault parametrization (in pink) in relation to the plate tectonic setting of the Mediterranean, e.g. as described by Faccenna et al. [2014] (Figure 1), see Section 4.1 for more references on which the fault locations are based. The surface traces of included plate boundary faults outline the major lithospheric African, Arabian, and Eurasian plates, and the Adriatic, Aegean, Anatolian, and Calabrian microblocks. Important geological features (in grey text) that mark the Western and Central Mediterranean plate boundaries consist of the Aeolian Islands (Ael), Albanides (Alb), Alboran Basin (AlbB), Algerian Basin (Algb), Alpine Arc (AlpA), Apennines (Apm), Betics (Btc), Dinarides (Dnd), Hellenides (Hld), Sardinia Channel (SrC), Sicily (Scl), and Tell Atlas (TIA). In the Eastern Mediterranean, the Rhodes Basin (RdB) stands out. A couple of (major) Central and Eastern Mediterranean plate boundaries with triple junction endpoints have been established, of which the following (in pink text) are specifically named in our report: the East and North Anatolian Fault (EAF, NAF), Western Anatolian Extension Zone (WAEZ), Apulian-Ionian Margin (AIM), Bitlis-Zagros Belt (BZB), Calabrian Arc (CaA), and Dead Sea Fault (DSF). Three of such triple junction-terminating faults are defined by multiple segments, being: (1) the North Aegean Trough (NAT) and Corinth Rift (CrR); (2) Cephalonia Fault (CpF) and Hellenic Arc (HLA); and (3) the Cyprian Arch (CyA), Florence Rise (FlR), and Karasu Rift (KrR). The remaining geological/geographical attributes (in grey) of the Mediterranean discussed by us comprise the Atlantic Ocean (AtO), the Bay of Biscay (BoB), Bitlis (Bts), the Black Sea (BkS), the Dodecanese (Ddc), Iberia (Ibr), the Ionian Sea (IoS), the Izmir Province (IzP), Limnos Island (LmI), the Marmara Sea (MrS), the Mediterranean Ridge (Mdr), the Nur Mountains (NrM), the Peloponnese Peninsula (PpP), and the Pyrenees (Pyr).

Incorporated studies	Main study region	Vector colour	Motion reference frame	Number of collected data	Data type	Observation period
Kreemer et al. [2014]	World		Eurasia	3981	GPS	1996-2013
Echeverria et al. [2015]	Betics		Eurasia	30	CGPS, SGPS	4.5 yr, 2008-2013
Galindo-Zaldívar et al. [2015]	Betics		Eurasia	12	CGPS	2008-2013
Garate et al. [2015]	Iberia, Morocco		Eurasia	26	CGPS	4 yr, 2008-2012
Gonzalez-Castillo et al. [2015]	Betics		IGb08	10	CGPS	2008-2013
Palano et al. [2015]	Iberia, Morocco		Eurasia	320	CGNSS, SGNSS	15 yr, 1999-2014
Cabral et al. [2017]	Algarve		ITRF2008	34	CGPS, SGPS	16.5 yr, 1998-2016
Borque et al. [2019]	Betics		IGb08	10	CGPS	13 yr, 1999-2013
Civiero et al. [2020]	Southern Iberia, Morocco		Eurasia	141	CGPS	25 yr, 1995-2019
Bougrine et al. [2019]	Algeria		ITRF2014	105	CGPS, GNSS	10 yr, 2007-2017
Bahrouni et al. [2020]	Tunisia		Eurasia	18	CGNSS, SGPS	2014-2018
Barreca et al. [2014a]	Sicily		Eurasia	5	SGPS	1994-2013
Barreca et al. [2014b]	Aeolian Islands		Eurasia	40	CGPS, SGPS	2000-2013
Ventura et al. [2014]	Southern Italy		ITRF2008	155	CGPS, SGPS	1993-2008
Esposito et al. [2015]	Aeolian Islands		Eurasia	28	SGPS	18 yr, 1996-2013
Mantovani et al. [2015]	Central-northern Apennines		ITRF2008	209	CGPS	2001-2014
Mezies et al. [2015]	Italy, eastern Alps, Balkan		Eurasia	662	CGPS	2000-2014
D'Agostino et al. [2018]	Southern Apennines		Tyrrhenian	66	CGPS	2000-2017
Silverii et al. [2019]	Central-southern Apennines		Tyrrhenian	184	CGPS	2004-2016
Danesi et al. [2015]	Southeastern Alps		Eurasia	74	CGPS, sCGPS	1998-2013
Rigo et al. [2015]	Pyrenees		Eurasia	91	CGPS, SGPS	18 yr, 1992-2010
Walpersdorf et al. [2015]	Southwestern Alps		Eurasia	35	SGPS	16 yr, 1996-2011
Nguyen et al. [2016]	Western Alps, Pyrenees		Eurasia	179	CGNSS	16 yr, 1997-2013
Serpelloni et al. [2016]	Alps, central-northern Apennines		NNR	456	CGPS, sCGPS	1994-2015
Rabin et al. [2018]	Northwestern Alps		Eurasia	49	CGPS	15 yr, 2000-2015
Sánchez et al. [2018]	Alps		Eurasia	180	CGNSS	12.5 yr, 2004-2016
Walpersdorf et al. [2018]	Western Alps		Eurasia	111	CGPS, SGPS	22 yr, 1993-2015
Ergintav et al. [2014]	Marmara Sea		Eurasia	112	CGPS, SGPS	20 yr, 1994-2014
Monslopoulou et al. [2014]	North-eastern Greece		ITRF2008	20	CGPS	5.5 yr, 2008-2013
Aktugç et al. [2015]	North Anatolian Fault		Eurasia	38	CGPS, SGPS	1994-2014
Chousianitis et al. [2015]	Greece		Eurasia	99	CGPS	2003-2013
Marinou et al. [2015]	Central Greece		Eurasia	11	SGPS	2004-2008
Aktugç et al. [2016]	East Anatolian Fault		ITRF2008	48	CGPS, SGPS	1998-2010
Çirmik et al. [2017]	Izmir Province		Eurasia	30	CGPS, SGPS	2009-2011
Aslan et al. [2019]	Marmara Sea		Eurasia	33	InSAR, CGPS, SGPS	2011-2017
Özdemir and Karşioğlu [2019]	Turkey		Eurasia	184	CGPS	10 yr, 2008-2018
D'Agostino et al. [2020]	Balkan, Aegean Region		Eurasia	329	CGPS	2000-2019
Masson et al. [2015]	Dead Sea Fault		Arabia	26	CGPS, SGPS	12 yr, 1999-2012
Saleh and Becker [2015]	Egypt, Dead Sea Fault		Eurasia	55	CGPS, SGPS	2006-2012
Pietrantonio et al. [2016]	Egypt, Dead Sea Fault		IGb08	385	CGPS, SGPS	1996-2015
Hamiel et al. [2016]	Dead Sea Fault		Sinai	68	CGPS, SGPS	2009-2015
Hamiel et al. [2018a]	Dead Sea Fault		Sinai	56	CGPS, SGPS	1992-2017
Hamiel et al. [2018b]	Dead Sea Fault		Sinai	51	CGPS, SGPS	2003-2017
Palano et al. [2018]	Dead Sea Fault		Arabia	32	CGPS	15 yr, 1999-2014
Gomez et al. [2020]	Dead Sea Fault		Sinai	181	CGPS, SGPS	2000-2012

Table A.1: Compiled 45 geodetic datasets of the Mediterranean, primarily made up of continuous and episodic survey Global Navigation Satellite System (CGNSS, SGNSS) and Global Positioning System (CGPS, SGPS) observations derived from time series that are at least 2 years long, which altogether record the long-term slow surface deformation field over a rough period of 1992 to 2019. Other collected data types include semi-continuous GPS (sCGPS) [Danesi et al., 2015; Serpelloni et al., 2016] and Interferometric Synthetic Aperture Radar (InSAR) data [Aslan et al., 2019]. Certain vectors from the 45 papers have been left out of our compilation if they are positioned outside the Mediterranean model domain (Figure 5), or if they are clearly inconsistent with regional motion trends (Figure A.6). The 45 datasets have been processed into different plate velocity and global geodetic frames, like the Eurasia-fixed frame, International Terrestrial Reference Frame (ITRF), International GNSS Service (IGS) realization (IGb) of the ITRF, and the No-Net-Rotation (NNR) frame. To correct for these rotational differences between the 44 post-Kreemer et al. [2014] networks (Section 4.3.1), we identify 10 regional datasets (in **bright yellow**; Figure A.7), each extending over a particularly large area with about 150 to hundreds of observations. Note that the 44 networks are divided into categories of datasets sharing a study area, being Iberia and Morocco (Echeverria et al. [2015], ..., Civiero et al. [2020]), Algeria (Bougrine et al. [2019]), Tunisia (Bahrouni et al. [2020]), Italy (Barreca et al. [2014a], ..., Silverii et al. [2019]), the Alps and Pyrenees (Danesi et al. [2015], ..., Walpersdorf et al. [2018]), Greece and Turkey (Ergintav et al. [2014], ..., D'Agostino et al. [2020]), and the Dead Sea Fault and Egypt (Masson et al. [2015], ..., Gomez et al. [2020]). Furthermore, note that the Bahrouni et al. [2020] network has the same vector colour (white) as the Kreemer dataset, meaning that this network had been integrated into the reference dataset at the start of the network rotation experiment (Section 4.3.1).

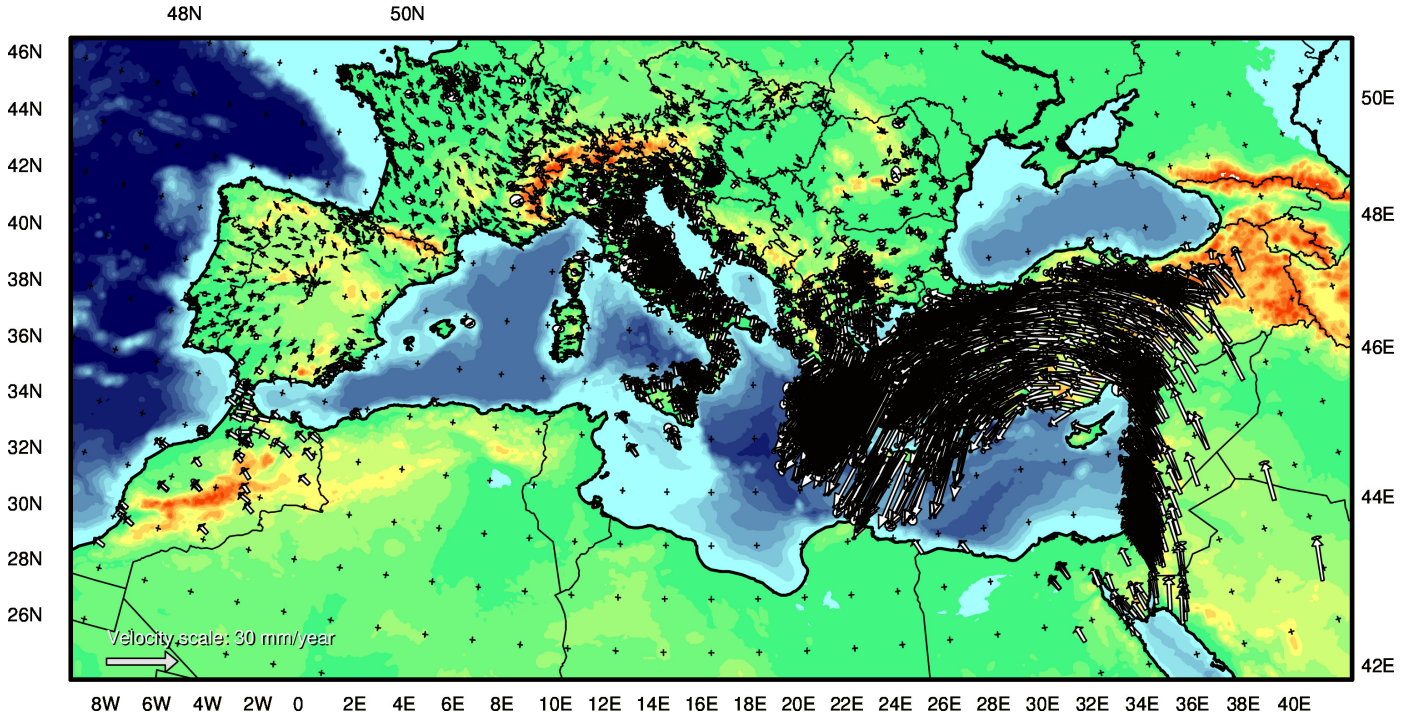


Figure A.2: 3981 GPS vectors relative to the Eurasian plate compiled from Kreemer et al. [2014], together with their 95% confidence error ellipses. We adopt this Mediterranean Kreemer network as the reference dataset for the network rotation experiment (Section 4.3.1) because it is without doubt our largest and most widespread dataset, and since all velocities have been uniformly processed into the same reference frame.

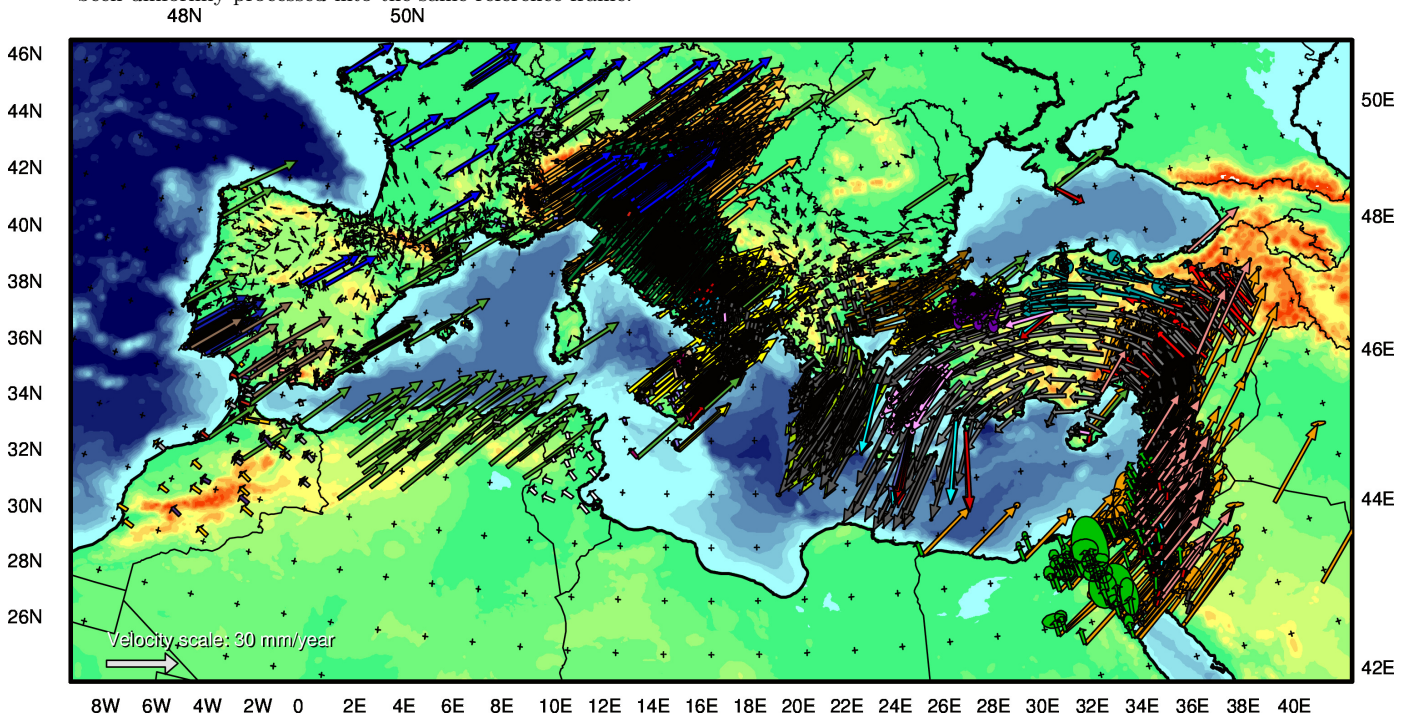


Figure A.3: 4988 GPS vectors, together with their 95% confidence error ellipses, collected from 44 post-Kreemer et al. [2014] papers. Each of the 44 geodetic networks is presented in its published reference frame, e.g. the Algerian Bougrine et al. [2019] (in green) and Balkan D'Agostino et al. [2020] (dark grey) datasets are coupled to the ITRF2014- and Eurasian frames, respectively. The 4988 motions consist of both newly issued measurement sites in regions poorly sampled by the Kreemer network, e.g. Algeria [Bougrine et al., 2019], the central Balkans (Bulgaria, Serbia, Montenegro) [Metois et al., 2015; D'Agostino et al., 2020] (purple, dark grey) the southern Black Sea region [Ergintav et al., 2014; Aktuğ et al., 2015; Özdemir and Karshoğlu, 2019] (yellow, blue, grey), Egypt [Saleh and Becker, 2015; Pietrantonio et al., 2016; Gomez et al., 2020] (green, orange, dark grey), and Tunisia [Bahrouni et al., 2020] (white), and many reprocessed observations at station positions overlapping with the Kreemer dataset.

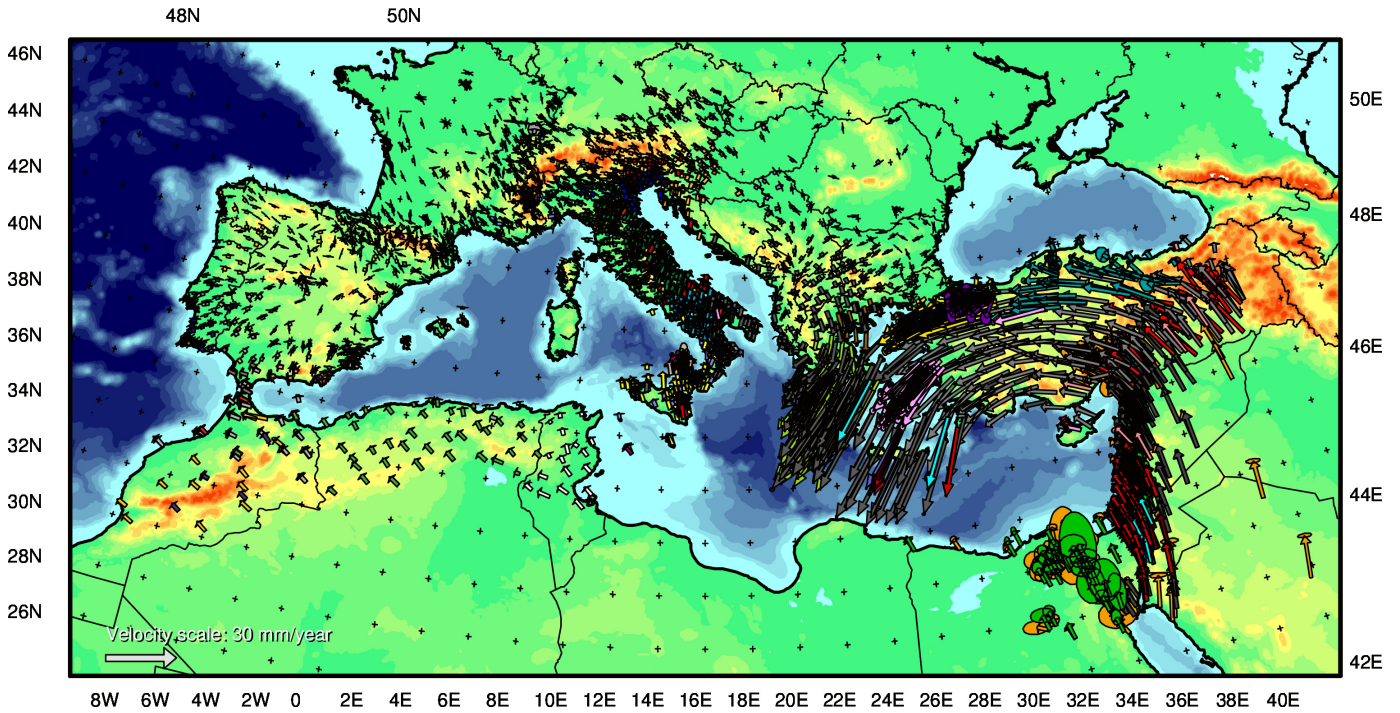


Figure A.4: 4988 GPS vectors, together with their 95% confidence error ellipses, of the 44 non-reference networks rotated into the Kreemer Eurasia reference frame (see Section 4.3.1 for details), but left in their original 43 network colours. Note that the Tunisian Bahrouni et al. [2020] dataset (in white like the Kreemer network) had been attached to the Kreemer dataset before the network rotations, and that the 25 data outliers from Figure A.6 have already been removed here. In addition, note that we choose to incorporate the Egyptian Saleh and Becker [2015] (green) and Pietrantonio et al. [2016] (orange) datasets into our compilation in spite of their large error ellipses because Egypt is poorly covered by the Kreemer network alone (Figure A.2).

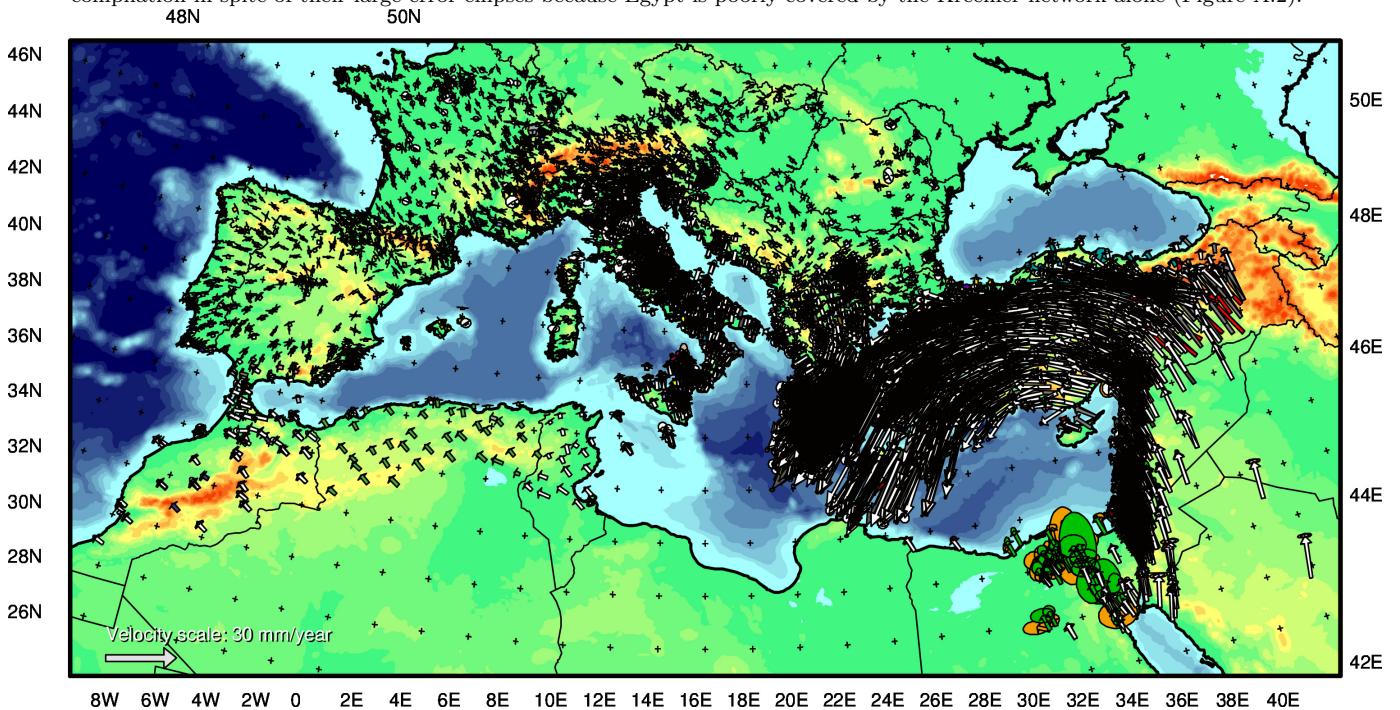


Figure A.5: 8969 GPS vectors of the Mediterranean, together with their 95% confidence error ellipses, corrected for network rotations relative to the Kreemer Eurasia dataset (in white; see Section 4.3.1 for details), but left in their original 43 network colours. Note that the Tunisian Bahrouni et al. [2020] dataset (also in white) had been merged with the Kreemer network prior to the network rotation correction, and that the 25 data outliers from Figure A.6 have already been deleted here. Moreover, note that we decide to include the Egyptian Saleh and Becker [2015] (green) and Pietrantonio et al. [2016] (orange) datasets into our compilation despite their large error ellipses since Egypt is poorly sampled by the Kreemer network alone (Figure A.2).

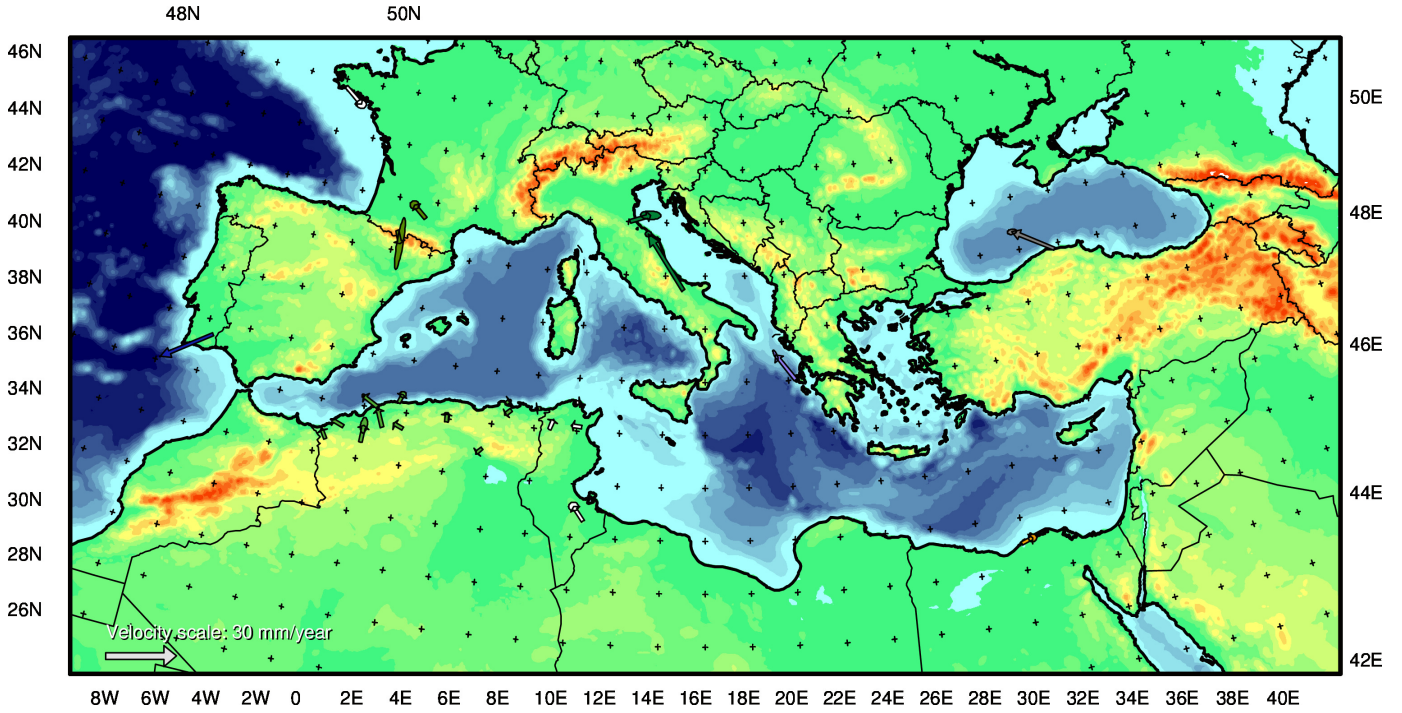


Figure A.6: 25 GPS vectors relative to the Eurasian plate that clearly do not express regionally consistent motion, together with their 95% confidence error ellipses. These 25 data outliers have been excluded from the compilation (Figure 2). Especially, 16 of them from the Algerian Bougrine et al. [2019] (in green) and Tunisian Bahrouni et al. [2020] (white) datasets have been discarded in view of the likelihood that the outlying velocities would dominate the inverse problem in Algeria and Tunisia where data are relatively sparse. The remaining outliers identified by us come from Kreemer et al. [2014] (white), Mantovani et al. [2015] (dark green), Metois et al. [2015] (purple), Nguyen et al. [2016] (green), Pietrantonio et al. [2016] (orange), Cabral et al. [2017] (blue), and Özdemir and Karshoğlu [2019] (grey).

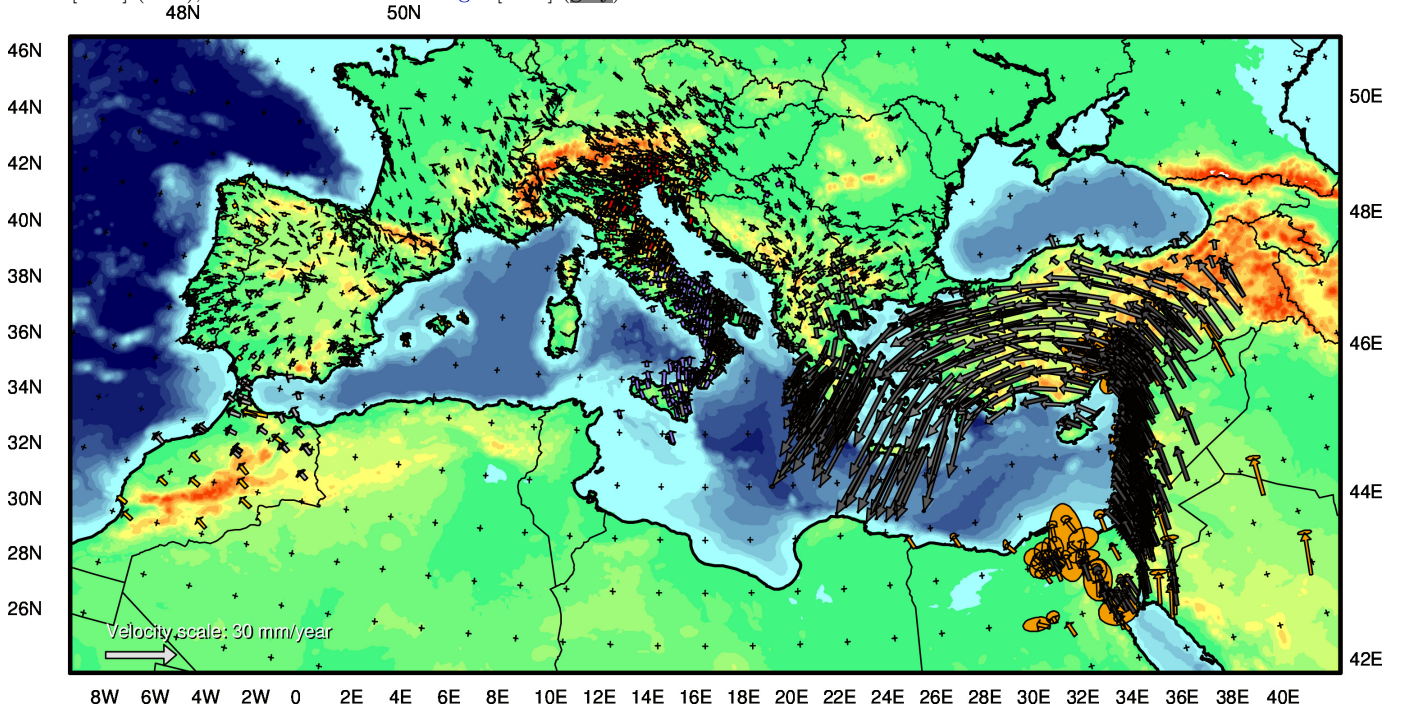


Figure A.7: 3017 GPS vectors relative to the Eurasian plate, together with their 95% confidence error ellipses, belonging to ten networks that contain around 150 to hundreds of widely distributed observations, which typically have numerous site locations in common with the Kreemer dataset and local networks. The ten datasets correspond to Metois et al. [2015] (in purple; 662 vectors), Palano et al. [2015] (light orange; 320), Nguyen et al. [2016] (green; 179), Pietrantonio et al. [2016] (dark orange; 385), Serpelloni et al. [2016] (orange; 456), Sánchez et al. [2018] (red; 180), Özdemir and Karshoğlu [2019] (grey; 184), Civiero et al. [2020] (light grey; 141), D'Agostino et al. [2020] (dark grey; 329), and Gomez et al. [2020] (dark grey; 181). Establishing such regional networks may help resolving the network rotations of smaller datasets, see Section 4.3.1 for experiments.

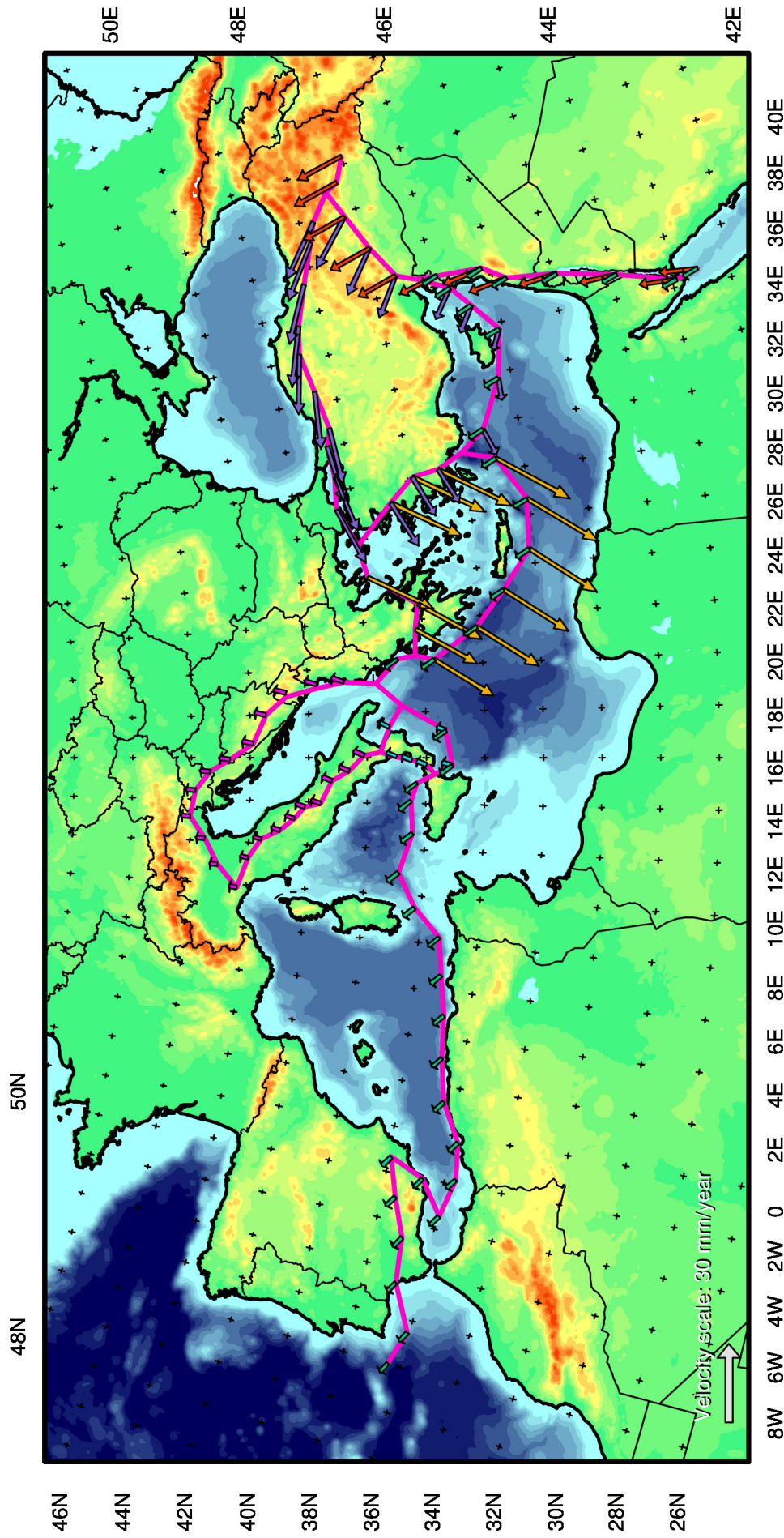


Figure A.8: 114 synthetic Euler vectors relative to the Eurasian plate, which reflect the homogeneous rigid plate motion of Africa (with **green** vectors), Adria (**pink**), the Aegean Region (**yellow**), Anatolia (**purple**), Arabia (**red**), and Calabria (**blue**) at plate boundary faults (in **pink**). The Euler velocities have been calculated at the positions of 90 fault nodes, disregarding triple junctions, using the relative Euler poles inferred from the IGS08-frame poles published by [Kreemer et al. \[2014\]](#) for Africa and Arabia (see Section 4.2 for details), and the Euler poles estimated from all geodetic observations located inside crustal blocks for Adria, the Aegean Region, Anatolia, and Calabria (Section 4.3.2). Note that the computed relative plate motions are (very) similar in faulting style to the fault creep solutions determined by inverting the averaged GPS and substituted Euler plate velocity datasets (Figure 16), e.g. see the sinistral Arabia-Anatolia fault motion at the East Anatolian Fault. One experiment that we leave for future research is to quantitatively compare Euler plate boundary vectors to resolved fault slip rates in terms of misfit, see Section 5.3 for elaboration.